

JPRS-CST-85-036

23 October 1985

China Report

SCIENCE AND TECHNOLOGY



FOREIGN BROADCAST INFORMATION SERVICE

NOTE

JPRS publications contain information primarily from foreign newspapers, periodicals and books, but also from news agency transmissions and broadcasts. Materials from foreign-language sources are translated; those from English-language sources are transcribed or reprinted, with the original phrasing and other characteristics retained.

Headlines, editorial reports, and material enclosed in brackets [] are supplied by JPRS. Processing indicators such as [Text] or [Excerpt] in the first line of each item, or following the last line of a brief, indicate how the original information was processed. Where no processing indicator is given, the information was summarized or extracted.

Unfamiliar names rendered phonetically or transliterated are enclosed in parentheses. Words or names preceded by a question mark and enclosed in parentheses were not clear in the original but have been supplied as appropriate in context. Other unattributed parenthetical notes within the body of an item originate with the source. Times within items are as given by source.

The contents of this publication in no way represent the policies, views or attitudes of the U.S. Government.

PROCUREMENT OF PUBLICATIONS

JPRS publications may be ordered from the National Technical Information Service, Springfield, Virginia 22161. In ordering, it is recommended that the JPRS number, title, date and author, if applicable, of publication be cited.

Current JPRS publications are announced in Government Reports Announcements issued semi-monthly by the National Technical Information Service, and are listed in the Monthly Catalog of U.S. Government Publications issued by the Superintendent of Documents, U.S. Government Printing Office, Washington, D.C. 20402.

Correspondence pertaining to matters other than procurement may be addressed to Joint Publications Research Service, 1000 North Glebe Road, Arlington, Virginia 22201.

23 October 1985

CHINA REPORT

SCIENCE AND TECHNOLOGY

CONTENTS

PEOPLE'S REPUBLIC OF CHINA

NATIONAL DEVELOPMENTS

- Special Features of the Limitations to China's Patent Law
(Zheng Chengsi; GUOJI MAOYI WENTI, No 3, May-Jun 85) 1

PHYSICAL SCIENCES

- Foetus Model, Demographic Stability Described
(Shi Jiahong; SHUXUE DE SHIJIAN YU RENSHI, No 4, Oct 85) 5
- Application of Fuzzy Mathematics in Core Drilling Discussed
(Wang Shaohao, Gao Shen; SHUXUE DE SHIJIAN YU RENSHI,
No 1, Jan 85) 11

APPLIED SCIENCES

- Structure of Nylon 1010 Described
(Yang Xiaozhen, et al.; GAOFENZI TONGXUN, No 3, Jun 85) 19
- Differential Elastic Scattering Cross Sections of 14.2 MeV
Neutrons From Niobium
(Li Jingde, et al.; YUANZHE WULI, No 2, May 85) 27
- Differential Circuit Model for Turbomolecular Pump Blade
(Chu Jiguo, Sun Yunlong; ZHENKONG KEXUE YU JISHU, No 5,
Sep 84) 35
- Theoretical Calculation of Pulsed Active-Passive Mode-Locked
Solid State Lasers (Part I)
(Zhu Zhenghe; WULI XUEBAO, No 5, May 85) 49
- Theoretical Calculation of Pulsed Active-Passive Mode-Locked
Solid State Lasers (Part II)
(WULI XUEBAO, No 5, May 85) 59

Optical Adjustment for EOT2000 Infrared Rangefinder Detailed (CENGJI TUBUBAO, No 3, 25 Jun 85)	72
Configuration and Longitudinal Wind Tunnel Testing of Forward-Swept Wings (Ye Weiliang, Riao Renxi; KONGQIDONGLIXUE XUEBAO, No 2, Jun 85)	80
SCIENTISTS AND SCIENTIFIC ORGANIZATIONS	
China's First Symposium on Tectonophysics Held (DIZHI LIEFENG, No 4, Jul 85)	91
ABSTRACTS	
BIOCHEMISTRY	
FUDAN XUEBAO (ZIRAN KEXUE BAN) [JOURNAL OF FUDAN UNIVERSITY (NATURAL SCIENCE)], No 2, Jun 85	93
CHEMISTRY	
GAOFENZI TONGXUN [POLYMER COMMUNICATIONS], No 1, Feb 85	95
FENXI HUAXUE [ANALYTICAL CHEMISTRY], No 5, 20 May 85	100
ENGINEERING	
NANJING DAXUE XUEBAO (ZIRAN KEXUE) [JOURNAL OF NANJING UNIVERSITY (NATURAL SCIENCES EDITION)], No 4, Dec 84	107
TIANJIN DAXUE XUEBAO [JOURNAL OF TIANJIN UNIVERSITY], No 1, Jan 85	110
INORGANIC CHEMISTRY	
FUDAN XUEBAO (ZIRAN KEXUE BAN) [JOURNAL OF FUDAN UNIVERSITY (NATURAL SCIENCE)], No 2, Jun 85	112
ORGANIC CHEMISTRY	
FUDAN XUEBAO (ZIRAN KEXUE BAN) [JOURNAL OF FUDAN UNIVERSITY (NATURAL SCIENCE)], No 2, Jun 85	113
SILICATES	
GUISUANYAN XUEBAO [JOURNAL OF THE CHINESE SILICATE SOCIETY], No 2, Jun 85	114

NATIONAL DEVELOPMENTS

SPECIAL FEATURES OF THE LIMITATIONS TO CHINA'S PATENT LAW

Beijing GUOJI MAOYI WENTI [INTERNATIONAL TRADE JOURNAL] in Chinese No 3,
May-Jun 85 pp 1-7

[Article by Zheng Chengsi [5774 :2052 1835], Law Institute, the Chinese Academy of Social Sciences: "The Limitations of Patents With Regard to International Trade"]

[Excerpt] II. Some Special Features of the Limitations to Chinese Patents

A. The "State Plan Permit" System

In order to assist in the popularization of advanced technologies in China and at the same time not to hinder the importation of foreign advanced technologies, China's patent law has adopted a unique "state plan permit" system. This system works as follows: Relevant departments in charge under the State Council and the people's governments of provinces, autonomous regions and centrally-administered municipalities are authorized to allow, according to the state plan, designated units to use the patent for an important invention or creation held by units under state ownership that are within their own system or under their jurisdiction; the designated unit that uses the patent shall pay royalties to the unit which holds the patent, in accordance with state stipulations. If a Chinese unit under the collective ownership system or an individual owns a patent which is of major significance to the national or public interests, and which should be popularized, the relevant departments in charge under the State Council may submit a report to the State Council and on approval by the State Council, this type of patent may also be dealt with according to the above-stated provisions.

To implement the "state plan permit" system and other special restrictions of the Chinese system, the Chinese patent law divides patentees into three categories: 1. Patent-holders, i.e. patentees who are Chinese enterprises and units under state ownership; 2. Chinese patent-owners, i.e. patentees who are Chinese enterprises and units under the collective ownership system and Chinese natural persons; 3. Foreign owners of patents, i.e. Chinese-foreign joint venture enterprises, wholly-owned foreign enterprises and foreign natural persons who have obtained Chinese patents.

The "state plan permit" system applies only to patentees under the first two categories. Foreign owners of advanced technologies need not worry about having their patents, brought in as shares in joint ventures, as investments, etc., "popularized" and their exclusive use rights invalidated.

In relation to the State Council and its relevant departments in charge and the relevant departments of provinces, autonomous regions and centrally-administered municipalities, Chinese holders and owners of patents are by law restricted in their exclusive use rights. These particular restrictions are different from most of the restrictions discussed in Chapter 1. Under most of the conditions discussed in Chapter 1, the exclusive use right of the patentee loses all binding effect on everyone, but under the "state plan permit" system, the exclusive use right of the patentee loses validity only with respect to the state organs concerned and the users specially designated by these organs. This means that the holder or owner of a patent that is to be "popularized" still retains his exclusive rights in relation to all enterprises and individuals other than those specially designated by the state for use of the patent. It means that the enterprise or person has the right of granting licenses and collecting use fees, as well as the right to file suits against unlicensed users and to claim compensation.

B. Restrictions in the Assignment of Patents

The right of assignment is not a right peculiar to owners of patents, but one enjoyed (under general conditions) by every owner of a property. In most countries, a patentee is not at all restricted in the assignment of his patent right, just as the owner of goods when selling his goods. However, because the "patent-holders" among the Chinese patentees also have ownership rights in units under the system of state ownership, they are not legally designated "owners" of the patent, but merely "holders." When assigning patent rights, this type of unit must, therefore, obtain approval from its higher competent authority. In international trade, foreign enterprises that claim to have obtained Chinese patents must pay special attention to this matter. They must first of all clarify whether the patent which is being assigned to them is held by a unit under state ownership, and if so, whether the transfer was approved by its superior organ. Otherwise, they would possibly be obtaining a patent through an illegal transfer. At the same time, any assignment of a patent to a foreigner must be approved by the responsible State Council department. This provision applies to the patent rights of all Chinese juristic persons and individuals.

The assignments dealt with here refer to the transfer of patent rights as property and not to the transfer of use rights (i.e., not to the granting of patent licenses). The Chinese patent law imposes no restrictions at all on the right of Chinese holders or owners of patents to issue licenses.

C. No "Import Rights" Being Conferred

China's patent law does not confer "import rights" to the patentee; this is a further provision that limits the patent. The question whether an import right is conferred is usually brought up in the patent legislation of developing countries. The granting of an import right has its positive

aspects with regard to the importation of advanced technologies. Because the owner of the advanced technology will in general apply for a patent in developed countries as well as in developing countries, an enterprise that has obtained a patent license in a developed country has frequently a much larger production capacity at its disposal than an equivalent enterprise in a developing country. If the patentee in the latter kind of country cannot enjoy the controlling right over the importation of the patented product, the assignee in the first type of country, through marketing the products in the latter type, can make it unprofitable to manufacture in the latter type of country. In consideration of this consequence, the owner of the technology will abstain from applying for a patent in the latter type of country, but if import rights would be conferred, it would induce the foreign patentee to obstruct the importation of the same article, manufactured in high quality and at low price, into the developing country and thereby cause economic losses to these countries.

However, we must come to understand: countries which confer import rights to the patentee will also frequently not allow this import right to be exercised at will by the patentee. First, the import right is not being granted for designs; second, as to the import right for invention patents, it is frequently restricted by other even more stringent measures. For instance, Article 1, Paragraph 2 of the Unified Patent Law of the African Intellectual Property Organization mentions the conferring of import rights to the patentees, but also stipulates in its Article 55, Paragraph 1: For the importation of certain patented products for the important need of national defense, public health and national economy, the industrial property department of any member nation of the African Intellectual Property Organization is authorized to issue "requisitioning licenses," to assist importation. The requisitioning by the state is one method that inflicts on the owner of the technology a more serious restriction than not having the import right. China did not institute a state requisitioning system, rights are therefore balanced, and it is only that no import right is conferred, which will not at all hinder Chinese importation of technologies.

In developed countries where the patent law confers import rights to patentees, restrictive provisions are frequently added to prevent the patentee using this monopolistic right from creating a negative influence on the market of one's own country. For instance, Article 48 of the British patent act of 1977 (revised in 1979) stipulates: If a certain patented invention is capable of being used in the United Kingdom but has its use hindered by importation of the said patented product, anyone expecting to use that invention may apply for a compulsory license; in another respect, if the demand on the British market for a certain patented product is being met to a substantial extent by importation, the Patent Office can change this situation by issuing compulsory patent licenses, so that one's own country may be able to manufacture the same type of products.

This shows that not granting import rights to patentees, although a limitation of a special kind in China, is not at all excessive compared with other countries; it is a reasonable limitation.

D. "No Punishment for Ignorance"

Article 62, Paragraph 2, of the Chinese Patent Law stipulates: "The use or sale of a patented product without any knowledge that such product was manufactured and sold without the permission of the patentee" shall not be deemed to infringe a patent. Because use was unknowing use, it can generally be called "use in good faith". Using the product well knowing that the article is patented by someone else can be called "use in bad faith." In the patent laws of most countries such "use in bad faith" is considered an act of patent infringement, but they do not explicitly say whether "use in good faith" constitutes a patent infringement, or make "use in good faith" into a limitation of the patent law. This article of China's patent law, therefore, appears to be unique.

The said provision in the Chinese law can be similarly expressed by a traditional saying in the ancient Chinese legal system, namely "no punishment in case of ignorance." The main reason for this provision is, in my opinion, that under the present conditions in China, when protection of patents is only in its initial stage, and the majority of Chinese, at this stage, have no direct understanding of the actual significance of the monopoly of the patentee, it is hard to prevent patented products from being unknowingly used or sold by careless oversight. It is, therefore, reasonable not to treat such actions as patent infringements at the present time. However, I believe that the specific application of this provision will at least require some supplementation: First, on gaining the knowledge which he lacked before (regardless of whether he was warned by the patentee or informed by others), the offender must immediately halt the activity in question. Second, if the offending party has gained an unjustifiable profit from the patented products during the time he unknowingly used or sold them, he must, on gaining knowledge of the state of things, turn the profits over to the state treasury or use them to compensate the patentee for losses (if there had been losses). Third, the offending party must submit positive evidence of his "ignorance."

At the same time, attention should also be paid to the following: many foreign countries merely recognize responsibility for "acts committed with full knowledge," but do not explicitly negate responsibility for "acts committed in ignorance." If the commercial transactions that possibly relate to patents took place outside of China, the special provisions of Article 62, Paragraph 2, of the Chinese patent law must not, therefore, be indiscriminately applied, but every possible effort should be made beforehand to avoid such unknowing use or sale, as otherwise the offender will possibly be sued (and, furthermore, adjudged) as having committed an infringement of patent rights.

9808

CSO: 4006/954

PHYSICAL SCIENCES

FOETUS MODEL, DEMOGRAPHIC STABILITY DESCRIBED

Beijing SHUXUE DE SHIJIAN YU RENSHI [MATHEMATICS IN PRACTICE AND THEORY]
in Chinese No 4, Oct 84 pp 31-35

[Article by Shi Jiahong [2508 0857 7703] of Fu Dan University: "Foetus Model and Its Stability in Demography"]

[Text] 1. Introduction

The huge-numbered population problem is often induced by solving the initial boundary value problem of a partial differential equation of the first order [1, 2]. Without considering population migration, the partial differential equation is

$$u_t + u_x = -\mu(x, t)u, \quad (1)$$

In the equation, the unknown function $u(x, t)$ represents the age density of the population at time "t" and age "x", and $\mu(x, t)$ represents the ratio of the death rate of the population. Variables "x" and "t" represent, respectively, age and time with units of age and year, respectively. The age density of population at the initial time is known, that is,

$$u(x, 0) = \varphi(x), \quad (2)$$

Marginal conditions are in a feedback form [3]:

$$u(0, t) = \beta(t) \int_{r_1}^{r_2} h(x, t) k(x, t) u(x, t) dx, \quad (3)$$

In it, r_1, r_2 are the upper and lower limits of the female child-bearing age, $h(x, t)$ is the birth model, $k(x, t)$ is the ratio of the female population and $\beta(t)$ is the female birth rate at time "t".

Here in birth rate there is no distinction between the number of times of birth and the number of foetuses, and for a more precise and reasonable calculation, it is appropriate to consider separately the birth rate of each birth because the birth model of each birth is obviously different.

The birth model curve of $i+t$ is almost the birth curve of i moving horizontally several years to the right. On the other hand, from the practical point of view, the fetus model is also convenient. The reason is that in the formulation of a population policy, the relationship between the birth rate and the birth model can be better considered.

Suppose that the birth model of "i" birth is $h_i(x, t)$ and the birth rate is $\beta_i(t)$. Then the fetus model is to change Equation (3) to

$$u(0, t) = \sum_{i=1}^N \beta_i(t) \int_0^{\infty} h_i(x, t) \phi(x, t) u(x, t) dx, \quad 0 \leq \beta_i \leq 1. \quad (4)$$

What value positive integer "N" takes depends on the problem. Based on the situation of our nation, "N" may take the value of 3. However, whatever value "N" may take will not have any substantial effect on our following conclusion. Therefore, we still use the general "N" to express the marginal condition.

Articles [2], [3] and [5] on the stability problem of systems (1), (2) and (3) under the Lyapunov stability function have been discussed in detail, and it has been proved that there exists a marginal birth rate β_0 , in which when constant $\beta \leq \beta_0$, the solution of (1), (2) and (3) is stable, and when $\beta > \beta_0$, it is not.

Now let us discuss the solution of (1), (2) and (4) and the problem of stability.

II. Solution of Problem of Initial Marginal Value

Theorem 1: When $x \in (0, \infty)$, $t \geq 0$, the solution for (1), (2) and (4) is

$$u(x, t) = \begin{cases} \phi(x-t)e^{-\int_0^t \mu(x-t+\tau) d\tau}, & x-t \geq 0 \\ \sum_{i=1}^N \beta_i(t-x) \int_0^{\infty} h_i(r, t-x) \phi(r, t-x) u(r, t-x) dr e^{-\int_0^t \mu(x-t+\tau) d\tau}, & x-t < 0 \end{cases} \quad (5)$$

Proof: Let

$$v(x, t) = u(x, t)e^{\int_0^t \mu(x-t+\tau) d\tau},$$

then function $v(x, t)$ satisfies

$$v_t + v_x = 0, \quad (6)$$

$$v(x, 0) = \phi(x)e^{\int_0^0 \mu(x-t+\tau) d\tau}, \quad (7)$$

$$v(0, t) = \sum_{i=1}^N \beta_i(t) \int_0^{\infty} h_i(r, t) \phi(r, t) e^{-\int_0^t \mu(r-t+\tau) d\tau} v(r, t) dr \quad (7')$$

The general solution representation of (6) is

$$v(x, t) = f(x - t).$$

To get the form of function f , let $t=0$, and we get

$$f(x) = \varphi(x)e^{\int_0^x \lambda(\tau) d\tau}, \quad x \geq 0.$$

When $x - t \geq 0$,

$$\begin{aligned} v(x, t) &= \varphi(x - t)e^{\int_0^{x-t} \lambda(\tau) d\tau}, \\ v(x, t) &= v(x, t)e^{-\int_0^t \lambda(x-t+\tau) d\tau} = \varphi(x - t)e^{-\int_0^t \lambda(x-t+\tau) d\tau}. \end{aligned} \quad (8)$$

Substituting $x=0$ for $t(x - t)$, we get

$$f(-t) = \sum_{j=0}^n g_j(t) \int_0^t \lambda(\tau) \varphi(\tau) e^{-\int_0^{\tau} \lambda(x-t+\tau) d\tau} v(\tau, t) d\tau, \quad t \geq 0.$$

When $x - t < 0$,

$$\begin{aligned} v(x, t) &= f(x - t) = \sum_{j=0}^n g_j(t - x) \int_0^{x-t} \lambda(\tau) \varphi(\tau) e^{-\int_0^{\tau} \lambda(x-t+\tau) d\tau} v(\tau, t - x) d\tau \\ &= \sum_{j=0}^n g_j(t - x) \int_0^x \lambda(\tau) \varphi(\tau) e^{-\int_0^{\tau} \lambda(x-t+\tau) d\tau} v(\tau, t - x) d\tau, \\ v(x, t) &= \sum_{j=0}^n g_j(t - x) e^{-\int_0^x \lambda(x-t+\tau) d\tau} \\ &\quad \times \int_0^x \lambda(\tau) \varphi(\tau) e^{-\int_0^{\tau} \lambda(x-t+\tau) d\tau} v(\tau, t - x) d\tau. \end{aligned} \quad (9)$$

The combination of (8) and (9) is (5), and the theorem is proved. Notice that $\sigma_1 > 0$, so (5) is a recurrence representation of "u".

III. Stability of Solution

Here we discuss the continuity of the solution's dependence on the $t \geq 0$ initial state. To describe it precisely, that is, if $\epsilon > 0$, there is always

$\delta > 0$, then when

$$\| \varphi(x) \| \leq \delta \quad (10)$$

there will be

$$\sup_{t \in [0, \tau_0]} \|u(t, x)\| \leq \delta. \quad (11)$$

Among them $\|\cdot\|$ is a norm of $x \in [0, \tau_0]$ with a certain meaning. Then the system is considered stable. Otherwise, it is not stable, especially in a case no matter how small δ is, there is always a $\varphi(x)$ to satisfy (10) to make

$$\lim_{t \rightarrow \infty} \sup_{x \in [0, \tau_0]} \|u(t, x)\| = \infty.$$

Then the system (1)(2)(4) is divergent unstable.

Notice that $u(x, t)$ is the continuous function of $x \in [0, \tau_0]$, $t \geq 0$. Here we take the maximum value of the norm of $[0, \tau_0]$, that is,

$$\|u(x, t)\| = \max_{x \in [0, \tau_0]} u(x, t).$$

$$\text{Theorem 1: (i) If } \sum_{i=1}^n p_i(t) \int_0^{\tau_0} k_i(x, t) u(x, t) e^{-\int_0^t \lambda_i(s) ds} dx \leq 1, \quad (12)$$

then the system is stable.

(ii) Suppose there exists $\epsilon > 0$, that makes

$$\sum_{i=1}^n p_i(t) \int_0^{\tau_0} k_i(x, t) u(x, t) e^{-\int_0^t \lambda_i(s) ds} dx \geq 1 + \epsilon, \quad (13)$$

Then the system (1)(2)(4) is divergent unstable.

Proof: Suppose (12) stands, write

$$\max_{x \in [0, \tau_0]} \varphi(x) e^{\int_0^t \lambda_i(s) ds} = M.$$

Let $x \in [0, \tau_0]$. From (6) we can easily see that when $x \in [t, \tau_0]$

$$\max_{x \in [0, \tau_0]} u(x, t) = \max_{x \in [t, \tau_0]} \varphi(x - t) e^{\int_0^t \lambda_i(s) ds} \leq M. \quad (14)$$

When $x \in [0, t]$, from (5), (12) and (14) we get

$$\begin{aligned} u(x, t) &= \sum_{i=1}^n p_i(t - x) \int_0^{\tau_0} k_i(x, t - x) u(x, t - x) e^{-\int_0^{t-x} \lambda_i(s) ds} dx \\ &\leq M \sum_{i=1}^n p_i(t - x) \int_0^{\tau_0} k_i(x, t - x) u(x, t - x) e^{-\int_0^{t-x} \lambda_i(s) ds} dx \leq M. \end{aligned} \quad (15)$$

as against $x \in [0, \tau_0]$ stands

$$\sup_{x \in [0, \tau_0]} u(x, t) \leq M. \quad (16)$$

Repeat the steps in (13), and it will be easy to get (16) when $t \geq 0$. Then to the assigned $\epsilon > 0$, we only take

$$t = \epsilon e^{-\int_0^t \mu(s) ds}.$$

Then from (16) we know that (15) can be deduced from (13). Theorem (1) is proved.

Now suppose (13) stands, if we let

$$\phi(x) = a_0 e^{-\int_0^x \mu(s) ds},$$

then when $x - t \geq 0$,

$$\phi(x, t) = a_0.$$

Let us use finite induction to prove that when

$$\begin{aligned} -(\mu + 1)r_1 \leq x - t \leq -\mu r_1, \quad t \leq r_1, \\ \phi(x, t) \geq (1 + \epsilon)^{-1} a_0. \end{aligned} \quad (17)$$

In fact, when $-\mu r_1 \leq x - t \leq 0$

$$\begin{aligned} \phi(x, t) &= \sum_{i=1}^n \beta_i \int_0^t k_i(t-s) \phi(t-s) \phi(t-s) e^{-\int_0^{t-s} \mu(s) ds} ds \\ &= a_0 \sum_{i=1}^n \beta_i \int_0^t k_i(t-s) \phi(t-s) e^{-\int_0^{t-s} \mu(s) ds} ds \geq (1 + \epsilon)^{-1} a_0. \end{aligned} \quad (18)$$

If the second equality sign in (18) is changed to " \geq ", then (18) stands against $-\mu r_1 \leq x - t \leq 0$ and this is (17) when $\mu = 0$.

Repeat steps in (18) and change a_0 to $(1 + \epsilon)^{-1} a_0$, and using finite induction (17) can be proved.

From (17) the conclusion of Theorem (1) can be immediately derived. The theorem is proved.

Note 1: If (12) or (13) does not stand at any condition but only when $t \geq t_0$, and t_0 is a positive constant, then obviously the conclusion of the theorem will still stand.

Note 2: We call the situation in which the equality sign in (12) stands a birth marginal saturation. If μ, β, k , and λ have no relation with time "t", then the marginal saturation becomes

$$\sum_{i=1}^n \beta_i \int_0^{\infty} k_i(s) \phi(s) e^{-\int_0^s \mu(s) ds} ds = 1. \quad (19)$$

We call the birth rate $\lambda_1, \lambda_2, \dots, \lambda_N$ that satisfies the relational formula (19) a marginal birth rate. In this situation, the (ii) of Theorem 2 can be changed to (ii)' on condition

$$\sum_{i=1}^N \lambda_i \int_0^{\infty} k_i(s) k(s) e^{-\lambda_i s} ds > 1.$$

Then the system is divergent stable. Therefore, in this situation, when the birth rate is greater than the marginal value, it becomes unstable, and when the birth rate is less or equal to the marginal value, it becomes stable.

Note 3: If we let

$$k_i(s, t) = k(s), \quad i = 1, 2, \dots, N, \quad \sum_{i=1}^N \lambda_i = \lambda, \quad (20)$$

then (19) changes to

$$\lambda = \frac{1}{\int_0^{\infty} k(s) k(s) e^{-\lambda s} ds}.$$

This is just the representation of the marginal birth rate mentioned in Articles [3] and [5]. The first formula in (20) represents the birth model without foetus differentiation, and the λ in Formula 2 is the birth rate defined in Article [3]. Therefore, Theorem 2 is the extension of the stability concluded in Articles [3] and [5].

REFERENCES

- [1] and [2] Song Jian [1345 0256], Tian Xueyuan [3944 3785 0955], Yu Jingyuan [0060 2529 0337] and Li Guangyuan [2621 1684 0337], "Population Forecast and Control," People's Press, 1982.
- [3] Song Jian and Yu Jingyuan, "Theory of Population System Stability and Marginal Female Birth Rate," AUTOMATION JOURNAL, Vol 7 (1981).
- [4] Li Youyun [2621 2589 3387], Chen Bingzhen [7115 0014 3791] and Zhang Nengli [1728 5174 0500], "A Mathematical Simulation of the Population Migration Process in Our Country," POPULATION STUDY, Vol 3 (1980).
- [5] Song Jian, Yu Jingyuan and Li Guangyuan, "Theory on Prospects of Population Evolution Processes," SCIENTIA SINICA, Vol XXIV (1981) p 2.

12909

C50: 4008/1034

PHYSICAL SCIENCES

APPLICATION OF FUZZY MATHEMATICS IN CORE DRILLING DISCUSSED

Beijing SHUXUE DE SHIJIAN YU RENSHI in Chinese No 1, Jan 85 pp 14-18

[Article by Wang Jiaohao [3169 1421 6275] and Gao Shen [7559 2773], Zhongnan Institute of Metallurgy]

[Text] Most of the studies in petrographic grading by the geological exploration departments in China and foreign countries are limited to studies of the drillability of rocks which offer various programs in rock grading according to drillability. This kind of grading gives consideration only to the degree of difficulty of the mechanical disaggregation of the rocks without considering the effects of the stratigraphic complexity, wall stability, hole deviation and difficulty of core sampling on the drilling technology process as a whole. Therefore, this kind of grading can reflect the drillability of the rocks but cannot reflect the difficulty of the core drilling of a certain area as a whole.

In estimating investment needed to prospect in a certain area, the management department must make a comprehensive evaluation of the difficulties of drilling. We believe that besides drillability, one must also consider factors of stability, difficulty of core sampling and hole deviation. Only with the four factors considered can one have an overall view of the difficulties of the drilling operation.

Lacking a more scientific method in our country for the calculation of investment needed to prospect a certain area, we present for discussion in this article a comprehensive evaluation method using fuzzy mathematics, with consideration of the four factors of drillability, stability, difficulty of core sampling and hole deviation in a certain site to provide a comprehensive evaluation and a classification of the difficulty of an exploration drilling. We also offer a simple model of calculation for the evaluation of exploration drilling investment in a certain area.

Let the aggregate of the target factors be

$$U = (\text{drillability, stability, difficulty of core sampling, hole inclination})$$

The result of the evaluation will be the drillability of the exploration drilling, which is divided into five grades which also mean the five levels of investment:

$$V = \{I, II, III, IV, V\}.$$

The criteria for single-factor evaluation are shown in Table 1. For better understanding and simpler calculation, in our evaluation considering the main factor of drillability, we use only the index of mechanical drilling speed. For the same reason, in stability, we use the index of the longitudinal wave velocity V_p measured from the core sample; in drillability of rock sampling, we use the percentage of the core sampling rate; and in bore inclination, we use the result of boring electrical logging, the index of axial deviation calculated from the bearing and the spiral angle.

Table 1. Classification of Drillability in Exploration

(1) 等级		I	II	III	IV	V
(3) 岩性	(11) 机械钻速	(11) 0	(11) 1-1.5	(11) 1.5-2	(11) 2-2.5	(11) 2.5-3
	(12) 稳定性	(12) 1-1	(12) 1-1	(12) 1-1	(12) 1-1	(12) 1-1
	(13) 钻探率	(13) >1	(13) 1.0-1.25	(13) 1.25-1.5	(13) 1.5-1.75	(13) 1.75-2
(17) 岩心	(14) 机械钻速	(14) 1-1.5	(14) 1.5-2	(14) 2-2.5	(14) 2.5-3	(14) 3-3.5
	(15) 钻探率	(15) >1	(15) 1-1	(15) 1-1	(15) 1-1	(15) 1-1
(20) 岩心	(16) 机械钻速	(16) 1-1.5	(16) 1.5-2	(16) 2-2.5	(16) 2.5-3	(16) 3-3.5
	(17) 钻探率	(17) >1	(17) 1-1	(17) 1-1	(17) 1-1	(17) 1-1
(28) 岩心	(18) 机械钻速	(18) 1-1.5	(18) 1.5-2	(18) 2-2.5	(18) 2.5-3	(18) 3-3.5
	(19) 钻探率	(19) >1	(19) 1-1	(19) 1-1	(19) 1-1	(19) 1-1

Key:

1. Class
2. Factor
3. Drillability
4. Description of extent
5. Soft
6. Mid-hard (1)
7. Mid-hard (2)
8. Hard
9. Very hard
10. Twelve rock grades

11. Mechanical drilling speed
12. Stability
13. Extent
14. Long-term stable
15. Stable
16. Medium stable
17. Unstable
18. Seriously unstable (serious tailing)
19. Longitudinal wave velocity of rock sample V_p km/sec
20. Drill sampling

Table 1 continued:

21. Extent	29. Extent
22. Very easy	30. Very unlikely deviation
23. Easy	31. Unlikely
24. Medium	32. Medium
25. Hard	33. Likely deviation
26. Very hard	34. Very likely to deviate
27. Core sampling rate	35. Axial inclination (degrees per 100 meters)
28. Hole deviation	

In any specific drilling area, though information can be obtained from the production record of one or several holes drilled and the results of rock specimen tests, rock formations are different in nature in the exploration area, and there is no way to classify the whole exploration area according to the classifications in Table 1, no matter which single factor we choose to use. For example, if drillability is used, in that area some rocks belong to incompetent beds, some to mid-competent beds and some to competent beds. Therefore, drillability in a certain area can only be a fuzzy idea and should be expressed with a fuzzy aggregate:

$$\Delta = \alpha_1/I + \alpha_2/II + \alpha_3/III + \alpha_4/IV + \alpha_5/V,$$

$$0 \leq \alpha_i \leq 1.$$

Here the U_{ij} is the extent of subordination of that element in the area of Class i to the subaggregate of "area drillability." The value of U_{ij} is derived as follows: among n times the calculations done (or of rock samples tested or the segments of holes measured or other tested values), there are n_i times whose mechanical drilling speed (or some other tested value) belongs to Class i drilling area. The total length of the former is L_i and the total length of the latter is L_n . The rate of subordination should be their ratio:

$$\alpha_i = L_i/L_n.$$

Obviously, $\sum_{i=1}^5 \alpha_i = 1$, and the fuzzy vector is inductive. Thus we get the four subaggregates of the single-factor evaluation:

$$\begin{aligned} A &= (\alpha_{11}, \alpha_{12}, \alpha_{13}, \alpha_{14}, \alpha_{15}), \\ B &= (\alpha_{21}, \alpha_{22}, \alpha_{23}, \alpha_{24}, \alpha_{25}), \\ C &= (\alpha_{31}, \alpha_{32}, \alpha_{33}, \alpha_{34}, \alpha_{35}), \\ D &= (\alpha_{41}, \alpha_{42}, \alpha_{43}, \alpha_{44}, \alpha_{45}). \end{aligned}$$

and from here we get the fuzzy relational matrix. From I to V

$$R = \begin{pmatrix} r_{11} & r_{12} & \dots & r_{1n} \\ r_{21} & r_{22} & \dots & r_{2n} \\ r_{31} & r_{32} & \dots & r_{3n} \\ \vdots & \vdots & \ddots & \vdots \\ r_{m1} & r_{m2} & \dots & r_{mn} \end{pmatrix} = \begin{pmatrix} r_{11} & r_{12} & \dots & r_{1n} \\ r_{21} & r_{22} & \dots & r_{2n} \\ \dots & \dots & \dots & \dots \\ r_{m1} & r_{m2} & \dots & r_{mn} \end{pmatrix}$$

This is the matrix derived from the single factor evaluation. The element r_{ij} represents the feasibility in the class j prospecting area with the factor i in consideration.

Again, based on statistics, if the percentage of the cost of drilling, well protection, leak repair, core collection, inclination prevention and correction, etc. in the total investment can be determined by the operational conditions and technological requirements, then we get the order of subordination

$$M = (m_1, m_2, m_3, m_4).$$

Finally, through combined calculation of the two fuzzy matrices, we get the result of the comprehensive evaluation:

$$I = M \cdot R.$$

Now, we use the statistics of the exploration drilling in a certain area and the data gathered on the spot as our bases and apply the above method to make an investment calculation. The data from a certain drilling are listed in Table 2.

From the data in that table we can get the four fuzzy subaggregates of the single-factor evaluation.

For drillability, we calculated a total of 338.50 meters. Included in it, when drilling speed is greater than 2.45 m/hr, progress is 0 meters; at speeds of 2.45-1.15 m/hr, it is 2.15 meters; at 1.15-0.57 m/hr it is 278.32 meters; at 0.57-0.25 m/hr, it is 58.03 meters; and when the speed is less 0.15 m/hr, the length is also 0 meters. Then we get

$$\begin{aligned} a_1 &= a_5 = 0, \\ a_2 &= 2.15/338.50 = 0.01, \\ a_3 &= 278.32/338.50 = 0.82, \\ a_4 &= 58.03/338.50 = 0.17, \\ I &= (0, 0.01, 0.82, 0.17, 0). \end{aligned}$$

Similarly we can calculate according to the stability: 0 meters belongs to Class I, 210.83 meters to Class II, 125.52 meters to Class III, 2.11 meters to Class IV and 0 meters to Class V, that is,

Table 2. Data From XX Prospecting Area Well ZK 7-22

1. No	(1)	(2)	(3)	(4)	(5)	(6)	(7)	(8)	(9)
2. Hole Depth <m>	井 号	井 深	井 径	井 径	井 径	井 径	井 径	井 径	井 径
3. Segment									
Length M	1	86.65	13.45	13.45	0.95	4019	86.65	13.45	13.45
4. Name of Rock									
5. Siliceous limestone	2	123.41	16.76	16.76	1.14	4091	123.41	16.76	16.76
6. Siliceous mudstone	3	127.00	3.59	3.59	0.77	4074	127.00	3.59	3.59
7. Siderite limestone	4	149.15	22.15	22.15	0.94	3835	149.15	22.15	22.15
8. Siliceous mudstone	5	151.30	2.15	2.15	1.31	2644	151.30	2.15	2.15
9. Siliceous limestone	6	181.40	18.10	18.10	0.97	3789	181.40	18.10	18.10
10. Siltstone	7	214.71	35.31	35.31	0.47	3674	214.71	35.31	35.31
11. Medium fine- grain stone bind	8	218.78	4.07	4.07	0.84	3922	218.78	4.07	4.07
12. Siltstone	9	249.50	17.24	17.24	1.00	3384	249.50	17.24	17.24
13. Pelitic siltstone	10	278.14	28.64	28.64	1.08	4014	278.14	28.64	28.64
14. Siltstone	11	295.44	18.32	18.32	0.57	4379	295.44	18.32	18.32
15. Medium fine- grain stone bind	12	298.70	3.26	3.26	0.88	3487	298.70	3.26	3.26
16. Siltstone	13	299.80	1.10	1.10	0.82	3623	299.80	1.10	1.10
17. Sandy mudstone	14	305.80	6.00	6.00	1.00	4061	305.80	6.00	6.00
18. Siltstone	15	339.34	12.54	12.54	0.64	4060	339.34	12.54	12.54
19. Fine sandstone	16	359.50	20.16	20.16	0.90	4253	359.50	20.16	20.16
20. Siltstone	17	371.89	14.39	14.39	1.08	3580	371.89	14.39	14.39
21. Sandy mudstone	18	376.61	2.72	2.72	0.37	4322	376.61	2.72	2.72
22. Fine sandstone									
23. Mechanical Drilling speed (m/hr)									
24. Longitudinal Wave Velocity <m/sec>									
25. Stratified Drilling Rate									
26. Depth									
27. Sampling Rate									
28. Record of Inclination									
29. H									
30. Optical									
31. Bearing									

$$\begin{aligned}
a_{21} &= a_{22} = 0, \\
a_{23} &= 210.83/338.50 = 0.62, \\
a_{24} &= 125.52/338.50 = 0.37, \\
a_{25} &= 2.15/338.50 = 0.01, \\
\mathbf{g} &= (0, 0.62, 0.37, 0.01, 0).
\end{aligned}$$

For core recovery, 373.61 meters are calculated. Among them, 66.13 meters with a core recovery rate greater than 90 percent belongs to Class I, 50.28 meters with a rate of 90-75 percent belongs to Class IV, 17.74 meters with a rate of 75-60 percent belongs to Class III, 32.92 meters with a recovery rate of 60-45 percent belongs to Class IV and 206.54 meters with a core rate of less than 40 percent belongs to Class V. Thus,

$$\begin{aligned}
a_{31} &= 66.13/373.61 = 0.18, \\
a_{32} &= 50.28/373.61 = 0.13, \\
a_{33} &= 17.74/373.61 = 0.05, \\
a_{34} &= 32.92/373.61 = 0.09, \\
a_{35} &= 206.54/373.61 = 0.55, \\
\mathbf{G} &= (0.18, 0.13, 0.05, 0.09, 0.55).
\end{aligned}$$

The hole deviation, first we calculate the axial inclination according to the apical angle and the bearing used for the electrical logging, as shown in Table 3. The value of the axial inclination is calculated with the cosine formula:

$$\cos \gamma = \cos \theta_1 \cos \theta_2 + \sin \theta_1 \sin \theta_2 \cos \Delta \alpha.$$

From Table 3 and by calculation, we know that when a hole deviation of 360 meters has been measured, we get

$$\begin{aligned}
a_{41} &= 50/360 = 0.14, \\
a_{42} &= 50/360 = 0.14, \\
a_{43} &= 140/360 = 0.39, \\
a_{44} &= 0, \\
a_{45} &= 120/360 = 0.33, \\
\mathbf{D} &= (0.14, 0.14, 0.39, 0, 0.33).
\end{aligned}$$

Now we get

$$\mathbf{g} = \begin{pmatrix} 0 & 0.01 & 0.62 & 0.37 & 0 \\ 0 & 0.62 & 0.37 & 0.01 & 0 \\ 0.18 & 0.13 & 0.05 & 0.09 & 0.55 \\ 0.14 & 0.14 & 0.39 & 0 & 0.33 \end{pmatrix}$$

Table 3. Results of Hole Deviation Calculation of Well ZK7-12

(1)	(2)	(3)	(4)	(5)	(6)	(7)	(8)	(9)
深度(米)	长度(米)	δ_1	δ_2	δ_3	δ_4	δ	δ	分类
0-50	50	0	1°30'	0	135°	1.18°	2.68°	III
50-100	50	1°20'	3°20'	135°	282°	4.40°	4.44°	V
100-150	50	3°30'	4°0'	285°	280°	0.94°	2.60°	III
150-190	20	4°0'	6°0'	280°	277°	2.59°	11.49°	V
190-200	10	5°0'	5°40'	277°	285°	0.68°	1.70°	III
200-250	50	5°40'	6°10'	285°	280°	0.72°	1.44°	I
250-300	50	6°10'	8°0'	280°	293°	2.59°	3.18°	V
300-350	50	8°0'	8°30'	293°	282°	1.57°	1.14°	III
350-400	50	8°30'	9°30'	282°	280°	0.18°	1.10°	III

Key:

1. Depth (M)
2. Length (M)
3. Degree
4. Degree/100M
5. Classification

According to the prospecting class and the actual situation of the example, we presume the subordination of each factor as follows:

$$M = (0.50, 0.15, 0.10, 0.25).$$

Finally, we get the result of the comprehensive evaluation:

$$\begin{aligned}
 I &= M \cdot B \\
 &= (0.50, 0.15, 0.10, 0.25) \cdot \begin{pmatrix} 0 & 0.01 & 0.82 & 0.17 & 0 \\ 0 & 0.62 & 0.37 & 0.01 & 0 \\ 0.18 & 0.13 & 0.05 & 0.09 & 0.55 \\ 0.14 & 0.14 & 0.59 & 0 & 0.33 \end{pmatrix} \\
 &= (0.14, 0.15, 0.50, 0.17, 0.25).
 \end{aligned}$$

Factors of the comprehensive evaluation must also be summed up as

$$0.14 + 0.15 + 0.50 + 0.17 + 0.25 = 1.21.$$

so that the final result is

$$\begin{aligned}
 &\left(\frac{0.14}{1.21}, \frac{0.15}{1.21}, \frac{0.50}{1.21}, \frac{0.17}{1.21}, \frac{0.25}{1.21} \right) \\
 &= (0.12, 0.12, 0.41, 0.14, 0.21).
 \end{aligned}$$

The above result indicates that this drilling area should belong to Class IV investment for prospecting area.

REFERENCE

1. Wang Peizhuang [1976 1014 8169], "Introduction to Fuzzy Mathematics," PRACTICE AND UNDERSTANDING OF MATHEMATICS, Vol 3 No 3, 1980.

12,909

CSO: 4008/1036

APPLIED SCIENCES

STRUCTURE OF NYLON 1010 DESCRIBED

Beijing GAOFENZI TONGXUN [POLYMER COMMUNICATIONS] in Chinese No 3, Jun 85
pp 202-206

[Article by Yang Xiaozhen [2799 1420 7201], Hu Shiru [7579 0013 1172],
Lu Yafei [0712 0068 7236], Zhu Shannong [2612 0810 6393] and Li Xiangkui*
[2621 4161 7608] of the Chemistry Institute of the Chinese Academy of
Sciences: "A Study of the Structure of Nylon 1010"; paper received on
22 April 1983]

[Text] Abstract: Nylon 1010 specimens prepared from both vitreous and melted crystalline states were studied by x-ray diffraction, infrared spectroscopy, differential scanning calorimetry, polarized optical microscopy, viscoelasticity and density. It was found that its structure is similar to that of Nylon 66. However, the lattice is greatly distorted when crystallized from the melt. Related problems were discussed and a hydrogen bond plane distortion model was introduced.

Nylon 1010 is a special engineering plastic in China. Its chain structure and polymeric structure have been studied.^{1,2} In order to understand the structure changes of Nylon 1010 crystallized from different states, we investigated the polymeric structures and crystals of specimens prepared from three different scanning calorimetry, polarized optical microscopy, viscoelasticity and density. The first type is quenched from a melt. The second type is crystallized isothermally from a vitreous state. The third type is crystallized from a melt. We found that, in addition to its crystal structure being similar to that of Nylon 66, the lattice of the third type crystal is severely distorted, resulting in its unique x-ray diffraction pattern as well as changes of the infrared band, melting peak and kinetic behavior. We believe that it is reasonable to explain this phenomenon by the distortion of the hydrogen bond plane.

*Current address is Chemistry Department, Zhengzhou University.

Experiments and Results

Sample Preparation

Nylon 1010 resin used was produced by Thompson-University (aster oil limit). It was dissolved in methanol and cast into a film on a glass plate. Then, it was placed in a fixture and immersed in a 130°C salt bath for 3-5 minutes. The three types of specimens were prepared as follows: type I was quenched to dry ice and heptane, type II was quenched in dry ice and heptane, crystallized isothermally at 150-180°C for several minutes to 1 day (under nitrogen), and then air cooled at room temperature, and type III was crystallized isothermally at 170-180°C under nitrogen for several minutes to 1 hour and then air cooled at room temperature.

Thickness Determination

A micrometer was used to measure six points and report the average. Sample thickness is 80-120 μ .

Density Determination

A density gradient tube with carbon tetrachloride and heptane was used. The density range is 1.004-1.101 g/cm³ and the resolution is 0.0001 g/cm³/cm. Specimens were measured at 25°C.

Polarized Optical Microscope

A Model IPT-6 optical microscope manufactured by Changchun Optical Instrument Plant with a magnifying power of 10 x 25 was used. Figures 1(A) and (B) show type I and II specimens. We did not see any spherocrystal. However, in type III specimen (C) the presence of spherocrystals is apparent. Based on color, they were identified as positive spherocrystals. The white line in (A) indicates some kind of molecular order which suggests that Nylon 1010 can easily crystallize. Even though it is quenched immediately after melting, it is not possible to obtain totally amorphous specimens.

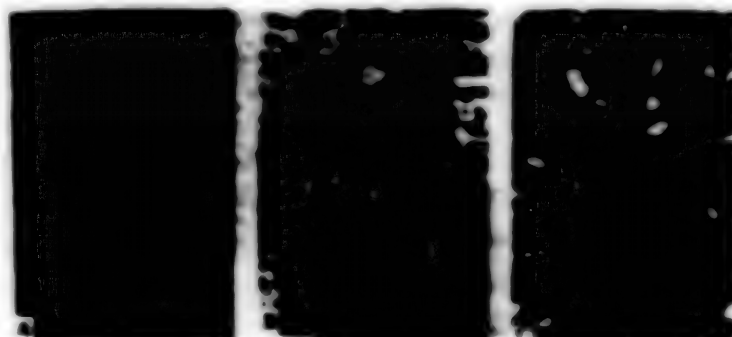


Figure 1. The Three Specimens Under a Polarized Optical Microscope: (A) Type I; (B) Type II; (C) Type III

X-ray Diffraction

A Scientific Electrical Equipment Model 3020 x-ray diffractometer with a Cu target, a Ni filter and a 2° incident slit was used. The sample film was adhered to a glass plate using Canadian glue. Typical x-ray diffraction patterns of these three types of specimens are shown in Figure 2. The crystal structure of Nylon 100 exhibits two distinct diffraction peaks at $2\theta^\circ$ and 24° , similar to those of Nylon 66.³ The arising diffraction planes are 100 and 010 + 110, respectively. The spacings are $d_{100} = 4.44\text{\AA}$ and $d_{010+110} = 3.71\text{\AA}$. There is an amorphous-like peak near 8.5° . The type I peak is diffused, indicating that the specimen is almost amorphous. The type II peak is similar to that of Nylon 66.³ The 100 plane diffraction peak is very high and sharp for type III and its 010 + 110 peak is small and diffused.

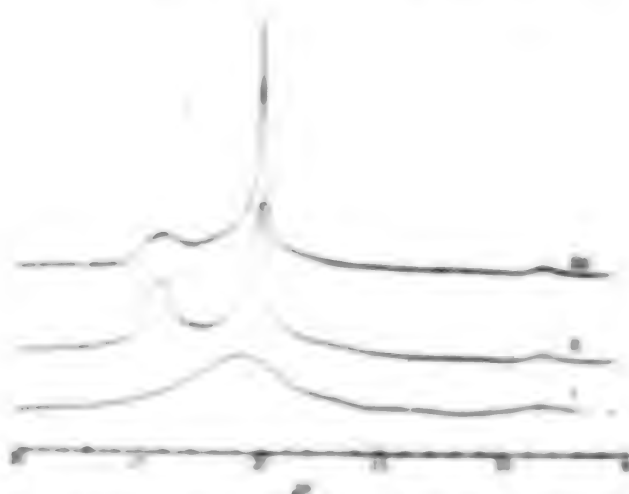


Figure 2. X-ray Diffraction Patterns for Three Types of Specimens

Infrared Spectroscopy

A Perkin-Elmer Model 180 infrared spectrophotometer was used to record the spectra. The resolution is 2 cm^{-1} . The bands at 810 and 1037 cm^{-1} are related to the vibration of the nylon skeleton.⁴ Figure 3 was prepared by normalizing absorbance and density as well as by taking sample thickness into account. Type I and II specimens seem to vary linearly with density, while the density of type III specimen seems to be independent of absorptivity.

Differential Scanning Calorimetry

A Perkin-Elmer Model DSC-11 calorimeter was used. The temperature rising rate was 20°C , the range was 5 mCal/sec and the nitrogen flow rate was 45 ml/min . Results obtained in the $400\text{--}500^\circ\text{K}$ range are as follows:

Figure 4 shows a high melting peak at near 471°K for type I and II samples, while the main melting peak for type III specimens appears at 461°K . The difference is apparent. This is because in the temperature rising process we have to experience the optimal crystallization temperature, which is estimated

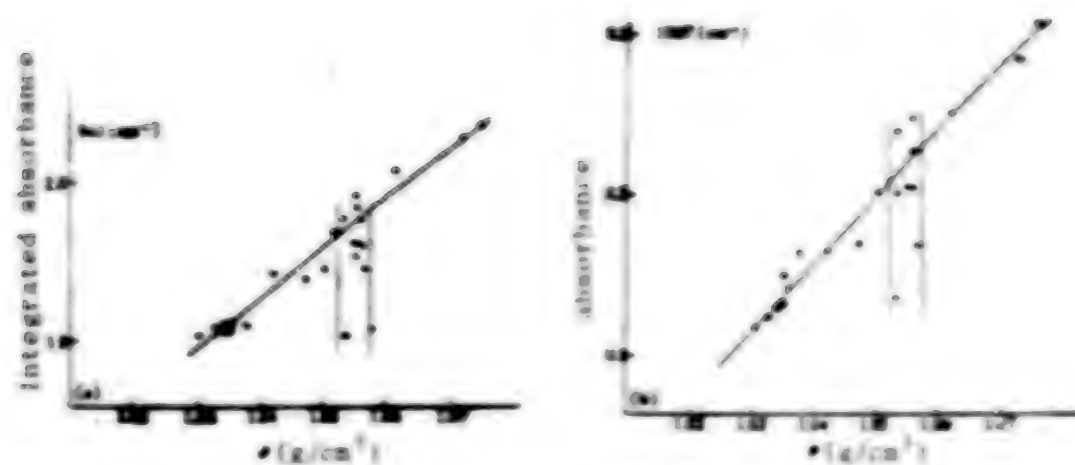


Figure 3. Relation Between the 940 cm^{-1} Band of Three Types of Nylon 1010 and Density

○ = type I; ● = type II; ▲ = type III

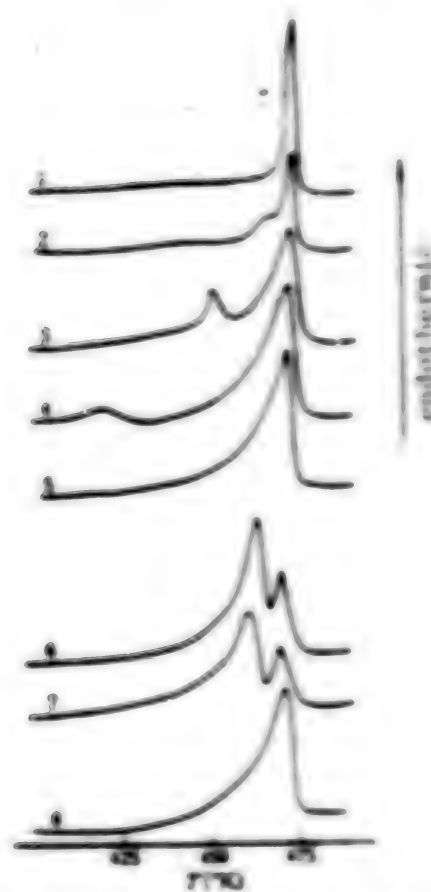


Figure 4. DSC Results of Three Types of Samples

Type I: 5 and 8; II: 1-6; III: 6,7

to be 165°C, despite that the temperature rising rate is high (20°C). Thus, crystallization occurred in DSC measurements. Of course, this happened to all samples. The melting peak of type I is a few degrees lower and the peak is wider than that of type II, which is more crystalline. This effect may be caused by the superposition of the crystal and the melt, as well as by the superposition of the relaxation of the crystallization process and the melting process. The small peak before the melting peak of type II specimens is basically related to the temperature of the thermal treatment. It is approximately 10°C higher than the thermal treatment temperature.

Viscoelasticity

A Model DDV-II Dongwang instrument was used. The frequency was 110 Hz, the temperature rising rate was 2°C/min and the temperature range was from liquid nitrogen temperature to 100°C. Figure 5 shows typical viscoelasticity patterns of these three types of samples. Within the temperature, there are three transition peaks. At approximately 70°C, it is the vitreous or α transition, -48°C corresponds to a β transition and -118°C is the γ transition. The two latter transitions correspond to the movement of the acid group and the carbon chain, respectively.⁶ Among all specimens tested, the α transition peaks of type III samples are always less than those of types I and II.

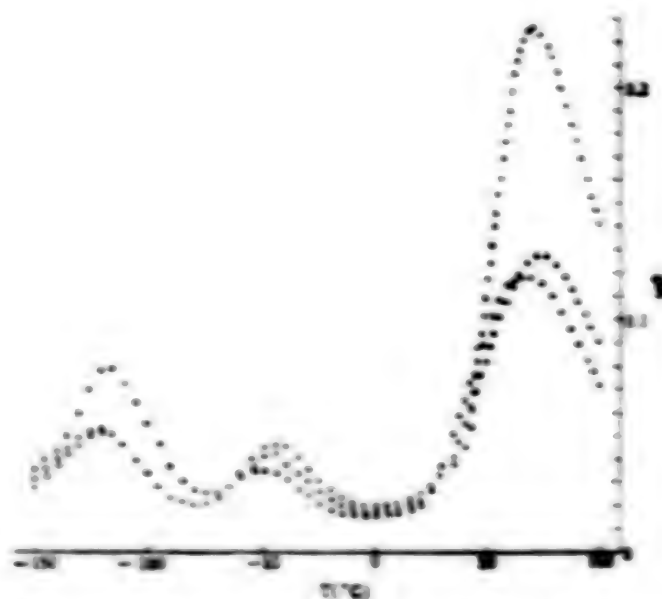


Figure 5. Viscoelasticity Patterns of Three Types of Samples
 ○ = I; □ = II; ▲ = III

Discussion

From the above results one can see that there are obvious differences between types II and III in terms of crystal structure, x-ray diffraction pattern, relation between skeletal vibration and density, enthalpy variation and kinetic characteristics. We believe that these differences indicate that they are different.

Type II is similar to other crystalline polymers crystallized from the vitreous state. The resulting spherocrystal is smaller. Normally a polymer forms a larger spherocrystal from the melting state. The lattice is orderly over a long span in three dimensions. Although type III specimens crystallized from the melt shows large spherocrystals, however, the height and half width of the two diffraction peaks are quite different. This indicates that it only grows orderly in one dimension and there is no apparent change in other directions. It may even decrease in the direction of the 010 + 110 plane, which is the hydrogen bond plane. It is a mesh created by linking hydrogen bonds among the stretched molecular chain. The direction of the hydrogen bond is the direction of the 100 plane. Therefore, the degree of orderliness in large type III crystals is nonuniform.

The loss peak τ_g/\max obtained from the viscoelasticity due to T_g transition is compared to the absorbance at 1807 and 940 cm^{-1} on the infrared spectra (see Figure 6). The intensity of the loss peak decreases with increasing intensities of these two absorption bands for type II specimens. However, type III samples are different. Although the infrared spectrum peak height varies a lot, yet the loss peak remains unchanged. Their loss peaks are lower than those of type II samples, indicating that there is less noncrystalline area in type III samples. At the two upper points for type II specimens, the densities are higher than those of type III samples. This abnormal effect is attributed to the distortion of the crystal structure of type III specimens. The DSC melting temperature of type III, which characterizes its crystal structure, is approximately 10°C lower than that of type II, reflecting a distorted structure as well. The structure distortion in the geometric space leads to the lowering of internal polymerization energy. The density decrease in the crystalline region is also understandable.



Figure 6. Infrared Absorbance vs. $1/\tau_{\max}$ for Two Types of Samples

(Absorbance $\times 0.1$)

Hosemann investigated the distortion of crystalline polymers in depth. It usually belongs to type II defects. The lattice defect we detected is more severe than that he described. Moreover, the distortion in various directions is different. The cause and explanation of the formation of this structure and a description of the picture of the distorted structure are as follows.

Because the activation energy of molecular chain movement is lower for type III crystals, the chain segment moves faster and easier. In this case, the free energy for nucleus formation is relatively high. The number of nuclei formed is less, causing the molecular chain to stretch forming a larger hydrogen bond cross-linked plane. This naturally makes the diffraction peak of the 100 crystal plane high and narrow. The hydrogen bond mesh plane is orderly aligned under the influence of van der Waal force which is much weaker than hydrogen bonding force. It is comprehensible that this effect causes a wide distribution of crystal plane spacing. However, experimental results showed much more. The fact that the absorbance of the infrared band corresponding to the skeletal vibration of type III specimens is independent of density indicates that the molecular chains in the crystalline region are not all in a planar saw-tooth structure. This makes it impossible to form a real hydrogen bond plane. At around 181°C, it already reaches the melting temperature of hydrocarbon chain macromolecules. In the hydrogen bond plane of Nylon 1010 with a long hydrocarbon chain, van der Waal force is not enough to control the hydrocarbon movement. However, the hydrogen bond is still very strong which leads to the wide fluctuation of spacing of hydrogen bond plane and the significant distortion of the hydrogen bond plane. Consequently, the effect that the diffraction peak of the 010 + 110 crystal plane of the larger type III spherocrystal is not increased can be explained. This effect is not apparent for type II specimens because a large number of nuclei is formed after quenching. When it is isothermally recrystallized, even at 180°C, it is not possible to make all the nuclei disappear. Consequently, it is difficult to form a larger hydrogen bond mesh surface. Because the hydrogen bond surface is smaller, the scale of orderliness is small in all directions. The effect of hydrogen bond surface distortion is reduced and the drastic difference of distortion along various directions is also reduced. Of course, it belongs to the second kind of lattice distortion specified by Hosemann.

Meaningful information can also be obtained from the β and γ transition peaks measured kinetically. β peak corresponds to the motion of the nonhydrogen bonded amide group. In Figure 5, the β peak for type III specimens is the smallest, indicating that there are more hydrogen bonds in the crystalline region which is in agreement with its high degree of crystallinity. γ peak corresponds to the carbon chain movement. The γ peak for type III specimen is not the smallest, indicating that the number of orderly carbon chains in the lowest ground state is not proportional to the large crystalline region. In other words, there are irregular carbon chains in the crystalline region. This kinetic characteristic also supports the above hydrogen bond plane distortion model.

Acknowledgement

The authors wish to thank Associate Research Fellows Xu Ruifu [1776-1843-1133] and Qi Zongneng [1344-1150-5174] for the beneficial discussion on the results.

REFERENCES

1. Yang Xiaozhen, Lu Yafei, Zhu Shannong and Li Xiangkui, POLYMER COMMUNICATIONS, 1982, (6), 469.
2. Unpublished results.
3. Haberkorn, H., Illers, K.H. and Simak, P., COLLOID AND POLYMER SCI., 1979, 257, 820.
4. Woodward, A.E. Sauer, J.A., Deeley, C.W., and Kline, D.E., J. COLLOID SCI., 1957, 12, 363.
5. Rosemann, R. and Bagchi, S.K., "Direct Analysis of Diffraction by Matter," North Holland, Amsterdam, 1962, pp 239-246.
6. Qian Renyuan [6929 0086 0337], Qi Zongpeng and Wu Linsheng [0702 2651 3932], POLYMER COMMUNICATIONS, 1985, 7, 291.

12553

CSO: 4008/1059

APPLIED SCIENCES

DIFFERENTIAL ELASTIC SCATTERING CROSS SECTIONS OF 14.2 MeV NEUTRONS FROM NIOBIUM

Beijing YUANZHE WULI [CHINESE JOURNAL OF NUCLEAR PHYSICS] in Chinese Vol 7 No 2, May 85 pp 106-111

[Article by Li Jingde [2621 2529 1795], Xie Daquan [6200 1129 0356], Li Yexiang [2621 2814 4382], Zhang Di [1728 2769], Wang Shiming [1769 0013 2494] and Cao Jianhua [2580 1696 5478]]

[Text] 1. Introduction

Elastic scattering is the primary physical process in the interaction between fast neutrons and matter. Accurate data of differential elastic scattering cross sections not only is valuable in the design of nuclear reactors and in other nuclear projects, but also provides a reliable basis for adjusting optical model parameters, verifying theoretical models, and predicting measured data in energy deficient zones.

The superior physical properties of niobium makes it an attractive construction material for reactors. In fusion reactors, there is growing interest in using niobium as the cover layer for the fusion plasma; consequently, niobium neutron data is becoming increasingly more important. In the literature, there have been two reported measurements of differential elastic scattering cross sections of niobium fast neutrons in the neighborhood of 14 MeV: the measurement by Western, et al., at 20 different angles between 20° and 140°,¹ and the measurement by Kammerdiener at 18 different angles between 25° and 145°. The two sets of data differ substantially for angles less than 45°, and there is no experimental data below 20°. There are also significant differences between the experimental values, the theoretical values, and recommended values of the total elastic scattering cross sections. The integrated elastic scattering cross section given by Western, et al., is 1.77b, which obviously does not agree with the value 2.12b obtained by Angeli, et al.,¹ using mass system theory; the calculated cross sections based on the optical model given by Smith, et al., fall between 2.3b and 3b; the recommended values are between 1.77b and 2.3b; thus, these results differ by 25 percent or greater.²⁻⁷ The large discrepancies indicate that there is clearly a need to improve the quality of the experimental data. In the evaluation report, Smith, et al., pointed out that by improving the measurement of 14 MeV elastic scattering cross sections, particularly in the range 0°-45°, the quality of evaluation can be significantly improved.

In view of the importance of the data in the 14 MeV energy zone for applied and theoretical research, and in order to clarify the differences of experimental results and to fill the void of small angle data, we have made laboratory measurements of the differential elastic scattering cross sections of 14.2 MeV neutrons in niobium at 28 different angles between 6° and 150° ; these angular data are fitted with Legendre polynomials to obtain the integrated elastic scattering cross sections.

II. Experimental Setup and Measurement Technique

The experiment was conducted on the 400 KV high-voltage multiplier at the Sichuan University Nuclear Science Research Institute using the associated particle time of flight method; the experimental setup is shown in Figure 1. The 200 KeV deuterium beam generated by the high-voltage multiplier bombards the tritium-titanium target, and produces neutrons through $T(d,n)^4He$ reaction. The "associated" α particles are detected using a 50 μ m thin-film plastic scintillator which is coupled to the 56 AVP type photoelectric multiplier. This detector is positioned at 90° relative to the deuterium beam; the corresponding neutron beam which is constrained by the rectangular diaphragm is located 82° relative to the deuterium beam; the average neutron energy is 14.2 MeV.

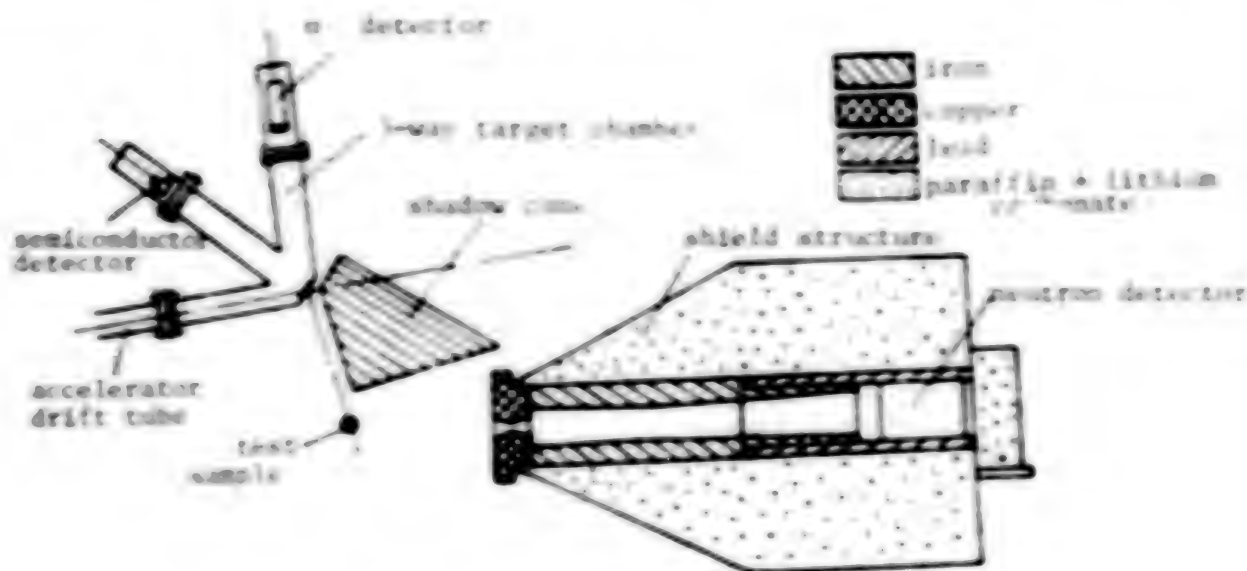


Figure 1. Experimental Setup

In this experiment, two different neutron detectors were used. The first consists of a ST451 liquid scintillator 5 cm in diameter and 5 cm thick which is coupled to the 56 AVP photoelectric multiplier; it is used to measure the position and shape of the associated neutron beam. The second consists of a ST451 liquid scintillator 10.4 cm in diameter and 5 cm thick which is coupled to the XP2041 photoelectric multiplier; it is used to measure the differential elastic scattering cross section. In order to reduce background noise, the neutron detector is located inside the shield structure. The shield structure is 1.3 m

in diameter, 2 m long, and filled with paraffin and lithium carbonate in equal proportion plus an appropriate amount of ethylene trichloride; the inner layer is a 5 cm thick lead ring. To minimize the interference due to hole-wall scattering, the alignment hole is made into a shape of a double frustum cone. The shield weighs 3.5×10^4 kg, and is carried on an air-cushioned cart; it can be rotated freely about the axis of the test sample.

The position and shape of the associated neutron beam are carefully measured in both the horizontal and vertical directions. The associated beam has a horizontal opening of 21.6° (see Figure 2) and a vertical opening of 21.7° . With the aid of a bidirectional laser collimator, the scattering test sample can be placed in the center of the associated beam so it is surrounded by the beam. The axis of symmetry of the test sample is perpendicular to the beam axis of symmetry; the center of the test sample is 71 cm from the target center, and the flight distance of the scattering neutron is 230 cm.

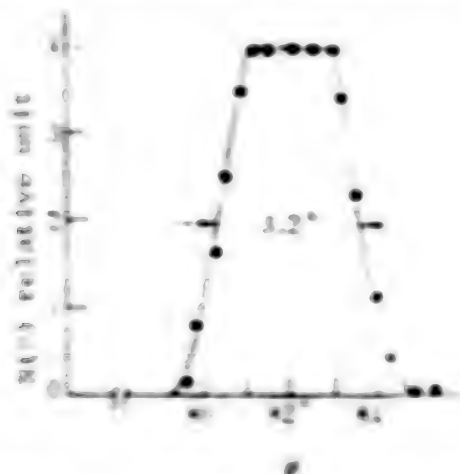
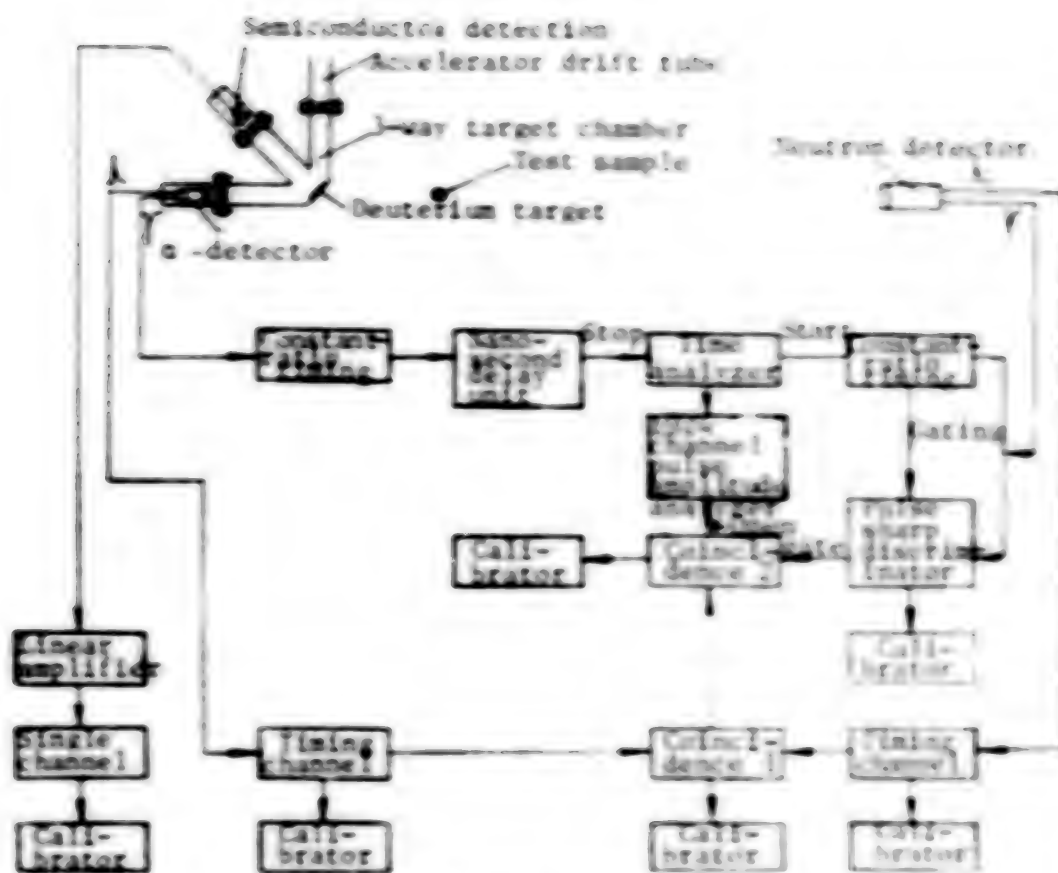


Figure 2. Position and Shape of the Associated Beam in the Horizontal Direction

The shadow cone absorber is made of stacked iron bricks; it is longer than 40 cm, and its shape and position are determined by the geometry of the measuring angles.

The electronic circuit diagram is shown in Figure 3. A fast signal with very short time constant is generated from the anodes of the photoelectric multipliers of the α detector and the neutron detector, and passed through a constant-ratio timing device to provide timing signals for the α particles and neutrons. The neutron timing signal with lower count rate is used as the "start" signal for the timing analyzer, and the α timing signal with higher count rate is used as the "stop" signal after an appropriate delay. The distribution of the neutron flight time is converted by the timing analyzer into corresponding pulse amplitude distribution, and then processed by the 1024-channel pulse amplitude analyzer.



From the 13th pole of the α detector photoelectric multiplier, a linear signal is extracted and passed through the timing channel with the proper threshold and window width to produce the required α particles; they are recorded by a calibrator which is also used to monitor the flux of the neutron beam. From the 12th pole of the neutron detector photoelectric multiplier, a linear slow signal is extracted and filtered through the single timing channel; the threshold value of the spectrometer is selected based on measurement needs. A pulse shape discriminator is used to separate the neutrons from γ particles and to eliminate γ background. The output from the α timing channel, the neutron linear timing channel, and the pulse shape discriminator are passed through a two-stage adjustable-delay double-coincidence circuit to provide the open signal for the multichannel pulse amplitude analyzer where coincidence spectral measurements are made.

The scattering sample is a ^{115}In metallic cylinder 2 cm in diameter and 4 cm in height; its purity is better than 99.5 percent. Alternate measurements

of the flight time spectrum with the test sample and the background spectrum without the test sample are made at 26 different angles between 6° and 150° , where the scattering angle is measured from the axis of the associated neutron beam. Two or three repeated measurements are made at most angles with good results of repeatability. All measurements are normalized with respect to the monitor count. During the entire measurement process, the stability of the energy threshold of the spectrometer is being constantly monitored.

The neutron count at 0° angle without the test sample is also measured at the same count rate.

III. Data Processing and Correction

For the geometric configuration of this experiment, the differential elastic scattering cross section is computed according to the following formula:

$$\frac{d\sigma}{d\Omega}(\theta) = \frac{N(\theta)}{M(\theta)} \cdot \frac{M(0)}{N(0)} \cdot \frac{\epsilon(\theta)}{\epsilon(0)} \cdot \left(\frac{lL}{l-L}\right)^2 \cdot \frac{1}{N_0} \quad (1)$$

where $N(\theta)$ is the net elastic scattering neutron count at angle θ after compensating for the background; $N(0)$ is the neutron count at 0° without the test sample; $M(\theta)$ and $M(0)$ are, respectively, the total count of γ associated particles corresponding to the measurements $N(\theta)$ and $N(0)$; $\epsilon(\theta)$ is the detection efficiency of elastic scattering neutrons at angle θ ; $\epsilon(0)$ is the detection efficiency of primary neutrons at 0° ; l is the distance between the test sample and the target center; L is the distance between the test sample and the detector; N_0 is the total number of nuclei of the test sample. N_0 can be determined by weighing the test sample using a precision scale. Thus, the problem reduces to one of measuring the other physical quantities mentioned above.

In this experiment, we made the approximation $\epsilon(\theta)/\epsilon(0) = 1$ because the energy of the scattering neutrons is very close to that of the incident neutrons; the resulting error in the differential cross section is less than 1 percent.

The large amount of measurements of background spectra indicate that above 20° , the background is randomly distributed with respect to the flight time; there is no evidence of time-correlated structure. The accidental coincidence background on the right side of the elastic peak with test sample is generally consistent with that with the test sample removed. Below 20° , due to geometric constraints, the scattering effect between the target lining and air cannot be totally eliminated; also, the angular distribution of this type of scattering is front loaded, hence the corresponding elastic peak position on the background spectrum has a weak structure. The background attenuation due to the presence of test sample is taken into consideration in data processing.

Correction is made to the elastic scattering neutron peak based on the shape of the primary spectrum, thus the contribution of the nonelastic scattering

neutrons is removed. The loss in count caused by the dead time in the electronic circuit is also corrected. In addition, Monte-Carlo method⁸ is used to correct for neutron flux attenuation, multiple scattering, and limited angular resolution of the system.

IV. Results and Discussion

The calculated and corrected differential elastic scattering cross section is shown in Figure 4. The total error is between 4.7 and 8.5 percent. An error analysis is presented in Table 1.

Table 1. Error Analysis

Error source	Error, percent
Count statistics	1.5-7.2
Neonlastic correction	+2
Geometric factor	+1
Correction for dead time in electronic circuit	+1
Detector efficiency	+1
Correction for flux attenuation and multiple scattering	3.6
Number of nuclei in test sample (including error in weight measurement)	0.5
Total	4.7-8.5

For comparison, Figure 4 also shows the experimental data of References [1,2] and the theoretical angular distribution calculated using the optical model given in Reference [9].

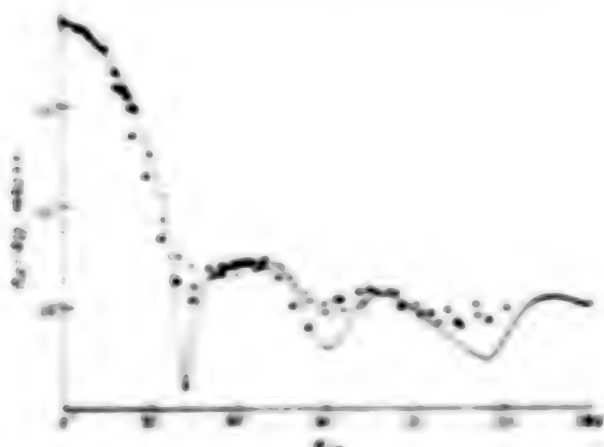


Figure 4. Differential Elastic Scattering Cross Section of 16.2 MeV Neutron From ^{235}U

x--Ref 1 16.7 MeV
o--current experiment

▲--Ref 2 14 MeV
solid curve represents the theoretical result based on optical method

The measured angle distribution data from this experiment are supplemented by computed data for small and large angles using the optical mode; at 0° , they satisfy the Wick limit¹¹:

$$\frac{d\sigma}{d\Omega}(0^\circ) > \left(\frac{\sigma_{\text{tot}}}{4\pi}\right)^2 \quad (2)$$

where k is the wave number, and σ_{tot} is the total cross section.

By approximating the above data using optimum Legendre polynomials, and integrating the approximating curve, we can calculate the integral elastic scattering cross section to be 2083 ± 76.6 mb. The expression of Legendre polynomials used to represent the differential elastic cross section is

$$\frac{d\sigma}{d\Omega}(E, \theta) = \frac{\sigma_{\text{el}}(E)}{4\pi} \sum_{l=0}^L (2l+1) f_l(E) P_l(\cos \theta) \quad (3)$$

where θ is the arc length of the mass system ($0 \leq \theta \leq \pi$), $f_l(E) \approx 1$, and the integral elastic scattering cross section is $\sigma_{\text{el}}(E) = 2\pi \int_0^\pi \frac{d\sigma}{d\Omega}(E, \theta) \sin \theta d\theta$.

The measured integral elastic scattering cross section values from this experiment are in good agreement with the value of 2036.65 mb computed in Reference [9] using optical model parameters and with the value of 2120 mb obtained in Reference [3] using mass system theory.

In order to obtain reliable data on integral elastic scattering cross sections, it is necessary not only to improve the measurement of differential cross sections, but also to make reasonable assumptions about differential cross sections in large and small angular regions where experimental data are lacking. This issue requires further discussion.

Due to constraints in experimental conditions, there is a lack of experimental data in both the small-angle region (0° - 20°) and the large-angle region (160° - 180°). In the past, manual extrapolation techniques, extrapolation using Legendre polynomial approximation, or analytical methods based on theoretical models have been used to fill these gaps. For low incident neutron energy, these methods yield similar results because variations in the angular distribution are generally quite small. However, as the energy level increases, the angular distribution becomes more and more front loaded and large differences between these methods become apparent; generally speaking, the higher the energy level and the heavier the nuclear weight, the larger the differences. For example, our calculations show that in the integral elastic scattering cross section of Niobium in the neighborhood of 14 MeV, more than 70 percent of the contribution comes from the region below 20° , where no experimental data existed prior to this measurement. Western, et al., obtained the elastic scattering cross section of 1770 mb by extrapolating from the blackcore model¹; Smith, et al., applied extrapolation and interpolation processing to the same angular distribution data to obtain the value of 2050 mb¹²; the difference between the two is 280 mb.

We believe that a reasonable approach would be to use the Wick limit at 0° , and fill the data gaps at small and large angles using optical model calculations, then apply Legendre polynomial approximation to obtain the integral elastic scattering cross sections.

In summary, the main contribution of this paper is to provide experimental data in the small-angle region, and to improve the reliability of integral elastic scattering cross sections by using an improved method of calculation.

Thanks are due to Comrade Wan Hongshang for calculating the theoretical optical model curve, and to members of the high-voltage multiplier group for their support in carrying out this experiment.

REFERENCES

1. Western, G.T., et al., CONE-440315, 1, 1966, p 875.
2. Kammerdiener, J.L., UCRL-51217, 1971.
3. Angeli, I., et al., PRIVATE COMMUNICATION (1973).
4. Smith, A.B., et al., ANL-NOP-6, 1974.
5. Hermendorf, D., et al., KE20, 1977, p 166.
6. Allen, H.S., et al., GA-8171, 1967.
7. Bazaryants, N.O., et al., AD. KONSTANTY, 8, 61 (1972).
8. Lin Yude, et al., SCIENCE AND TECHNOLOGY, (1134) (1981).
9. Rapaport, J., et al., NUCL. PHYS., A335, 15 (1979).
10. Wick, G.C. PHYS. REV., 73, 1439 (1949).

3012
CSO: 4008/395

APPLIED SCIENCES

DIFFERENTIAL CIRCUIT MODEL FOR TURBOMOLECULAR PUMP BLADE

Beijing ZHENKONG KEXUE YU JISHU [VACUUM SCIENCE AND TECHNOLOGY] in Chinese, Vol 4, No 5, Sep 84 pp 311-318, 334

[Article by Chu Jiguo [0328 4949 0948] and Sun Yunlong [1327 0061 7891] of Fudan University: "Differential Circuit Model of Turbomolecular Pump Blade and Calculation of Combination Turbine Compression Ratio"]

[Text] Based on a differential circuit model for turbomolecular pump blades, the simple relation of its compression ratio versus the leak gap and impeller spacing was obtained. In addition, a comprehensive correction method for compression ratio was introduced. Calculated results agreed with experimental data well. Furthermore, the relation between compression ratio and impeller spacing is not as close as predicted by the molecular drag theory.

The compression ratio of a single stage turbomolecular pump has already been derived from the Monte Carlo method[1] and statistical theory[2,3]. The compression ratio of a combination turbomolecular pump is generally believed to be simply the product of the compression ratios of various stages. However, the calculation usually deviates from the experimental data. On the one hand, it is because the effect of leak gap and separation is not included in the calculation. Another reason is due to error made in measuring the compression ratio.

Becker[4] used the molecular drag theory to analyze the leakage problem. However, this is not solved because he introduced too many correction factors and the molecular drag theory itself is not rigorous[2,3]. In this work, based on equilibrium equations, the relation of compression ratio versus leak gap and impeller separation was obtained by introducing a differential circuit model for the blades. Then, the "dead area" correction for the compression ratio was discussed. Corrected results showed that the effect of impeller separation on compression is not as high as predicted by Becker's molecular drag theory. The theoretical values also agreed very well with the experimental data.

1. Effect of Leak Gap on Compression Ratio of Single Stage Turbine

In order to ensure the safe operation of a turbomolecular pump, there is usually a 0.5-1.0 mm gap between the rotating part and the stationary part of

the pump. This gap becomes a leakage path which lowers the compression ratio of the turbine. Because drive rate is defined as the volume of flow per unit time when there is no pressure difference across the turbine, therefore, the leak in principle will not affect the working rate.

Figure 1 shows a schematic diagram of a cross section of a single stage turbine. From the figure one can see that the leak gap l is equivalent to a short circuit in the pumping line.

In equilibrium, the pumping rate is zero and the following equation is valid:

$$N_1 \Delta L_1 + N_2 \Delta L_2 = N_3 \Delta L_3 \quad (1)$$

where N_1 and N_2 are the number of molecules incident upon a unit area of the blade per unit time on the inlet and exhaust side, respectively. ΔL_1 and ΔL_2 are the forward and reverse transport probabilities, respectively. ΔL_3 is the transport probability of the leak gap. S and A represent the section area and leakage area, respectively.

From equation (1) we can find that the compression ratio of the turbine is

$$K = \frac{P_2}{P_1} = 1 - \frac{K_1 - 1}{1 + \frac{\Delta L_2}{\Delta L_1}} \quad (2)$$

where $K_1 = \frac{\Delta L_1}{\Delta L_2}$

Therefore, as long as the transport probability of the leak gap is known, the relation between the compression ratio of a single stage turbine and the leak gap can be quantitatively determined. As a matter of fact, with the exception of increased leak gap l , the situation is identical to that of finite blades without leakage. In approximation, we consider that this is a problem to add a thin wall flow conductance with an area A to the finite blade leak-free situation, i.e. $\Delta L_3 = 1$. The compression ratio in question should be understood as that of the finite blade [2,3]

$$K_1 = K_0^{1/\epsilon} \quad (3)$$

where $\epsilon = \frac{d}{2l}$, d is the distance between two neighboring blades, and l is the length of the blade.

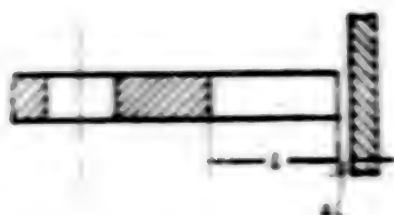


Figure 1. Cross-section of a Single Stage Turbomolecular Pump Impeller

From equation (2) we know that the leak will cause the compression ratio to go down. With the same leak μ_{40} , its effect on a higher compression ratio turbine is larger.

Let $l=12$ mm, $l'=0.5$ mm, angle of inclination of the blade $\alpha=20^\circ$, specific speed $\mu=0.5$, aspect ratio $r/b=1.0$, and blade width $b=10$ mm. The corresponding transport probabilities are [3]

$$S_1=0.522, S_2=0.242$$

We can determine that $X=1.99$, $K_1=2.7$ and $K_2=2.03$, i.e., the leak lowers the compression ratio by 8%.

II. Effect of Leaks in Multi-stage Turbomolecular Pump on Its Compression Ratio - Differential Circuit Model of the Blade

Figure 2 shows the leak in a combination turbomolecular pump. The leak of the moving turbine is on the outer side and that of the stationary turbine is on the inner side.

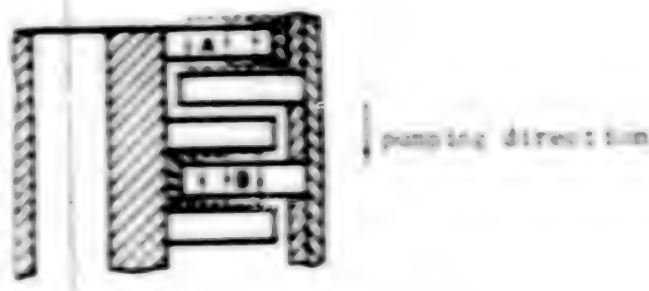


Figure 2. Cross-section of a Combination Turbomolecular Pump

Because neighboring impellers are very close, the pressure drop caused by the radial flow of the gas molecules along the gas van no longer be neglected. For this reason, the pressures on both sides of an impeller are no longer constants. Instead, the compression ratio of the turbine is a function of the blade length. In the following we will introduce a differential circuit model to discuss this problem.

Let us assume that

(1) the geometric and operating parameters along the blade are identical, i.e., pumping capability and forward and reverse transport probabilities are the same; and

(2) the radial flow conductance of the leak gas is the same.

As we know that a vacuum system and an electronic circuit have the following corresponding relations as shown in the following table.

<u>vacuum system</u>		<u>electronic circuit</u>	
flow conductance	F	electrical conductance	Y
pressure	P	voltage	V
flow rate	Q	current	I
vacuum pump		power source	

Let the pressure intensities on the inlet and exhaust side of turbine A in Figure 2 be P_1 and $P_2(X)$, respectively. The spacing between the pumping elements (i.e. the space between two neighboring blades) is $\tau = 1$. Based on the theory of transport probability, for any differential element dx of each pumping element along the length of the blade we have

$$N \cdot W \cdot dx = N_1 I_{12} dx - N_2 I_{21} dx \quad (4)$$

where W is the coefficient of the differential pumping element dx .

When the compression ratio is calculated, the effective drawing rate is zero. Hence, the net flow rate corresponding to the differential pumping element should be equal to the increment of the radial flow rate at the gap, i.e.

$$dQ_r(x) = P_1 \cdot \frac{1}{4} v_{th} W dx = P_1 \cdot \frac{1}{4} v_{th} I_{12} dx - P_2(x) \cdot \frac{1}{4} v_{th} I_{21} dx \quad (5)$$

where $Q_r(x)$ is the radial flow rate assigned to each pumping element by the gas and v_{th} is the average thermal velocity of the gas molecule.

For convenience, we define

$$F_{12} = \frac{1}{4} v_{th} I_{12} \quad (6)$$

$$F_{21} = \frac{1}{4} v_{th} I_{21} \quad (7)$$

where F_{12} and F_{21} have the dimension of flow rate.

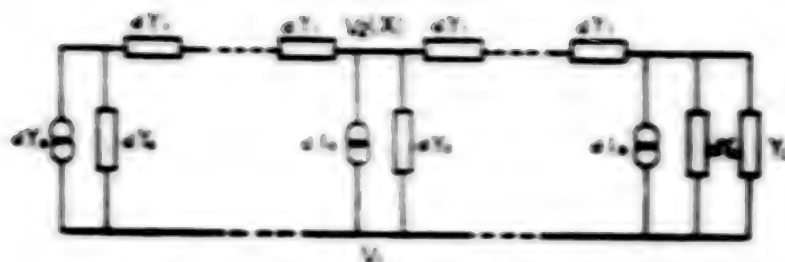


Figure 3. Differential Circuit Model of an Edge Turbine Blade

Substituting equations (6) and (7) into equation (5), we get

$$\begin{aligned} \frac{dU_1(x)}{dx} &= P_1 F_{11} \cdot \frac{1}{l} - P_2(x) \cdot F_{12} \cdot \frac{1}{l} \\ &= \frac{U_1}{l} - \frac{F_{12}}{l} (P_1(x) - P_2) \end{aligned} \quad (8)$$

where

$$U_1 = P_1 (F_{11} - F_{12}) \quad (9)$$

which is the maximum pumping rate of the element. When the pressure on the inlet side remains unchanged, U_1 is a constant.

According to equation (8), we can make an equivalent differential electronic as the one shown in Figure 3 for the pumping element. The parameters of the circuit in Figure 3 and those of the vacuum system are related as follows:

$$\begin{aligned} dI_1 &= \frac{dx}{l} \cdot I_{11}, & dY_1 &= \frac{dx}{l} \cdot F_{111} \\ dY_2 &= \frac{1}{dx} \cdot F_{12}, & Y_1 &= F_{11} \\ I_1(x) &= U_1(x), & V_1 &= P_{11} \\ V_2(x) &= P_2(x). \end{aligned}$$

From the equivalent circuit shown in Figure 3, we can list the following equations

$$dI_1(x) = dI_1 - (Y_1(x) - Y_2) \cdot dV_1 \quad (10)$$

$$dV_2(x) = -\frac{l_2 - x}{dY_1} \quad (11)$$

and condition

$$I_1(0) = 0 \quad (12)$$

By re-writing equation (10)-(12) into vacuum parameters, we get

$$\frac{dU_1(x)}{dx} = \frac{U_1}{l} - (P_2(x) - P_1) \frac{F_1}{l} \quad (13)$$

$$\frac{dP_2(x)}{dx} = -\frac{U_1(x)}{l \cdot F_1} \quad (14)$$

$$U_1(0) = 0 \quad (15)$$

By differentiating equation (13) and substituting it into (14), we get

$$\frac{d^2 U_1(x)}{dx^2} = -\frac{F_1}{l \cdot F_1} U_1(x) \quad (16)$$

Then, from equations (15) and (16), $U_1(x)$ is determined. Afterward, $U_1(x)$ is plugged back into equation (14) to determine $P_2(x)$. Then, the compression ratio can be determined by

$$K(x) = \frac{P_2(x)}{P} = K - \frac{(K-1)F_1 \cdot \cosh\left(\sqrt{\frac{F_1}{F_2}} \cdot \frac{x}{l}\right)}{\left(\sqrt{F_1} \cdot P_1 + F_1 \cdot \cosh\sqrt{\frac{F_1}{F_2}}\right) \sinh\sqrt{\frac{F_1}{F_2}}} \quad (17)$$

By averaging equation (17) with respect to the blade length, we get

$$K = K - \frac{K-1}{\frac{F_1}{F_2} + \sqrt{\frac{F_1}{F_2}} \cdot \cosh\sqrt{\frac{F_1}{F_2}}} \quad (18)$$

Because any practical pumping element satisfies $\sqrt{\frac{F_1}{F_2}} \gg 2$, we have

$$\cosh\sqrt{\frac{F_1}{F_2}} \approx 1.$$

Equation (18) can be simplified as

$$K = K - \frac{K-1}{\frac{F_1}{F_2} + \sqrt{\frac{F_1}{F_2}}} \quad (19)$$

In the following, we will discuss a few special cases:

1. The impeller spacing $b \rightarrow \infty$, i.e. a single blade turbine. In this case, the radial flow conductance of the gap is infinite, i.e. $F_1 \rightarrow \infty$. Therefore, the second term of the denominator in equation (18) becomes

$$\sqrt{\frac{F_{10}}{F_1}} \cdot \coth \sqrt{\frac{F_{10}}{F_1}} = 1.$$

The compression ratio of a pumping element, which is the compression ratio of the impeller, is

$$K = K - \frac{F(K-1)}{F_1 - F} = 1 + \frac{K-1}{1 + \frac{1.47}{A \cdot L_1}}$$

which is identical to equation (2). Notice that equation (19) does not apply to this special case, therefore, it cannot be used to find the compression ratio.

2. The impeller spacing $b=0$, i.e. the gap of a combination turbomolecular pump is the minimum. In this case, $F_1=0$. By substituting it into equation (19) we get

$$K = K$$

which shows that the leak has no effect on the compression ratio. Our understanding of this conclusion is that when the separation is zero, the effect of the leak is concentrated at the gap. It is not spread outward and the averaging effect can be neglected.

The middle turbine shown in Figure 1 can be expressed by the equivalent circuit shown in Figure 4. According to electronic circuit theory, Figure 4 is equivalent to Figure 3. By changing the electrical conductance dY_1 to $1/2(dY_1)$ in Figure 3, we find that the radial flow rate $U_1(x)$ and the pressure on either side of the impeller are identical to those in Figure 4. However, the radial pressure drop $P_2(0)-P(x)$ on the exhaust side is increased by one fold. In order to distinguish them, the voltage in Figure 3, i.e. the pressure, carries an * when we use the equivalent circuit in Figure 3 to solve the problem. The real pressure intensities on both sides of the impeller should be

$$P_1(x) = P_1^*(x) + \frac{1}{2}[P_1^*(0) - P_1^*(x)] \quad (20)$$

$$P_2(x) = P_2^* + \frac{1}{2}[P_1^*(0) - P_1^*(x)] \quad (21)$$

Hence, the compression ratio is

$$K(x) = \frac{P_1(x)}{P_1^*} = \frac{P_1^*(x) - \frac{1}{2} [P_1^*(0) - P_1^*(x)]}{P_1^* - \frac{1}{2} [P_1^*(0) - P_1^*(x)]} \quad (22)$$

for ease of use, equation (22) can be simplified as

$$K(x) = \frac{P_1^*(x)}{P_1^*} \quad (23)$$

Obviously, the condition for equation (23) to be valid is

$$P_1^*(x) \geq \frac{1}{2} [P_1^*(0) - P_1^*(x)]$$

$$P_1^* \geq \frac{1}{2} [P_1^*(0) - P_1^*(x)]$$

Most practical turbines can meet the above condition. Therefore, we can determine the compression ratio by directly using equation (17).

$$K(x) = K - \frac{(K-1)F_1 \cdot \tanh\left(\sqrt{\frac{2F_1}{F_1}} \cdot \frac{x}{l}\right)}{\left(\sqrt{\frac{F_1}{F_1}} + F_1 \cdot \tanh\sqrt{\frac{2F_1}{F_1}} \cdot \tanh\sqrt{\frac{2F_1}{F_1}}\right)} \quad (24)$$

By averaging equation (24) with respect to the blade length, we get

$$K_t = K - \frac{(K-1)F_1}{F_{11} + F_1 \sqrt{\frac{2F_1}{F_1}} \tanh\sqrt{\frac{2F_1}{F_1}}} \quad (25)$$

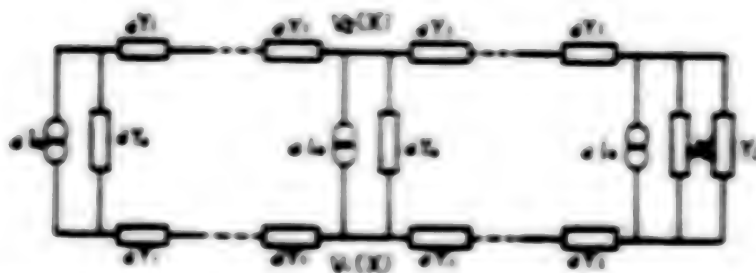


Figure 4. Differential Circuit Model for the Middle Turbine Blade

Similarly, because a practical pumping element satisfies the condition $\sqrt{\frac{F_{11}}{F_1}} > 2$, therefore, equation (25) can also be simplified as

$$K = K - \frac{K-1}{\frac{F_{11}}{F_1} + \sqrt{\frac{2F_1}{F_1}}} \quad (26)$$

When the spacing $h = \infty$, from equation (25) we get

$$K = 1 + \frac{K-1}{1 + \frac{1.4F_1}{4F_{11}}}$$

When the spacing $h = 0$, from equation (26) we get

$$K_1 = K$$

which is identical to turbine A on the edge.

We will discuss the choice of the value of the flow conductance F_{11} . From earlier analysis we understand that the radial flow in the gap due to leakage is an internal motion of the gas molecules. It is not limited by the inlet aperture. Therefore, its flow conductance should be calculated by using the formula for a long and narrow slit [6]

$$F_1 = \frac{8}{3} \left(\frac{KT}{2\pi m} \right)^{1/2} \frac{t_0 A^3}{l} \quad (27)$$

where t_0 is the sum of the blade separation t and thickness on the cross-section of the blade; i.e.

$$t_0 = t + \frac{d}{\sin \theta}$$

Let the angle of inclination of the blade be $\theta = 20^\circ$, the blade length $l = 20$ mm, the leak gap $d = 0.5$ mm, impeller separation $h = 2$ mm, the blade width $b = 10$ mm, and the thickness of the blade be neglected. The distribution of compression ratio along the length of the blade obtained based on equations (17) and (24) is shown in Figure 5. Curves 1 and 2 represent the middle and edge turbines, respectively. The dotted lines on the top and bottom represent the two special cases that $h = 0$ and $h = \infty$. From Figure 5 we can see that the compression ratio of the middle turbine is higher than that on the edge when the impeller separation is the same. Furthermore, the leak affected area is also smaller.

In the above discussion we did not discuss the mutual interaction between two neighboring leak gaps. In reality, the spacing between turbomolecular pump impellers is very small, usually less than 2 mm. Therefore, leak affected areas are mostly concentrated near the gap (see Figure 5). Leak affected areas of neighboring turbines almost do not overlap. Thus, their mutual interaction can be neglected.

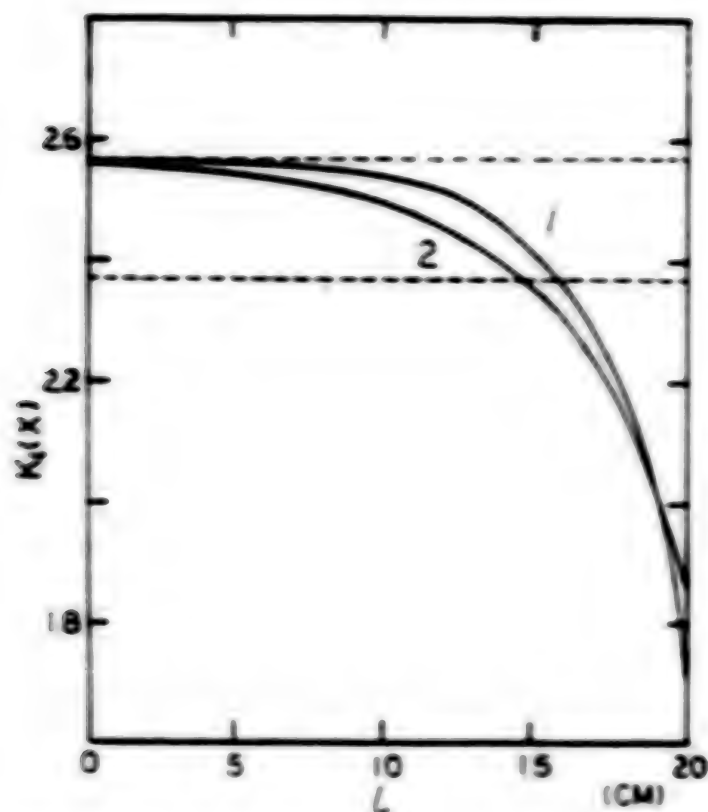


Figure 5. Compression Ratio vs. Blade Length

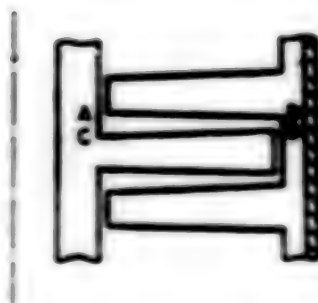


Figure 6. Axial Cross-section of a Practical Turbomolecular Pump Impeller

III. Correction for the "Dead Space" in the Gap

In addition to the leakage effect, the impeller gap also affects the relative velocity of the incident molecule relative to the impeller.

Figure 6 shows the axial cross-section of a practical impeller. h_1 and h_2 represent the inner and outer spacings of the impeller, respectively. For the moving impeller, incident molecules are composed of molecules scattered from surfaces AB, AC and BD. Among them, molecules scattered from AB and BD have a relative velocity. This means that the relative velocity of molecules scattered from AC with respect to the blade with a linear velocity v_b is zero. Furthermore, only one-half of the molecules scattered from AC and BD can incident upon the moving impeller. Therefore, the average relative velocity of incident molecules should be

$$v = \frac{2^{1/2} - 1}{2^{1/2} - 1 - h_1} v_{b1} \approx v_{b1} \quad (28)$$

where $\lambda = \frac{2^{1/2} - 1}{2^{1/2} - 1 - h_1} < 1$ is the correction factor.

From equation (28) we know that the presence of the gap lowers the relative velocity of the incident molecule. For the fixed impeller, all we have to do is to exchange h_1 and h_2 in equation (28).

This correction term is required because of the loss of relative velocity of the molecule scattered from AC. Therefore, we call it the "dead space" correction. This "dead space" on the inside of the moving impeller is particularly large when the blade is made by a twisting technique, which makes this correction term very important.

IV. Overall Correction for the Compression Ratio of a Turbomolecular Pump

According to the above discussion, it is concluded that the correction of the compression ratio of a combination turbomolecular pump should also include leak correction and "dead space" correction, in addition to the finite blade length correction. Every correction term has been derived. The question remained is the sequence of correction. Based on the physical significance, it is more reasonable to perform corrections in the order of "dead space", finite blade length and leak correction. However, the computation work load is larger according to this sequence. In order to save time, the order we are taking is leak correction, finite blade length correction and "dead space" correction. The final result was verified experimentally.

V. Experimental Apparatus and Results

Figure 7 shows a diagram of the experimental apparatus. The experimental pump comprised of a 3-stage moving impeller and a 2-stage stationary impeller made of an aluminum alloy. The dimensions of the moving impeller are shown in

Figure 8. The blade parameters are: $\alpha=30^\circ$, $\frac{r}{D}=0.9$, $b=10\text{mm}$, $l=25\text{mm}$, $\delta=0.5\text{mm}$ and the impeller outer diameter $D=169\text{mm}$. The impeller separation is adjustable. The blade parameters of the fixed impeller are the same as those of the moving impeller.

In the experimental apparatus, a combination of a 2x-8 mechanical pump and a F-203 diffusion pump in series is used as the fore-pump. The bearing of the molecular pump was lubricated by a high temperature instrument oil which has lasted for approximately 100 hours in use.

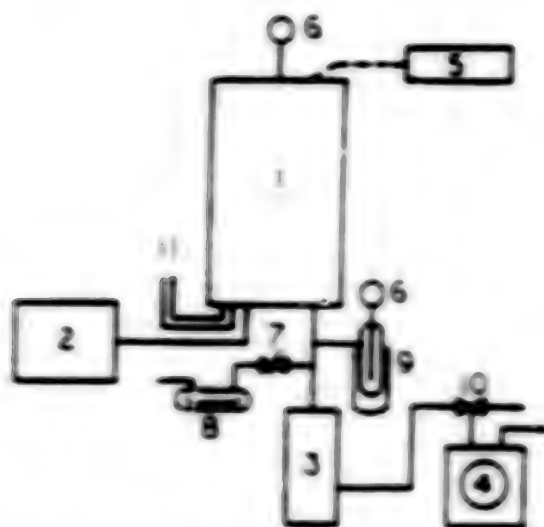


Figure 7. Experimental Apparatus

Key: 1 - molecular pump; 2 - medium frequency power supply; 3 - Model F-203 diffusion pump; 4 - Model 2x-8 mechanical pump; 5 - photo electric counter; 6 - ionization gauge; 7 - needle valve; 8 - desiccator; 9 - cold trap; 10 - air release valve; 11 - cooling water pipe.

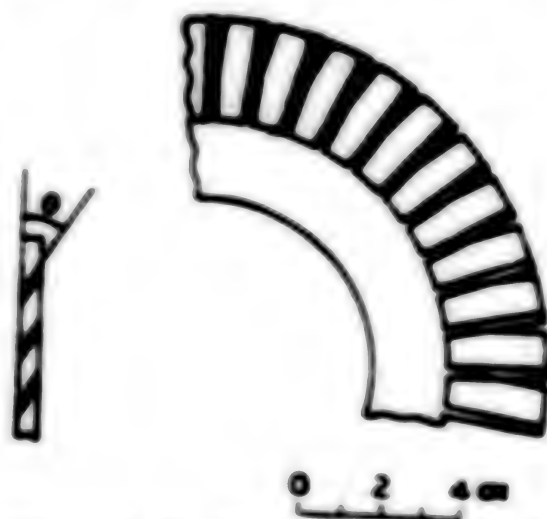


Figure 8. Cross-section of the Experimental Impeller

The vacuum system is sealed by vacuum rubber o rings. The pressure on either the inlet side and the exhaust side of the impeller was measured by ionization gauges. The relative error of the two vacuum gauges, including calibrating the amplifiers, is less than 5 percent.

In the experiment, the compression ratio was measured according to the "rising pressure method" specified by the International Organization of Standardization. The gas to be measured is dry air. In order to ascertain that the impeller is operational under molecular conditions, the primary pressure was always less than 1×10^{-3} torr. It was discovered that the use of a liquid nitrogen trap for the primary vacuum gauge had no effect on the experimental results. For this reason, all experimental data reported was obtained without the cold trap. The impeller separations are 1, 2 and 3 mm. The impeller rotating speed is 2,400 rev/min. The relative specific velocity is $z = 0.446$.

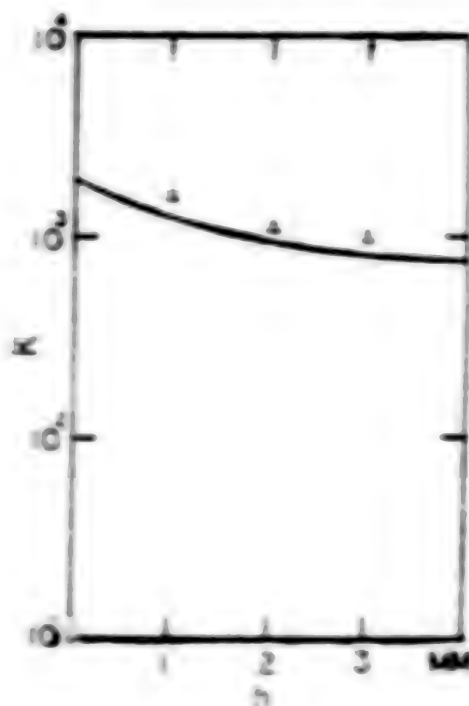


Figure 9. Compression Ratio vs. Impeller Separation h .

The experimental results are shown in Figure 9. The curve is the theoretical value after a comprehensive correction, which agrees well with the experimental data. The relative error is less than 10 percent which is within experimental error. Figure 9 also shows that the relation between compression ratio and impeller separation is not as close as predicted by Becker.

VI. Conclusions

The leak caused by the gap in a turbomolecular pump lowers its compression ratio. The effect of this leak on the middle impeller is less than that on a

side or single stage turbine. Both corrected and measured compression ratio values show that the relation between compression ratio and impeller separation is not very close. The current turbomolecular pump has a 3 mm operating gap, which is reasonable. To further reduce the operating gap will increase the technical difficulty. The compression ratio, however, cannot be significantly raised.

This work was completed under the direction of Professor Hua Zhongyi [6-28 0022 0001]. The machine shop of Zhejiang University provided all the experimental apparatus and testing equipment. The experimental work was jointly completed by the comrades of molecular pump development group of the machine shop of Zhejiang University. Among them, comrades Lu Shouyi [1778 1341 5088], Wang Fujin [3769 4395 3773] and Zheng Jiangting [6774 1886 7230] participated in all the experimental work. Comrades Wang Demiao [1768 1795 1479] and Ren Gaoshao [0088 7559 3390] of Zhejiang offered many valuable suggestions and facilitated the experimental work. Comrade Jiang Shengyi [5637 1182 4189] of Fudan University also provided beneficial guidance to the experimental work.

REFERENCES

- [1] Ch.H.Kruger, A.B.Shapiro, 7th Nat. Symp. Vac. Technol., Trans. 2., (1967), 6
- [2] J.C.Chu, Z.Y.Bua, J. Vac. Sci. Technol., Vol. 10, No. 4 (1967) 1781
- [3] Chu Jiguo, Vacuum Science and Technology, Vol. 1, No. 1, (1981) 11
- [4] U.Becker, Vakuum Technik, Vol. 13 (1966) 211, 274
- [5] Ch.H.Kruger, Ph.D. Thesis, Massachusetts Institute of Technology, (1966)
- [6] Design Manual of Vacuum System, Vol. I, p.72, Defense Industry Publishing Co 1972 edition

12553

CSO: 4008/10-9

APPLIED SCIENCES

THEORETICAL CALCULATION OF PULSED ACTIVE-PASSIVE MODE-LOCKED SOLID STATE LASERS
(PART I)

Beijing WEI L. XIEBAO [ACTA PHYSICA SINICA] in Chinese Vol. 34 No. 5, May 85
pp 602-610

[Article by Zhu Chenghe [2612 2161 0735] of the Institute of Physics, Chinese
Academy of Sciences; manuscript received 10 April 1984]

[Text] Abstract: A theoretical model for pulsed active-passive mode-locked solid state lasers is presented. The characteristics of these lasers can be solved by computer simulation with this model.

1. Introduction

Passive mode-locked pulsed solid state lasers are widely used as a source for picosecond laser pulses, but these lasers are intrinsically unstable. A simple method for improving their stability is to add an active modulator in the cavity. Such active-passive mode-locked lasers are first reported¹ in 1974 and subsequently studied by a number of researchers.²⁻⁴ According to the reported experimental results, the stability and repeatability of these lasers are considerably better than the pure passive mode-locked lasers.

Although pulsed active-passive mode-locked solid state lasers have been in existence for 10 years, there has not been a theoretical model, to our knowledge, that explains the characteristics of this type of laser. Good theoretical models⁵⁻⁶ have been developed for pure active mode-locked lasers. Such model assumes the mode-locking take place in a uniform single mode field in the cavity and, after repeated passages through the modulator, a pulse is formed. The pulse continuously narrows and finally becomes a picosecond pulse. Without considering the pulse formation process, a steady state self-consistent solution in the cavity may be found directly.⁷

Two theoretical models have been advanced for pure passive mode-locked solid state lasers. One model is based on the statistical fluctuation.⁸⁻¹¹ In this model the mode-locked pulse sequence grows out of the initial noise fluctuation and the strongest pulse is selected from the pulse sequence. This model satisfactorily explains the fluctuation and instability of the laser but cannot determine the shape and width of the pulse. The other model is based on a

quasi-steady state analytic theory¹⁻³ which gives the shape and width of the pulse but fails to explain the fluctuation nature of the laser.

In order to explain the behavior of pulsed active-passive mode-locked solid state lasers, the two totally different theories above (one statistical and the other deterministic) must be combined. This is a difficult task and perhaps also the reason that no theoretical model is yet available to date.

It was pointed out by some authors¹⁻³ that a passive mode-locked laser can be treated with nonstatistical quasi-steady state analysis after the gain medium and the saturable absorber enter the saturation region. Based on this idea, Zhu Zhenhe von der Linde² treated the passive mode locking first with the fluctuating model and then, after the gain saturation, with the quasi-steady state analysis. In this paper, we carried this method further and propose a theoretical model for active-passive mode-locked solid state lasers.

11. Theory

This section describes the function of the active modulator and proposes a theoretical model. Figure 1 shows schematically an active-passive mode-locked laser consisting of the cavity, the amplifying medium, the saturable absorber, and the active modulator. For simplicity we shall consider an attenuative modulator. For an ideal modulator the amplitude transmission coefficient⁴ is given by

$$a(t) = \exp[-\theta \sin^2(2\pi f_m t)] \quad (1)$$

and the transmissivity of the modulator is

$$T_m(t) = \exp[-2\theta \sin^2(2\pi f_m t)] \quad (2)$$

where f_m is the modulation frequency and θ is the modulation depth.

As shown in Figure 1(a), the output mirror with a reflectivity R and the modulator may be viewed as a single unit having a periodic reflectivity:

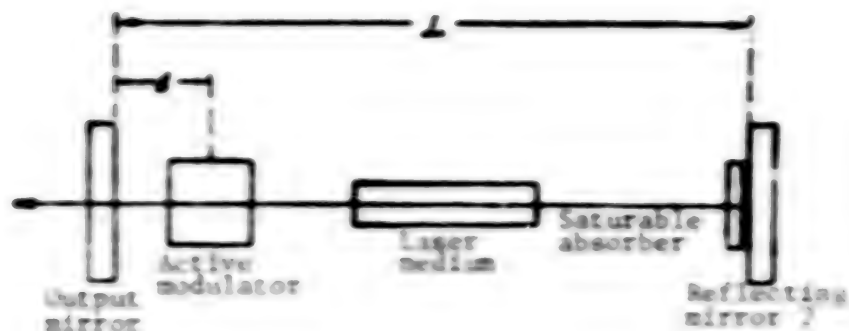
$$R_m(t) = T_m\left(1 - \frac{d}{c}\right) \cdot R \cdot T_m\left(1 + \frac{d}{c}\right) \quad (3)$$

where d is the distance between the modulator and the output mirror, and c is the speed of light. Substituting (2) into (3), we have

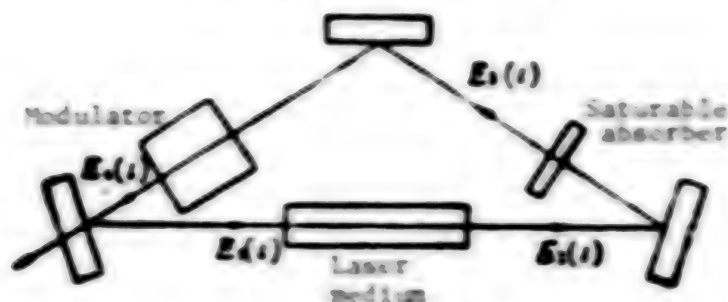
$$R_m(t) = R \cdot \exp\{-2\theta[1 - K \cos(4\pi f_m t)]\} \quad (4)$$

where the constant $K = \cos\left(4\pi f_m \cdot \frac{d}{c}\right)$.

If we view the Fabry-Perot cavity in terms of an equivalent ring cavity (see Figure 1(b)), then the transmissivity of the equivalent modulator is



(a) Fabry-Perot cavity



(b) Ring cavity

Figure 1. Schematic Diagram of a Pulsed Active-Passive Mode-Locked Solid State Laser

$$T_{\text{eq}}(t) = \exp\{-2\delta[1 - K \cos(4\pi f_m t)]\} \quad (5)$$

and the corresponding equivalent amplitude transmission coefficient is

$$a_{\text{eq}}(t) = \exp\{-\delta[1 - K \cos(4\pi f_m t)]\}. \quad (6)$$

Equation (5) shows that the frequency and phase of the equivalent modulator are the same as those of the actual modulator and only the waveform is slightly different. Figure 2 shows the transmission function of the equivalent modulator for $d = 0$ and $d = L/10$ (L is the cavity length) and a modulation depth of $2\delta = 0.25$. As can be seen, the difference in the modulation waveforms is very slight and the effect of d on mode-locking is expected to be small. Most of the calculations are therefore conducted for $d = 0$. For $d = 0$, Equations (5) and (6) can be simplified to (7) and (8), respectively;

$$T_{\text{eq}}(t) = \exp\{-4\delta \sin^2(2\pi f_m t)\} \quad (7)$$

$$a_{\text{eq}}(t) = \exp\{-2\delta \sin^2(2\pi f_m t)\}. \quad (8)$$

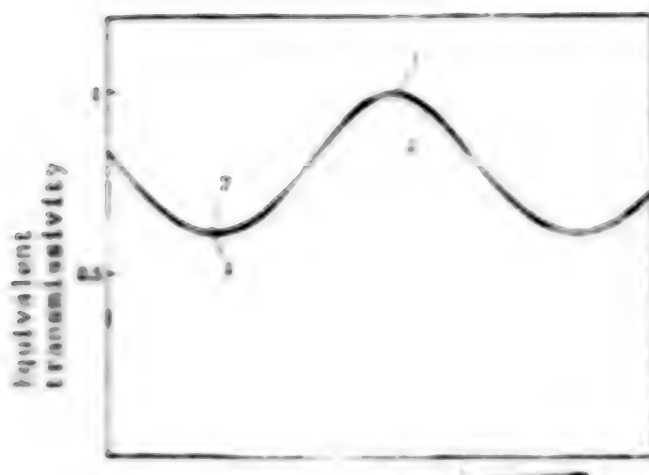


Figure 2. Transmission Function $T_{m,e}(t)$ of the Equivalent Modulator

Modulation depth $2d = 0.25$, curve 1 for $d = 0$ and curve 2 for $d = L/10$

We again make the assumption that, in an active-passive mode-locked laser, the pulse sequence originates from the initial noise fluctuation. We first consider the problem from the viewpoint of the fluctuation model in Reference 11. In this model, only the variation of the average light intensity is calculated for the initial phase. After the stimulated emission far exceeds the spontaneous emission, we assume an initial pulse group consisting of N pulses. The intensity distribution of the N pulses is logarithmic¹² and the magnitudes of the pulses appear in a random order. Now we add an active modulator in the cavity. $T_{m,e}(t)$ is equivalent to a "window" function and each round trip passage in the cavity is equivalent to one multiplication by the window function. When the stimulated emission far exceeds the spontaneous emission, the laser field has made thousands of passages in the cavity and, because of the window function, the order of the pulse magnitudes is no longer totally random. Obviously the probability for a large pulse to appear in the center of the window is greater and the intensity distribution of the pulses is no longer logarithmic.

For very small $2d$, the effects of active modulation is also small. For a given pulse sequence the intensity distribution does not deviate greatly from a logarithmic function and the order of the pulse magnitudes remains essentially random. Using widely different pulse distributions, we computed the intensity distribution for two limiting cases: (1) logarithmic function¹² of the noise distribution, and (2) logarithmic function multiplied by the N th power of the window function (7). Here N is the number of passages of the laser field in the cavity. We found that, as long as d is sufficiently small, all the calculated results are very close to each other.

As d increases, the behavior of pulse development gradually changes from random to deterministic and the calculated results for different pulse distribution begin to differ considerably. This shows that the positional

distribution of the pulses of different magnitude can no longer be considered random when the stimulated emission is much stronger than spontaneous emission. It is easy to imagine that, for large Γ , large pulses will occur at the center of the window and small pulses will appear at the edges of the window. We therefore choose a distribution when the pulse magnitude is greatest at the center of the window and the pulses gradually become smaller away from the center. The intensity distribution function of such a pulse distribution is difficult to calculate. Tentatively we take it to be a logarithmic function multiplied by the N th power of the window function, (7) or (5). Naturally the half-width of such a distribution will be somewhat smaller than the actual half-width. When Γ is sufficiently large and the half-width of the N th power of the window function is much smaller than the half-width of the logarithmic function of the noise distribution, it may be shown that the calculated results obtained by modifying the fluctuation model and taking the position and intensity distribution above are the same as that obtained by using the pure active mode-locking model. (After such modification the fluctuating model has in fact lost its statistical meaning.) In the pure active mode-locking model the laser field begins with a uniform single mode field in the cavity and makes many passages in the cavity. In each passage the laser field must go through the active modulator, the amplification medium, and the saturable absorber.

Based on the discussion above, we propose the following model. In the early stage of mode-locking, we use the "modified fluctuation model" and calculate only the variation of the average light intensity. When the stimulated emission far exceeds the spontaneous emission, we choose a collection of N pulses and take the intensity distribution of the pulses to be the logarithmic function of the noise distribution multiplied by the N th power of the window function given in (7) or (5). N is the number of passages already made by the laser field in the cavity. The sizes of the pulses are the largest at the center of the window and gradually decrease to the two sides. Calculations are then made using the equation given in Reference 11 with an additional active modulation term. After gain saturation is reached, calculations are made using the quasi-steady state analytic theory.

Although it is difficult to assess how well the model describes the behavior of the pulsed active-passive mode-locked solid state laser, the discussion above has shown that the model correctly describe the two limiting cases: (1) When Γ approaches zero, the model approaches the theoretical model¹¹ for a pure passive mode-locked laser; (2) when Γ becomes extremely large and the effect of the saturable absorber becomes correspondingly small, the model approaches the theoretical model¹¹ for a pure active mode-locked laser. We therefore conducted computations for the general case using this model and compared the results with experiments.

III. Analytic Model

We examine the behavior of a laser pulse that propagates one cycle in the ring cavity shown in Figure 1(b).

1. Pulse Parameters

We assume the electric field of the laser pulse to be of the following form:

$$E(t) = E(t) e^{-i\omega_0 t} \quad (9)$$

where $E(t)$ is the complex amplitude, and ω_0 is the center frequency. For simplicity, the amplitude is normalized so that the pulse intensity (power intensity) is given by

$$I(t) = |E(t)|^2. \quad (10)$$

$E_1(t)$ is the pulse entering the amplification medium, the peak value of the pulse occurs at $t = 0$ and $E_1(f)$ is the Fourier transform of $E_1(t)$.

2. Amplification Medium

It can be shown that the amplitude gain⁸ of a uniformly broadening laser is

$$g(f) = \exp \left[\frac{g_0}{1 + (2(f - f_0)/\Delta f_a)^2} \right] \quad (11)$$

where g_0 is the saturated amplitude gain at the center of the line (f_0) and Δf_a is the atomic linewidth.

If $E_2(t)$ is the pulse emerging from the gain medium, its Fourier transform is

$$E_2(f) = g(f) \cdot E_1(f), \quad (12)$$

3. Saturable Absorber

Using the four-level system shown in Figure 3 in describing the absorption characteristics ($\gamma_{21} = 0$, $\gamma_{10} = 0$) of the saturable absorber, we deduced an expression for the absorption coefficient^{10,13}:

$$\alpha(f) = \exp \left[-\frac{1}{\tau} \int_0^\tau \left(1 + \frac{I(f)}{I_s} \right) dt' \right] \cdot \left\{ 1 + \frac{1}{\tau} \int_0^\tau \exp \left[\frac{1}{\tau} \int_0^\tau \left(1 + \frac{I(f)}{I_s} \right) dt' \right] dt' \right\} \quad (13)$$

where k_0 is the unbleached absorption coefficient, I_s is the saturation intensity, τ (i.e., τ_{10}) is the relaxation time of the saturable absorber.

For the special case of fast relaxation ($\tau \rightarrow 0$), (13) may be simplified to^{10,13}

$$\alpha(f) = \frac{k_0}{1 + (I(f)/I_s)}. \quad (14)$$



Figure 1. Four-level Energy Diagram of the Saturable Absorber

The amplitude transmission coefficient through the saturable absorber is

$$T_a(t) = \exp\left[-\frac{1}{2} a(t)\right]. \quad (15)$$

Clearly the pulse after passing through the absorber is

$$E_s(t) = T_a(t) \cdot E_i(t). \quad (16)$$

The pulse intensity $I(t)$ appearing in Equations (13) and (14) is

$$I(t) = b |E_s(t)|^2 \quad (17)$$

where b is the beam cross section in the gain medium and the saturable absorber.

4. Active Modulator

The amplitude transmission coefficient $a_{eff}(t)$ of the laser pulse passing through the modulator is given by Equations (8) or (6). Since the laser pulse suffers a certain time delay (let the time delay of the pulse envelope be B) in passing through the gain medium and the saturable absorber,¹¹ the peak of the pulsers is no longer at $t = 0$ but at $t = B$ when the pulse goes through the modulator. The pulse coming out of the modulator is therefore

$$E_s(t) = a_{eff}(t - B) \cdot E_i(t). \quad (18)$$

An analytic expression for B cannot be deduced easily but its value may be obtained by simulation calculation.

The ideal modulation frequency, that is, the modulation frequency in the absence of detune, is

$$f_m = \frac{1}{2} \left[1 / \left(\frac{2L}{c} + \delta \right) \right] \quad (19)$$

where L is the optical length of the cavity. This frequency is different from the detune-free modulation frequency³ of an active mode-locked laser

$$f_m = \frac{1}{2} \left[1 / \left(\frac{2L}{c} + \frac{L}{\Delta L} \right) \right]. \quad (20)$$

In considering the effect of the detune error in the modulator, the detune is defined as the frequency shift from the ideal modulation frequency:

$$\Delta f_m = f_m - f_{m0} \quad (21)$$

This definition is consistent with the one given by Harris and McDuff.¹¹ When $f_m > f_{m0}$, the shift is negative, and when $f_m < f_{m0}$, the shift is positive.

5. Completing the Ring

Finally, we take into account the time delay $\tau_r = 2L/c$ incurred in completing the ring and introduce an effective loss coefficient γ , and obtain the pulse after one cycle:

$$E(t) = \exp\left(-\frac{1}{2} \gamma \tau\right) \cdot E(t - T). \quad (22)$$

Here γ includes the output loss of the output mirror and all the loss in the cavity.

6. Change in Gain Coefficient

The equation satisfied by the gain coefficient g ($g = 2g_2$) may be derived from the rate equation¹² of the four-level laser. In the saturation region the equation is simplified to

$$\frac{dg}{dt} = -\frac{2\sigma_s}{h\nu} I \quad (23)$$

where σ_s is the cross-section for stimulated emission and $h\nu$ is the photon energy.

Let the light intensity and the corresponding gain in the cavity on the k th passage be I_k and g_k , respectively, then it is easy to show that

$$g_{k+1} = g_k - g_k \cdot \frac{2\sigma_s}{h\nu} \cdot W_k \quad (24)$$

where W_k is the pulse energy in the cavity, given by the following equation

$$W_k = \int_{t_1}^{t_2} I_k(t) dt. \quad (25)$$

IV. Modified Fluctuation Model

The calculation steps and the meaning of the symbols in the various equations are given in detail in Reference 11 and will not be repeated here. We now describe the modification of the model.

Based on Section II, the relative intensity of the pulses in the initial group of pulses is as follows

$$\frac{I_s}{I_1} = \frac{\exp\left[-N \cdot 4\theta \sin^2\left(\pi \cdot \frac{s-1}{2M}\right)\right]}{\ln s} \quad (s = 1, 4, \dots, M) \quad (26)$$

$$\frac{I_2}{I_1} = C(M, P), \quad (27)$$

Here $C(MP)$ is a constant^{11,12} determined by the number of pulses M and the probability P . The definition of S is already given in Section II.

Equation (14) in Reference 11 is then modified to be

$$I_{i+1} = I_{i1} + I_{i2} \left[a_i - \tau - \frac{a_i}{1 + H_{i1}} - 4\theta \sin^2\left(\pi \cdot \frac{i-1}{2M}\right) \right] \quad (i = 1, 2, \dots, M), \quad (28)$$

Equations (26) and (28) are valid only when the modulator has no frequency shift error. In the presence of a frequency detune error, a pulse may pass through the modulator at the center of the window in a certain passage, but, as the pulse circulates in the cavity repeatedly, the time at which the pulse passes through the modulator gradually deviates from the center of the window. We therefore modify Equations (26) and (28) as follows

$$\frac{I_s}{I_1} = \frac{\prod_{k=1}^s \exp\left[-4\theta \sin^2\left[\pi \cdot \frac{(s-1) + \frac{\Delta f_0}{f_0} \left(i - \frac{N}{2} - \frac{1}{2}\right)}{2M}\right]\right]}{\ln s} \quad (s = 1, 4, \dots, M) \quad (29)$$

$$I_{i+1} = I_{i1} + I_{i2} \left[a_i - \tau - \frac{a_i}{1 + H_{i1}} - 4\theta \sin^2\left[\pi \cdot \frac{(i-1) + \frac{\Delta f_0}{f_0} (i-1)}{2M}\right] \right] \quad (i = 1, 2, \dots, M), \quad (30)$$

when $\Delta f_0 = 0$, (29) reduces to (26) and (30) reduces to (28).

By combining Sections III and IV, we have a complete theoretical model. Analytic solutions are extremely hard to obtain but computer simulations may be used instead. In the companion article, we present the computer simulation results. The theory and the experiment are in good qualitative agreement, suggesting that our model is a reasonable one.¹¹

REFERENCES

1. B.C. Johnson and W.D. Fountain, TECH. DIGEST, Int. Electron. Devices Meeting, (1974), p 322.
2. S. Kishida and T. Yamane, OPT COMMUN., 18(1976), 19.
3. W. Seka and J. Bunkenburg, J. APPL. PHYS., 49(1978), 2277.
4. M.A. Lewis and J.T. Kundraon, APPL. OPT., 21(1982), 2897.
5. H.P. Korts, IEEE J. QUANTUM ELECTRON., QE-19(1983), 578.
6. D.J. Kuizenga and A.E. Siegman, IEEE J. QUANTUM ELECTRON., QE-6(1970), 696.
7. Ibid., 709.
8. D.J. Kuizenga, D.W. Phillion, T. Lund and A.E. Siegman, OPT COMMUN., 9(1973), 221.
9. V.S. Letokhov, ZhETF, 55(1968), 1077; ERRATUM ZHETF, 56 (1969), 414; P.G. Kiryukov, V.S. Letokhov, IEEE J. QUANTUM ELECTRON., QE-8 (1972), 766.
10. W.H. Glenn, IEEE J. QUANTUM ELECTRON., QE-11 (1975), 8.
11. Zhu Zhenhe and Huo Chongru [7202 1504 0320], WULI XUEBAO [ACTA PHYSICA SINICA], 30, 178 (1981).
12. Zhu Zhenhe, WULI XUEBAO, 34, 426 (1985).
13. E.M. Carmire and A. Yariv, IEEE J. QUANTUM ELECTRON., QE-3 (1967), 222.
14. H.A. Haus, J. APPL. PHYS., 46(1975), 3049.
15. C.P. Ausschnitt, IEEE J. QUANTUM ELECTRON., QE-13(1977), 321.
16. J.A. Fleck, PHYS. REV., B1 (1970), 84.
17. Zhenhe Zhu and D. von der Linde, to be published.
18. M. Hercher, APPL. OPT., 6(1967), 947.
19. S.E. Harris and O.P. McDuff, J. QUANTUM ELECTRON., QE-1 (1965), 245.
20. A. Yariv, QUANTUM ELECTRONICS, 2nd ed., New York, Wiley, (1975).
21. Zhu Zhenhe, companion article in this issue.

9698

CSO: 4008/389

APPLIED SCIENCES

THEORETICAL CALCULATION OF PULSED ACTIVE-PASSIVE MODE-LOCKED SOLID STATE LASERS
(PART II)

Beijing WULI XUEBAO [ACTA PHYSICA SINICA] in Chinese Vol 34 No 5, May 85
pp 610-621

[Text] Abstract: Computer simulations are carried out using the theoretical model presented in the previous paper for pulsed active-passive mode-locked Nd-glass and Nd:YAG lasers. The dependences of some characteristics of active-passive mode-locked lasers, such as mode-locking threshold, output stability, pulse width, and pulse asymmetry, on the modulation depth and detuning of the active modulator and the relaxation time and concentration of the saturable dye are obtained in the simulations. The theoretical results are in good qualitative agreement with the experiments. The simulations explained some of the experimental observations and provided further understanding of the physical processes involved in active-passive mode-locking.

I. Computer Simulation

We have conducted computer simulation for pulsed active-passive mode-locked solid state lasers using the theoretical model presented in the previous paper.¹

1. Simulation Calculation Procedure

First we calculate the development of pulses and the increase of the gain for the pulse sequence using the modified fluctuation model.¹ When the gain g reaches its maximum value, the intensity and gain of the largest pulse are reached. Using the model described in Section III of the previous paper, the largest pulse is allowed to repeatedly pass through the laser cavity in the simulation and its evolution is followed. The maximum intensity and gain recorded earlier are used as the initial values in the simulation, and other pulses are treated as a background. Using Reference 2, the small signal solution is first obtained. In other words, we intentionally kept the pulse intensity at a low value. In this case, a steady state solution can always be found after the pulse makes a large number of circulations in the cavity no matter what its starting pulse shape is. The small signal solution is

used as the initial pulse $\{E_1(t)\}$ in the simulation and the justification is given in Reference 1.

The computer simulation requires repeated Fourier transforms and inverse Fourier transforms. Here we use the pulse envelop $E(t)$ for the time interval $(-T_0)/2 \leq t \leq T_0/2$ and substitute the function $E(t)$ with N discrete sampling values $E_n = E_n^* E(t_n)$, where $t_n = n\Delta t$; $n = -N/2 + 1, \dots, N/2$; and $\Delta t = T_0/N$. In the meantime the frequency spectrum $E(f = f_1)$ of the pulse is also replaced by the discrete spectrum $E_n = E_n^* E(f_n - f_1)$, where $f_n = f_1 + n\Delta f$; $n = -N/2 + 1, \dots, N/2$; and $f_1 = 1/T_0$. By doing so, we are able to use FFT (fast Fourier transform) for rapid transformation of the sampled E_n between the time domain and the frequency domain.

The protocol of the computer simulation is as follows. The initial pulse E_0 is stored numerically and, using the equations given in Section III of Reference 1, the signals after passing through each component are calculated until one cycle is completed. The signal after one cycle is again stored numerically. Using Equation (24) in Reference 1, the new gain is computed. Using the new gain we compute the new amplitude gain coefficient (Equation (11) in Reference 1). The process is then repeated for hundreds of times.

2. Aliasing

In the FFT calculation we assumed that the discrete sampling values are periodic in both the time domain and the frequency domain and therefore subject to the aliasing effect.^{1,2} In order to prevent aliasing, we multiplied the time domain signal $E(t_n)$ and the frequency domain signal $E(f_n)$ by a window function. We have tried several commonly used window functions^{3,4} and found that although they can suppress aliasing, they also distort the pulse shape.

Actually, the aliasing effect may be neglected as long as the time interval T_0 is much longer than the pulse width and the frequency bandwidth $N\Delta f$ is much greater than the bandwidth of the pulse. We used a T_0 equal to 10 times the pulse width and found that aliasing is negligible in most cases. Under certain circumstances, however, aliasing may be negligible in the first few cycles but gradually increases to such a degree that the simulation process must be aborted. Further investigations are needed to find an effective way for eliminating alias.

We need a T_0 equal to 10 times the pulse width instead of using a window function in our simulation. As a result we cannot calculate the parameters that would lead to an increase of aliasing. Fortunately, useful results can already be obtained within the parameter range we used.

Like in Reference 1, we also choose $N = 512$ in our calculation and the results are accurate enough.

3. Parameter Values

Table 1 shows the parameter values used in our calculation for Nd glass and Nd:YAG lasers.

Table 1.

Medium	α_0/ω (cm ⁻¹ /D)	α_0 (cm ⁻¹)	L (mm/cm)	θ	T_r (ns)
Nd glass	0.18	200	90	1	10
Nd:YAG	0.27	1	90	2	10

As explained in Reference 5, the beam cross-section ratio $b \sim 2$ is better than $b = 1$ for a Nd:YAG laser, we therefore take it to be 2. Depending on the experimental situation, the variable parameters are the loss coefficient γ , the absorption coefficient K of the saturable absorber, the relaxation time τ , the modulation depth z and the detuning $\Delta\omega_m$.

II. Calculation Results and Discussion

1. Mode-locking Threshold

The mode-locking threshold changes considerably when an active modulator is introduced to a passive mode-locked solid state laser. Figure 1 shows the dependence of the mode-locking threshold on the modulation depth of Nd glass and Nd:YAG lasers at different dye concentrations. In both cases the threshold decreased but by different amounts.

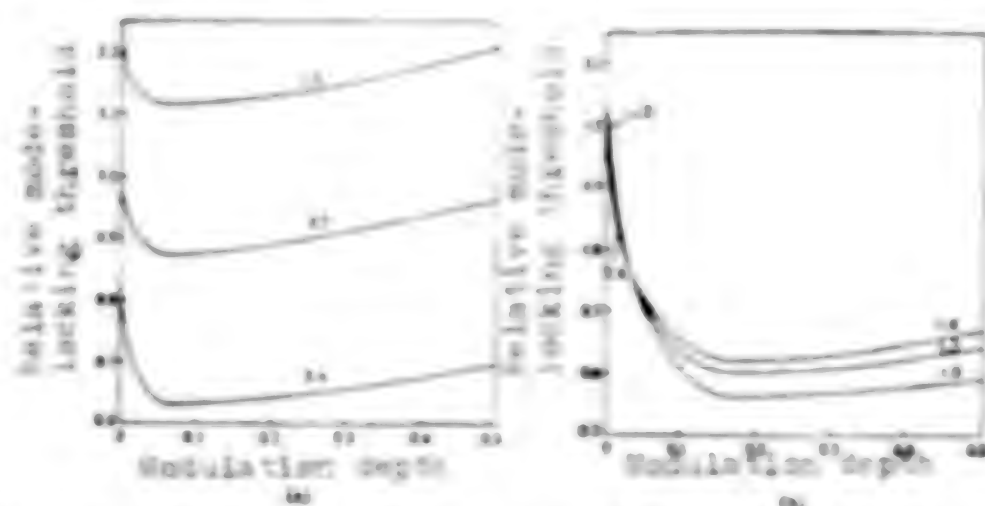


Figure 1. Mode-locking Threshold as a function of Modulation Depth (numbers in the curves are the K_1 values)

- (a) Nd glass, $\gamma = 0.18$, no detune, normalized to $K_1 = 0.7$ and $\tau = 0$
 (b) Nd:YAG, $\gamma = 0.27$, no detune, normalized to $K_1 = 1.0$ and $\tau = 0$

Under the action of the modulator, the laser field in the cavity soon changes from the initial random noise to become orderly and the largest pulse is quickly chosen, and, understandably, leading to a lower threshold. As the modulation depth increases, however, the total cavity loss also increases and the mode-locking threshold increases again after reaching a minimum. This phenomenon is evident in Figures 1(a) and 1(b).

Figure 1 also shows the effect of the dye concentration on the threshold. Within a certain range, the mode-locking threshold of a Nd glass active-passive mode-locked laser increases as the dye concentration increases. In a certain extent, the dye concentration does not affect the mode-locking threshold of a Nd:YAC active-passive mode-locked laser. In general, a Nd-YAC laser requires a higher dye concentration than the Nd glass laser.

Figure 2 shows the change of the threshold as a function of detune for different modulation depths. As expected, the threshold increases with detune. Also, the greater the modulation depth, the more the threshold increases with detune. This implies that the accuracy requirements on the modulation frequency and cavity length are greater at deeper modulation depth.

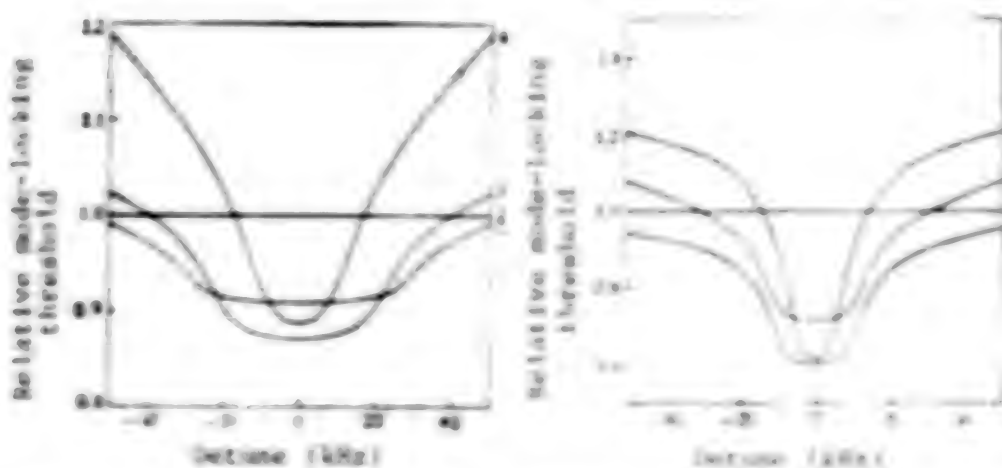


Figure 2. Mode-locking Threshold Versus Detune (ω/ω_0). All thresholds are normalized with respect to the threshold $\omega/\omega_0 = 0$.

- (a) Nd glass, $\gamma = 0.35$, $k_1 = 0.7$, 2β for curves 1, 2, 3 and 4 are, respectively, 0, 0.02, 0.06 and 0.2
 (b) Nd:YAC, $\gamma = 0.2$, $k_1 = 1.1$, 2β for curves 1, 2, 3 and 4 are, respectively, 0, 0.05, 0.13 and 0.2

Figure 3 shows a set of normalized $\text{SHER} \cdot \omega^2$ curves for Nd:YAC. (SHER stands for Second Harmonic Enhancement Ratio, and ω^2 is the mode-locking superthreshold.) As can be seen, the mode-locking threshold becomes extremely sharp with active modulation, a unique feature of the active-passive mode-locked laser. At a high dye concentration, the passive mode-locking threshold is already very sharp, the addition of the modulator makes it even sharper, but not as sharp as that shown in Figure 3. The threshold of an active-passive

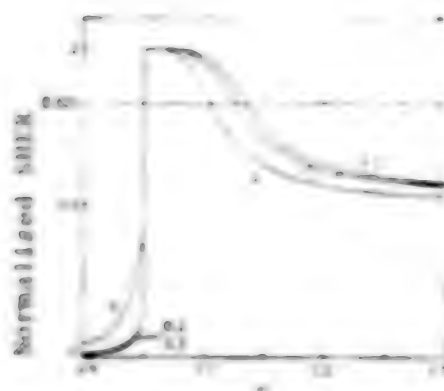


Figure 3. Normalized SHR Versus Δf Curves of a Nd:YAG Laser Under Peak Output. Values of $2f$ are shown on the curves, $\gamma = 0.2$, $K_1 = 1.0$, and no detune

mode-locked Nd glass laser also sharpens, but not as much as that of the Nd:YAG laser. The corresponding curves of the Nd glass laser are not shown here.

2. Stability

Active-passive mode-locking is known to improve the stability of lasers, again confirmed in our calculations. Figure 3 shows that the mode-locking window widens with increasing modulation (also true for Nd glass lasers), indicating an increase in stability. In order to quantify the stability improvement, we calculated the percent changes in the output pulse strength when the pumping rate is changed by 3 percent. We call this percent change the output deviation.

Figure 4 shows the output deviation as a function of the modulation depth. Figure 5 shows the output deviation versus detuning. Figures 4 and 5 show that the output stability of an active-passive mode-locked laser improves with modulation depth and deteriorates with detuning.

In producing an active-passive mode-locked laser, one always strives for a lower threshold, a higher stability, and a lower sensitivity to modulation frequency and cavity length. Our modulator is not the greater the better, instead, there exists an optimum depth, the same is true for the dye concentration. These optimal values depend on the cavity loss, the beam cross-section ratio, the relaxation time, and other specific requirements. Generally speaking, the modulation depth for a Nd:YAG laser should be greater than that for a Nd glass laser and the dye concentration should also be greater. In addition, our calculations also showed that Nd:YAG lasers can achieve a higher output stability.

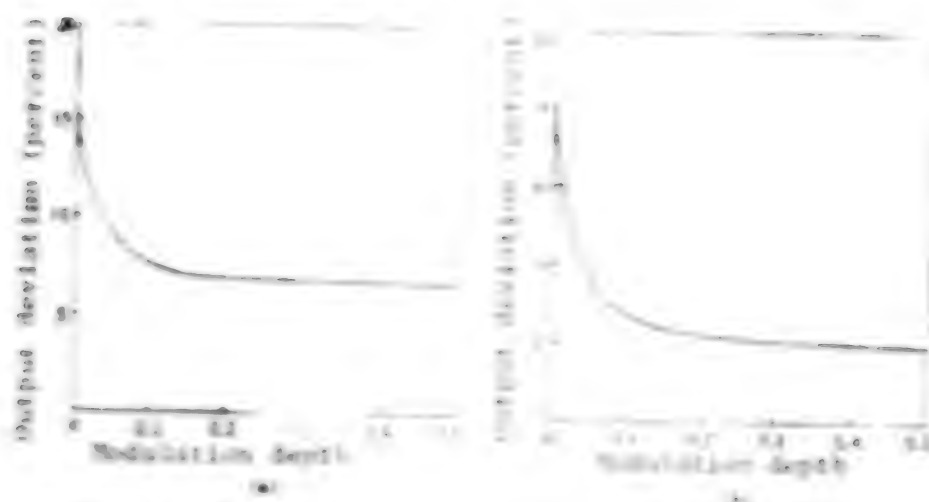


Figure 4. Output Deviation Versus Modulation Depth

- (a) Nd glass, $\beta = 0.01$, $k_1 = 0.1$, no detune
 (b) Nd:YAG, $\beta = 0.7$, $k_1 = 1.1$, no detune

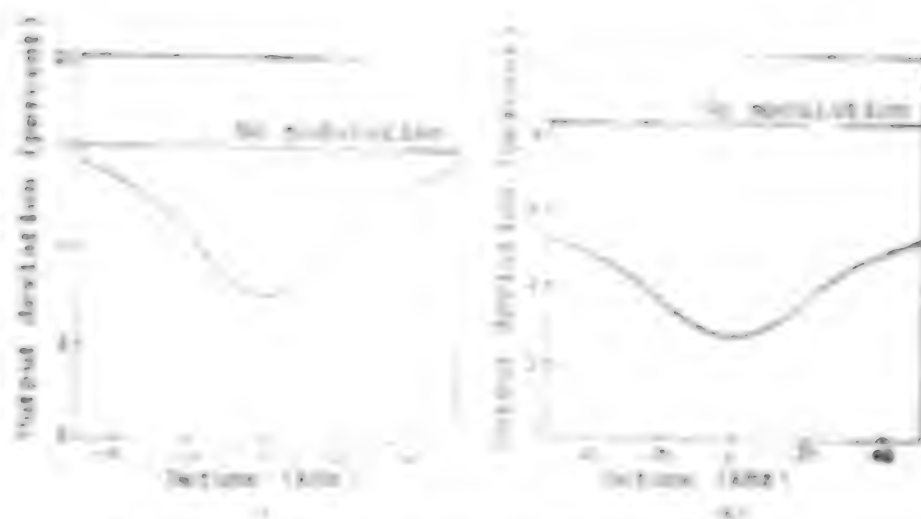


Figure 5. Output Deviation Versus Detune

- (a) Nd glass, $\beta = 0.01$, $k_1 = 0.1$, $D = 0.1$
 (b) Nd:YAG, $\beta = 0.7$, $k_1 = 1.1$, $D = 0.1$

3. Pulse Shape and Width

The pulse shape of an active-passive mode-locked laser is gaussian ($\exp(-\ln 2 \cdot t^2/t_p^2)$). Treating the dye as an inertialess saturable absorber, the small signal solution of a passive mode-locked laser is a hyperbolic secant: ($\text{sech}^2 = (0.44) \frac{t}{t_p}$). Calculations show that the small signal solution of an active-passive mode-locked laser (with inertialess dye) is still a hyperbolic secant. The situation is somewhat different for the Nd:YAG laser under certain conditions. The waveform of an active-passive mode-locked

laser is therefore determined primarily by the saturable dye and not so much by the modulator.

Since the relaxation time of the saturable dye is not infinitely small, the small signal solution is an asymmetric pulse with a slower rise and a faster drop.⁸ Such a pulse may be represented by the following empirical formula in Reference 2.

$$I(t) = \begin{cases} \exp \left[a_1 \left(\frac{t}{t_p} \right) + a_2 \left(\frac{t}{t_p} \right)^2 + a_3 \left(\frac{t}{t_p} \right)^3 \right] & (t \geq 0) \\ \exp \left[a_1' \left(\frac{t}{t_p} \right) + a_2' \left(\frac{t}{t_p} \right)^2 + a_3' \left(\frac{t}{t_p} \right)^3 \right] & (t < 0) \end{cases} \quad (1)$$

where $|a_1| = |a_1'| = a_1$ and $|a_2| = |a_2'| = a_2$. The values of a_1 , a_2 , a_3 , a_1' , a_2' , and a_3' depend on the laser parameters.

Our main interest is the true output pulse shape, that is, the pulse shape when the laser pulse intensity reaches a maximum in the cavity. For an inertless dye, the calculated pulse shape is basically Gaussian. For a Nd:YAG laser, the tail is lower than that of a Gaussian only when the modulation depth is large. But in actuality all dyes have a finite relaxation time and the computed waveform is asymmetric, as shown in Figure 6, with a steep-leading edge and a more gradual tail. Each a waveform may be represented by the empirical equation (1), but the signs of a_3 and a_3' are opposite to those of the small signal solution. For the discussion on the pulse width and asymmetry to follow, we introduce a quantity R_{as} known as the asymmetry factor. Figure 6 shows the definition of the pulse width τ_p and the asymmetry R_{as} .



Figure 6. A Typical Asymmetric Pulse and the Definition of the Pulse Width (τ_p) and the Asymmetry R_{as} .

In the simulation calculation we observed some interesting changes of the pulse shape in the cavity, see Figure 7. The pulse shape starts with a gradual leading edge and a steep tail and, just before the pulse intensity

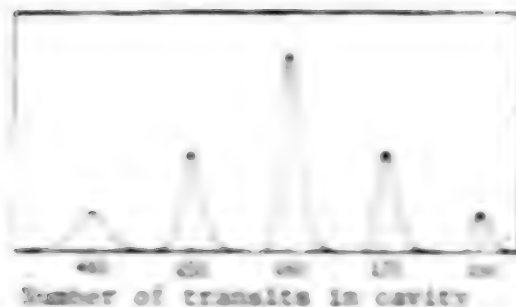


Figure 7. Changes of Pulse Shape in the Cavity of an Active-Passive Mode-locked Nd Glass Laser With a Finite Relaxation Time Saturable Absorber. On the 460th pass through the cavity, the pulse intensity reached a maximum. The pulse intensities are arbitrary.

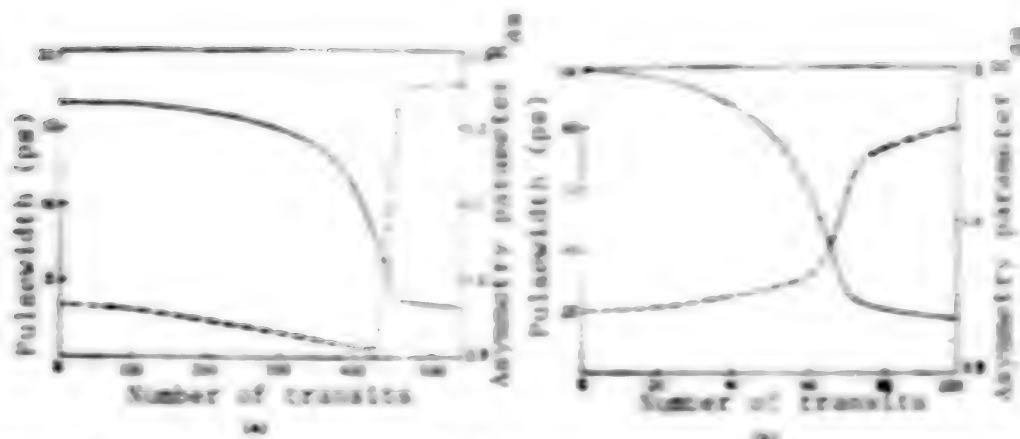


Figure 8. Pulse Width (solid line) and Asymmetry (dashed line) Changes. (Pulse intensity reaches a maximum on the N_{\max} passage.)

- (a) Nd glass laser, dye relaxation time $\tau = 10$ ps, modulation depth $2\delta = 0.06$, $N_{\max} = 460$
- (b) Nd:YAG laser, $\tau = 10$ ps, $2\delta = 0.1$, $N_{\max} = 76$

reaches its maximum, the asymmetry reverses and the leading edge becomes steeper. (The changes in Figure 7 are for a Nd glass laser but a Nd:YAG shows the same asymmetry reversal.) The cause of this phenomenon should be explained here. For a saturable absorber with a finite relaxation time, Equations (13) and (15) of Reference 1 should be used in the calculation of the amplitude transmission coefficient. This transmission function has two effects on the simulated pulse, one is to slow down the decay of the pulse tail and the other is to delay the pulse nonlinearly. The latter dominates when the pulse intensity is small and the result is a longer leading edge and a steep tail, like the first pulse in Figure 7. As the light intensity increases, the dye is gradually bleached and the first effect becomes more important, causing the asymmetry to reverse. At this time the nonlinearity of the dye causes rapid changes in the pulse width and the asymmetry, see Figure 8. As a result, the pulse shape

of the output pulse sequence changes. The early pulses have a gradual rise and a steep drop, the middle and late pulses have a steep rise and a gradual drop. The pulse widths are also different, the early pulses are wider than the late pulses.

In addition, the pulse delay caused by the saturable dye is nonlinear. Figure 9 shows the nonlinear increase of the delay as the number of passages increases. Figure 9 is based on a Nd:YAG laser, but the situation is similar for a Nd glass laser. Strictly speaking, the separation between two adjacent pulses is not a constant, although the difference is minute. For example, for a separation of 10 ns, the variation is no more than a few picoseconds, too small a change to detect experimentally.

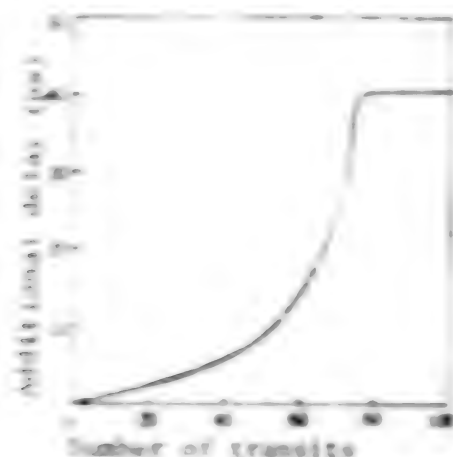


Figure 9. Pulse Delay Versus Number of Transits for an Active-Passive Mode-locked Nd:YAG Laser With a Finite Relaxation Time Saturable Absorber. The pulse intensity reaches a maximum on the 76th transit.

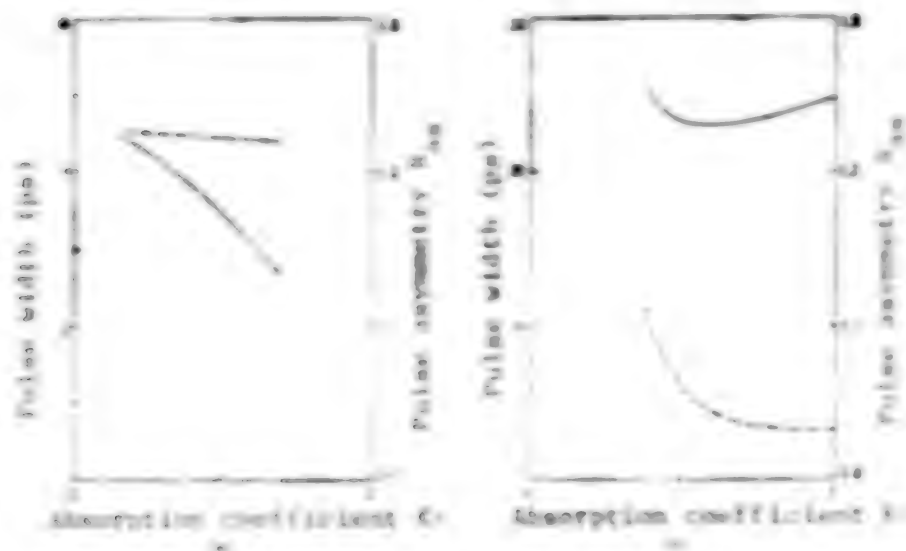


Figure 10. Pulse width (solid line) and Asymmetry (dashed line) Versus the Absorption Coefficient of the Saturable Dye

$\tau = 10$ ps, $\beta = 0.1$, no detune.

(a) Nd glass, $\gamma = 0.35$

(b) Nd:YAG, $\gamma = 0.1$



Figure 11. Pulse Width (solid line) and Asymmetry (dashed line) Versus Relaxation Time of the Saturable dye
 $2\tau = 0.1$, no detune

- (a) Nd glass, $\gamma = 0.35$, $\kappa_0 = 0.7$
- (b) Nd:YAG, $\gamma = 0.2$, $\kappa_0 = 1.1$

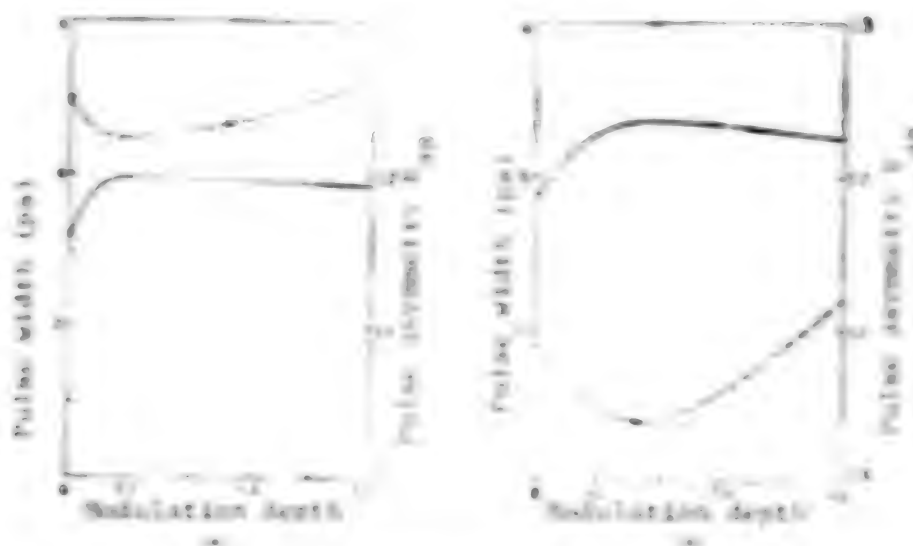


Figure 12. Pulse Width (solid line) and Asymmetry (dashed line) Versus Modulation Depth
 $\tau = 10$ ps, no detune

- (a) Nd glass, $\gamma = 0.35$, $\kappa_0 = 0.7$
- (b) Nd:YAG, $\gamma = 0.2$, $\kappa_0 = 1.1$

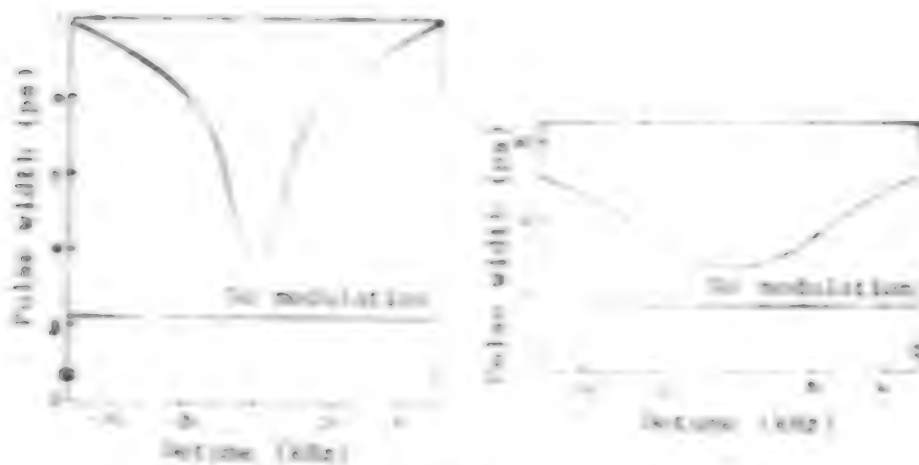


Figure 11. Pulse width as a function of detune
 $\tau = 10$ ps

- (a) Nd:glass, $\beta = 0.35$, $R_1 = 0.7$, $\beta' = 0.06$
 (b) Nd:YAG, $\beta = 0.2$, $R_1 = 1.1$, $\beta' = 0.13$

Figures 10 through 13 show the changes of the pulse width and the asymmetry versus the concentration and relaxation time of the saturable dye and the modulation depth and detune of the modulator. One observes that the relaxation time of the dye has the greatest effect on τ_p and R_{app} . The simulation results show that the saturable dye plays an important role in the pulse formation process and affects the pulse shape and width.

The following formula is often used in the calculation of the pulse width^(11,12):

$$\frac{1}{\tau_p^2} = \frac{1}{\tau_a^2} + \frac{1}{\tau_p^2} \quad (12)$$

where τ_{pa} is the pulse width of a purely active mode-locked laser, and τ_{pp} is the pulse width of a purely passive mode-locked laser. Based on this equation, the pulse width τ_p of an active-passive mode-locked laser should be less than τ_{pp} , but this contradicts with experimental results.⁽¹¹⁾ In our calculation, we found the increase in pulse width of an active-passive mode-locked laser, see Figure 12. The effect of the modulator should cause the width to narrow, so why does the width of the output pulse broaden? In analyzing our simulation process we found that introducing an active modulator lowers the mode-locking threshold and the initial values of the gain and the light intensity used in the calculation in Section 3 become smaller. As a result, the small signal solution pulse width increases and so does the output pulse width. If the initial values of the gain and the pulse parameters were intentionally set to the values for a pure passive mode locking, then the calculated results show a narrowing of the output pulse. Our computed pulse widths for a Nd:glass laser and a Nd:YAG laser are generally in good agreement with the experiment.

4. Distance Between the Modulator and the Output Mirror

In order to study the effect of the distance between the modulator and the output mirror, we carried out calculations while varying d (from zero to $1/10$ of the cavity length). Results show little changes of the threshold, stability, and pulse width, thus confirming the prediction in Reference 1 and conforming the experimental result in Reference 10.

III. Conclusion

We have proposed a theoretical model for a pulsed active-passive mode-locked solid state laser and conducted computer simulation for Nd:glass and Nd:YAG lasers. Calculated results confirmed experimental observed phenomena of a lowered mode-locking threshold, an improved stability, and an increased pulse width (lower than that of a purely passive mode-locked laser). The theoretical results are in good qualitative agreement with the experiment. Since simplifying assumptions were made in the model, it is unrealistic to expect quantitative agreement.

We have obtained the effects on mode-locking by parameters of the saturable dye and the modulator. These results will be important in the improvements of an active-passive mode-locked laser. Our model successfully described the physical process of active-passive mode-locking. With the addition of an active modulator, the pulse development changes from a random behavior to a deterministic behavior as the modulation depth increases. This is the essence of the improved stability.

Acknowledgement: This work is completed at the Essen University in the German Federal Republic. The author thanks the support provided by the German Federal Republic and the Humboldt Foundation and Professor D. von der Linde for his support. He also thanks Essen University for the use of the computer.

REFERENCES

1. Zhu Zhenhe, WULI XUEBAO [ACTA PHYSICA SINICA], this issue.
2. Zhu Zhenhe and D. von der Linde, to be published.
3. E.O. Brigham, "The Fast Fourier Transform," Englewood Cliffs, New Jersey, Prentice-Hall, (1974).
4. J.R. Rehner and B. Gold, "Theory and Application of Digital Signal Processing," Englewood Cliffs, New Jersey, Prentice-Hall, (1975).
5. P.H. Horton and R. Deor, J. OPT. SOC. AM., 66(1974), 738.
6. Zhu Zhenhe and Bao Chongru [7202 1504 0320], WULI XUEBAO, 30, 178(1981).
7. D.J. Kuizenga and A.E. Siegman, IEEE J. QUANTUM ELECTRON., QE-6 (1970), 644.

8. H.A. Haus, J. APPL. PHYS., 46(1975), 3049.
9. P.O. Hagelstein and C.P. Auschmitt, J. APPL. PHYS., 47(1976), 224.
10. H.P. Kottz, IEEE J. QUANTUM ELECTRON., QE-19(1983), 578.
11. C.P. Albrecht and J. Bunsenborg, OPT. COMMUN., 38(1981), 377.

9608

CSO: 4008/389

APPLIED SCIENCES

OPTICAL ADJUSTMENT FOR EOT2000 INFRARED RANGEFINDER DETAILED

Beijing CENVI TONGBAO [GEODESY AND PHOTOGRAPHY BULLETIN] in Chinese No 3,
25 Jun 85 pp 33-39

[Excerpt] In the article "A Study of the Four-Axes Problem of the EOT2000 Infrared Rangefinder" published in Vol 5 of CENVI TONGBAO, we made an initial study of the four axes relationship of EOT. In this paper we discuss the mechanism and the optical adjustment of the EOT.

The optical adjustment of the EOT differs from that of an ordinary theodolite and involves the adjustment of the optical paths of the four axes.

The EOT is a stand-alone apparatus and the disassembly and adjustment must be performed strictly according to a set procedure to insure the optimum operating condition of the apparatus. Here we describe the disassembly procedure for the infrared optics and their operating principles.

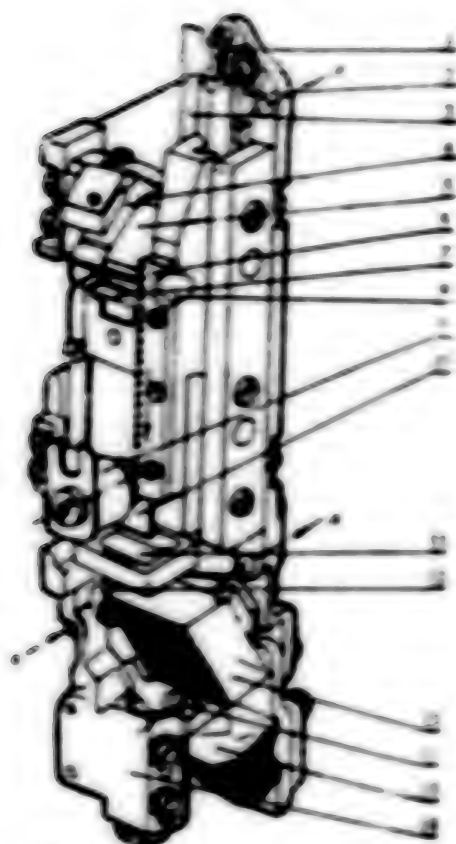


Figure 1. The Optical Micrometer

Key:

1. Balance spring for eliminating gravity effects
2. Micrometer travel stop
3. Glass plate
4. Field lens for reading window
5. Fitting prism
6. Micrometer rack
- 7,11. Double micrometer optical wedge assembly
8. Horizontal axis tilt calibration hole
9. Micrometer hand/wheel linkage
10. Optical path divider plate
12. Lens offset correction knob for H/V changeover prism (13)
14. Rotation axis of prism 11
15. Vertical image rotator prism
16. Objective assembly for horizontal reading microscope

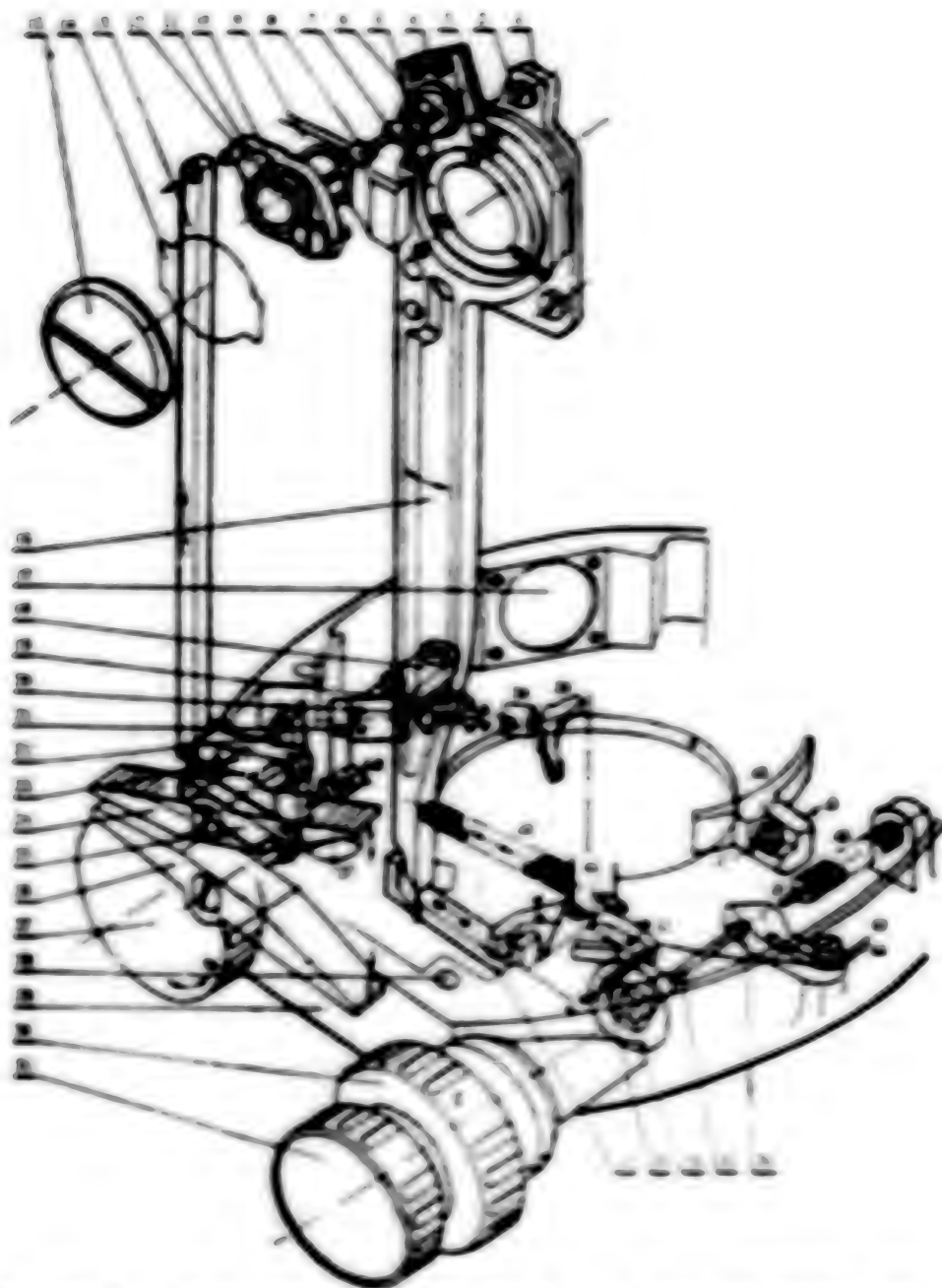


Figure 2. Structure and function of the logging Mechanism

Key:

1. Horizontal axis tilt correction plate
2. Three set screws of the correction plate
3. Four set screws of the vertical jogging arm
4. Horizontal clamping plates
6. Horizontal axis set screw with notch
7. Fixed plate with a conical surface and connected to the horizontal axis
- 8, 20. Universal joint
9. Axle frame
10. Vertical brake tightening adjustment screw, situated on the shoulder of part (11)
11. Axle with a notch and linked to the universal joint
21. Adjustment screw for setting the brake tension of the aiming mechanism. Adjustment is done through the opening (17)
22. Coupling linkage for horizontal brake

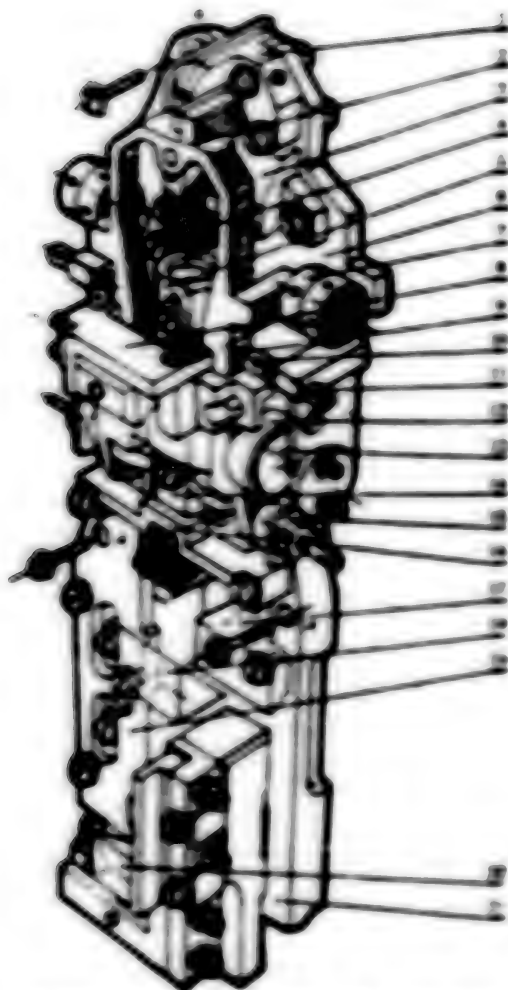


Figure 3. Large Optical Assembly in the Left Frame

Key:

1. Base for the automatic compensator
2. Pendulum
- 3, 17. Vertical plate illumination prism
4. Ridge prism for the 1:1 imaging system
- 5, 16. Objective assembly and base for the 1:1 imaging system
- 6, 21. Base for the large optical assembly
7. Weight
- 8, 20. Infrared reflector and base
9. Pendulum axis
- 10, 11. Pendulum amplitude limiter
- 12, 13. Cylinder, piston and piston adjuster for air damping
15. Pendulum coefficient adjustment plate
18. Horizontal dial illumination prism
19. Objective assembly for vertical plate microscope

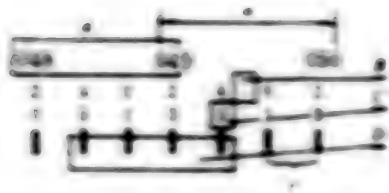


Figure 4. Graduation Method for the VOT Dial

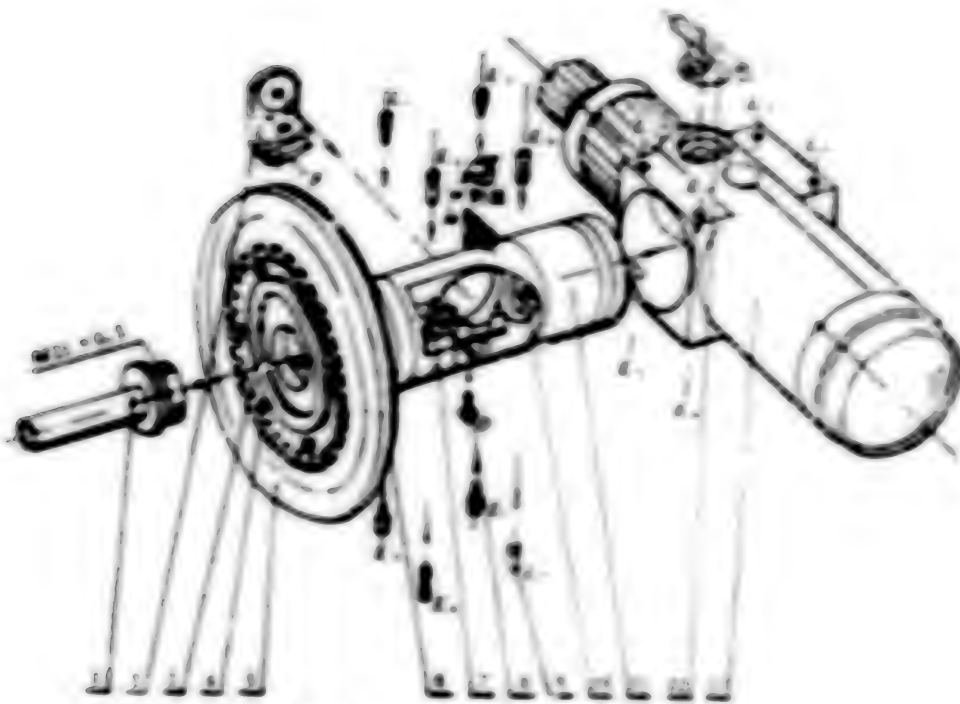


Figure 5. Horizontal Axis Structure

Key:

1. Special tool to disassemble the horizontal axis (M21 x 0.5)
2. Infrared reflection system
- 3, 4. Clamping plates and six set screws for the vertical disk
- 5, 6. Vertical dial and protective glass
7. Infrared reflection lenses and their base
8. Set screw for Part 2.
9. Eight set screws to fix the horizontal axis and adjustment limit screws
10. Reading microscope system rotates towards the prism base
11. Horizontal axis
12. Telescope body



Figure 6. Special Tool



Figure 7. Clamping Ring

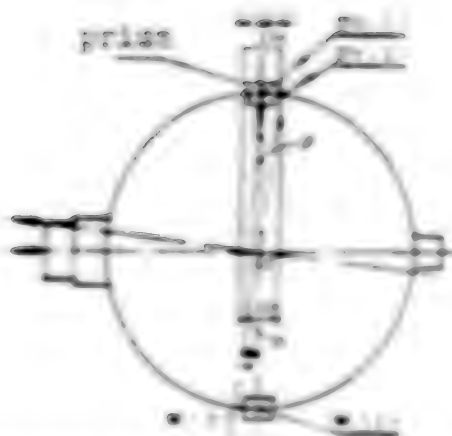


Figure 8. Principle of the Uncompressed Elastic Position

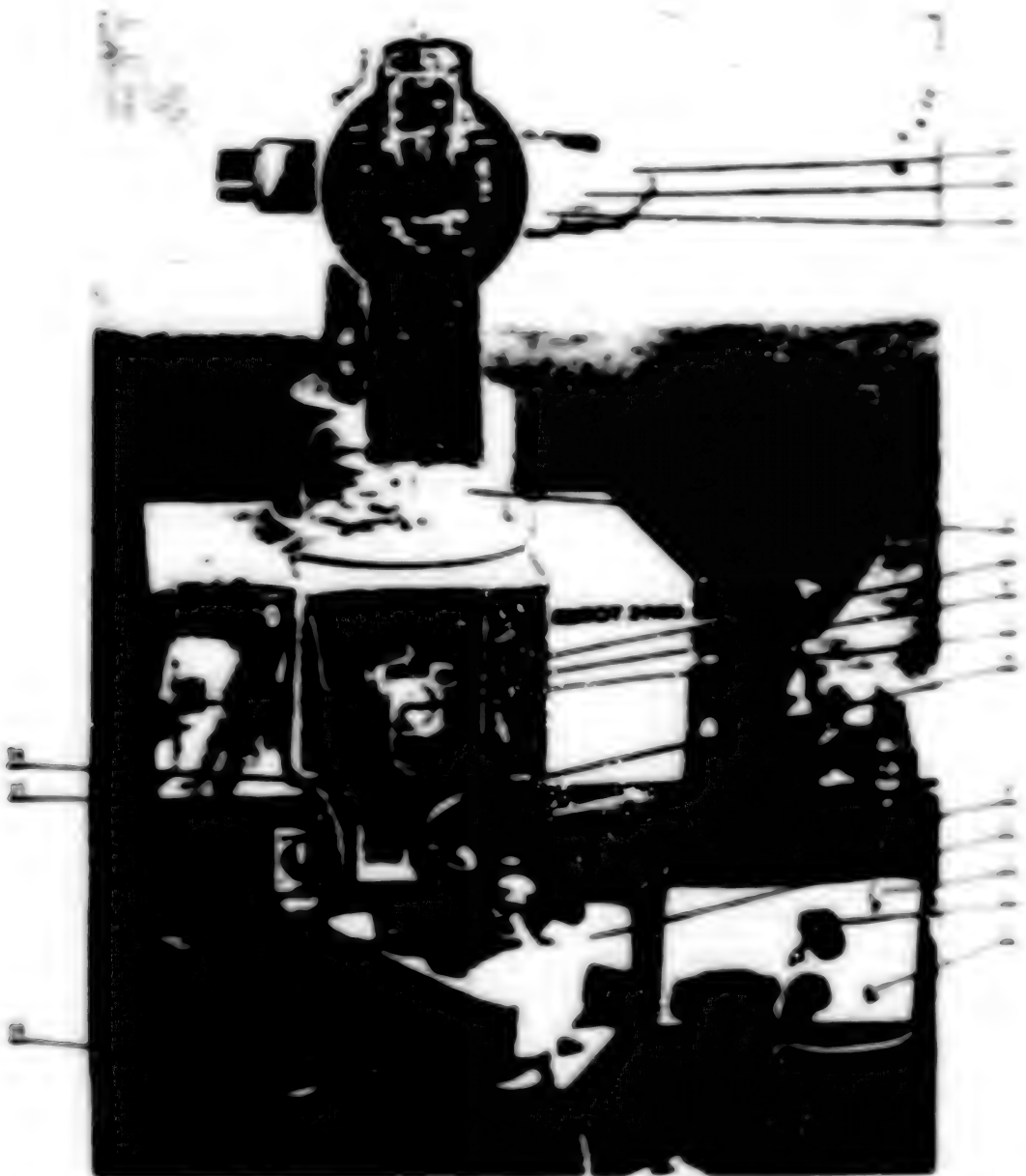
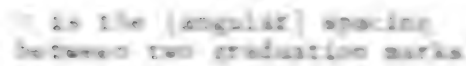


Figure 9. Photo Showing the Rotational and Vertical axes of the MPT being Adjusted

Key:

1. Single angle reflector
2. Prism cover
3. Telescope
4. Cleaning hole for the outer surface of the horizontal and prism
5. Set screw of the base (6) of the optical detector (14)
6. Small aperture grating
8. Adjustable spot light and lamp
9. 6V 2.5A step-down transformer
11. Power pilot light
12. Brightness adjustment knob and brightness pilot light
14. Electrical plug for optical detector (14)
15. Second corner of the MPT (14) arm



11-1

11-2

11-3

11-4

cross-section view

side view

Def:

-

1

APPLIED SCIENCES

CONFIGURATION AND LONGITUDINAL WIND TUNNEL TESTING OF FORWARD-SWEPT WING

Wanyang KONGJIDONGXUE KUBAO [ACTA AERODYNAMICA SINICA] in Chinese No. 1,
Jun 85 pp 61-68

[Article by Ye Weiliang [0673 3555 2733] and Xiao Benxi [3133 0036 339] of the Nanjing Aeronautical Institute. "Analysis of Aerodynamic Configurations of Forward-Swept Wings and Low-Speed Longitudinal Testing"]

[Text] Abstract:

Based on low-speed wind tunnel testing, calculation of load distribution and the transonic-supersonic area rule, this article analyzes the aerodynamic characteristics of aircraft with a configuration of forward-swept wings [FSW hereafter]. It suggests measures for improving the aerodynamic characteristics of FSW and uses the principle of symmetry to solve problems related to the application of the area eddy method and the area rule calculation method for FSW. The experimental research and calculations show that FSW have rather good aerodynamic characteristics and that a winglet at the wing tip can improve the lift and lift-drag ratios of FSW. FSW more closely approximate an optimum load distribution than do aft-swept wings (ASW hereafter). There are obvious improvements in airflow separation at the FSW base from using a nose-coupled canard and a fairing panel at the wing base. FSW more closely approximate an optimum load distribution than do ASW. The axial cross-sectional load distribution on an FSW with a canard more easily approximates an optimum load distribution and thereby can result in an obvious reduction in zero-lift wave drag.

1. Introduction

Aircraft with an FSW configuration now are in the flight trial and research stage. The American B-29 aircraft is a typical example. Although the use of the favorable external shape of FSW to overcome transonic drag divergence appeared at the same time as ASW, the problem of divergent static aerodynamic elasticity remained unsolved or in a state of stagnation for a long period. Developments in composite and active control technologies have provided a foundation for full utilization of the superiority of an FSW aerodynamic configuration. The rearward placement of the wing base provides flexibility for the overall configuration, while a matching canard makes the entire aircraft more closely suited to transonic-supersonic area rule laws and reduces zero-lift wave drag. Moreover, trim lift is high, drag is low and the angle of

angle of attack is large. This means that there is a large range for angle of attack.¹ Lifting and motion characteristics are good. Separation is made difficult at the wing base at an FPA and vibration operation characteristics are good. The load distribution along the direction of spread approximates an optimum load distribution under conditions of equal weight.² FPA have positive benefits for testing aerodynamic and structural phenomena.

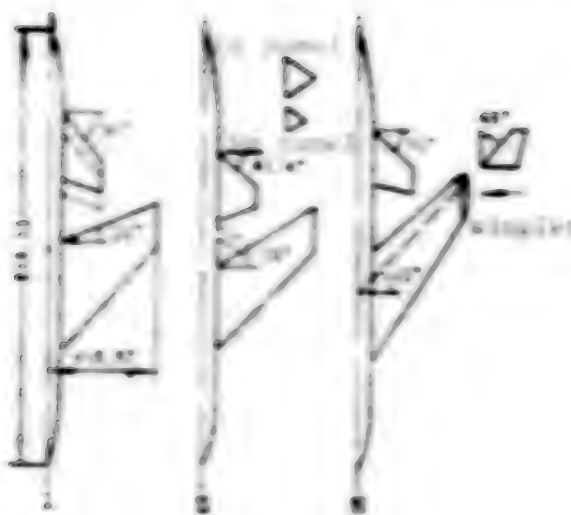
The low-speed wind tunnel testing in this article's study of FPA configuration aerodynamic characteristics included comparative tests of FPA and ASW wing units, manometric testing of FPA and longitudinal low-speed dynamic testing of FPA with fairings and fairing panels. We also used the Schwarz Method³ to calculate the load distribution of FPA and the Hinkle Transonic-Supersonic Area Rule Method⁴ to calculate the wave drag of FPA units. The calculations indicate that these two computational methods are suitable for FPA.

(1) Longitudinal Low-Speed Aerodynamic Characteristics

The experiments were done in a 1 meter (40 in) diameter low-speed wind tunnel. The wind speed was 25.47 m/sec and the Reynolds number $Re = 1.8 \times 10^5$. There were four models in the group. Figure 1 illustrates the internal shape of one-half the dynamically models. The external shape of the half of the manometric model was the same as model No. 1.

Figure 1

Internal Shape of Models



(2) Flow Field Analysis

Flow visualization and a camera were used to illustrate flow trends at the wing surface. FPA have different characteristics in the direction of the wing base in comparison with ASW, as shown in Figure 2 (not reproducible). During the air-flow separation at the wing surface with a low angle of incidence, developed flow lines formed vortices at the wing base and wing tip of the FPA, and the aerodynamic load distribution was concentrated at the base. When $\alpha = 8^\circ$, separation vortices at the front edge were more obvious. These separation vortices expanded gradually moving from the wing tip to wing base. The mix of the

eddies expands with the angle of incidence and they move toward the rear edge. Moreover, lateral flow increases the thickness of the boundary layer in the area of the wing base. When $\alpha = 17^\circ$, the air flow at the wing base is completely separated, but does not separate at the wing tip. There was incomplete separation at the wing tip of an ASW at this time.

Installation of a canard caused an obvious improvement in the flow field at the base of the FSW. This was especially true of a close-coupled canard. Photographs at different angles of incidence indicate that with the effective interference of canard body-eddy removal, there is almost no lateral flow on the main wing when $\alpha = 5^\circ$. Front-edge eddies at the main wing caused partial separation at the outer wing segment when $\alpha = 8^\circ$. Local separation occurs only in the middle section of the main wing when $\alpha = 17^\circ$. Without the canard, the region of separation is smaller and there is no separation at the wing base or tip. Installation of the canard at different angles is even more effective in improving the flow field of the main wing.

A fairing panel at the wing base of an FSW also effectively improves the flow field. A fairing panel at the wing base causes the air flow to flow laterally toward the outside and thereby stops boundary layer accumulation formed by lateral flow of the outer wing air flow toward the inside. In combination with effective interference of the canard, the region of local separation is reduced even more, as shown in Figure 1 (not reproduced).

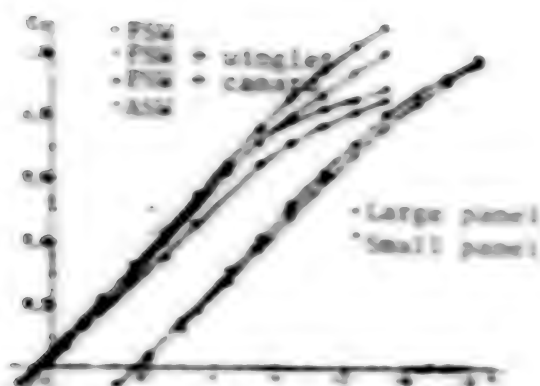
2. Dynamometric results

a) Lift characteristics. An FSW with a moderate or small angle of incidence has a linear lift curve. The separation eddy destruction at the front edge when the angle of incidence is large results in a declining slope in the lift line and the curve starts to bend. After addition of a canard, the effective interference of the body-eddy removal by the canard controlled air flow separation at the wing base and caused the linearity of the lift curve to improve. A slight curve in the lift curve appears only after the angle reaches 17° , as shown in Figure 4. The slope of the lift line of an FSW is greater than that of an ASW. The ability of eddy-body removal by a close-coupled canard to control air flow separation on the surface of the main wing is greater than that of a far-coupled canard. When the lift curve of a far-coupled canard starts to bend, the lift curve of a close-coupled canard still maintains an excellent linear relationship. For an FSW with a (fairing panel), a small fairing panel has better lift than a large panel. The small panel causes local improvements in air flow at the wing base, with the wing surface in the middle section of the main wing being subjected mainly to canard body-eddy removal. This results in rather good lift characteristics. A fairing panel that is too large causes stronger slip of the air flow from the wing base toward the outside, which is not good. Selection of the size of a fairing panel, therefore, deserves discussion. A winglet at the wing tip caused an obvious increase in lift of the FSW.

b) Lift-drag characteristics. FSW have less drag than ASW when the angles of incidence are identical. Because the lift of ASW is greater than FSW, however, the lift-drag ratio of ASW is greater than that of FSW within a range

Figure 4.

Lift Curves



of moderate angles of incidence. When there is a large angle of incidence, the more rapid air flow separation of ASW causes the lift-drag ratio to be nearly the same. Canards have obvious effects in improvement of the lift-drag ratio of FSW, while the results are smaller with ASW, as is shown in Figure 5. This is because of the greater frontwash effects of FSW compared with ASW. Moreover, the canard body-eddy removal improves the results of FSW wing surface flow fields rather well. When the angle of incidence reaches 17° , there still is no obvious air flow separation on the main wing, whereas rather large air flow separation regions begin to appear at the wing tip on ASW, causing a rapid increase in drag. Canard placement affects load-drag characteristics. Under moderate angles of incidence, the lift-drag ratio of close-coupled canards is greater than far-coupled canards. For FSW with fairing panels, the lift-drag ratio of small panels is better than that of large ones. When α is within a range of less than 10° , drag is reduced. The improvements in lift-drag ratios are shown in Table 1.

Figure 5.

Lift-Drag Ratio Curves

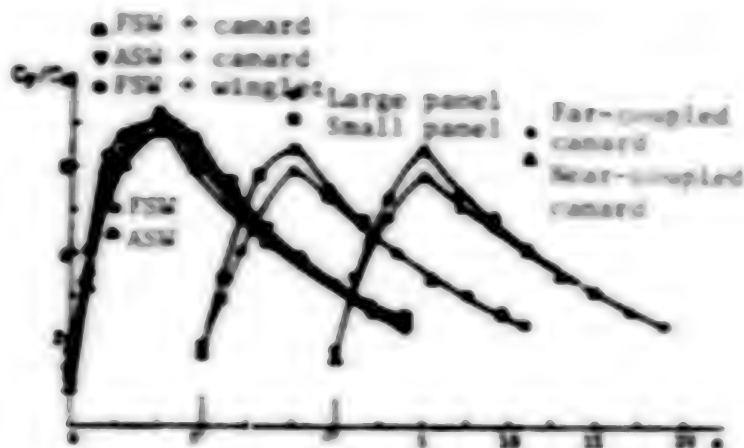


Table 1.

α (degrees)	1	2	3	4	7	9
% Decrease in drag	21.1	22.10	17.58	7.6	1.69	0.71
% Increase in lift-drag ratio	19.87	32.70	23.31	9.68	1.90	2.77

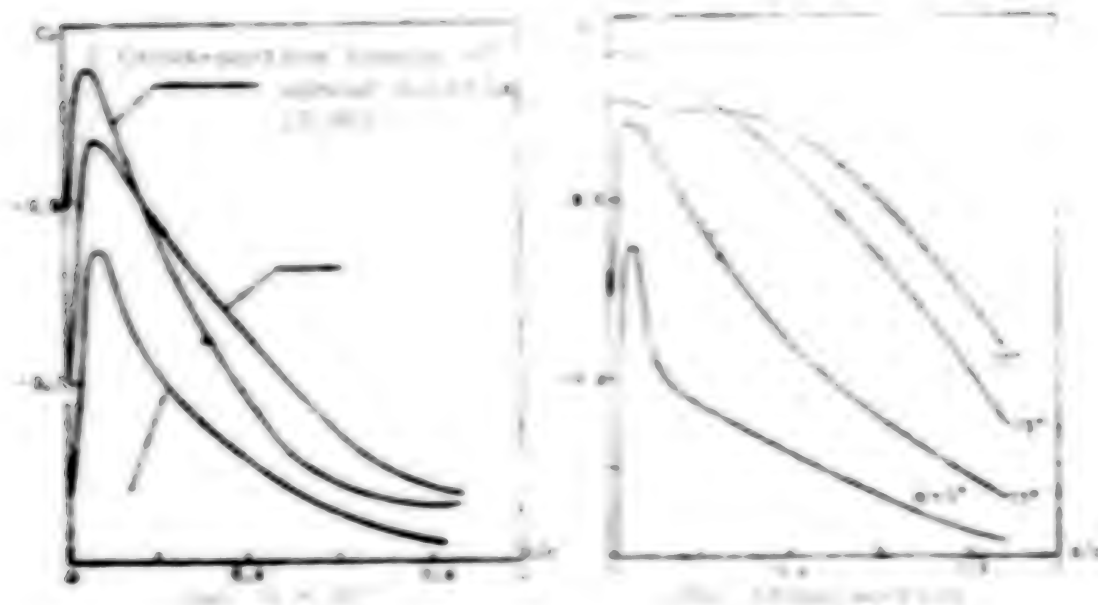
The maximum lift-drag ratio of the small panel was $b_{max} = 3.17$. A winglet at the wing tip improved the lift-drag ratio of FW.

2) Moment of force characteristics. When an AOW has a large angle of incidence, air flow separation at the wing tip causes a tendency to fall. FW does not have this shortcoming. Because of the effects of separation eddies and air flow separation at large angles of incidence at the front edge, however, the relationships in the curves m/C_L have poor linearity. After installation of a board, moment of force characteristics are improved. The improvement is most obvious on FW. When there is a large angle of incidence, the tendency toward falling without an AOW still remains. The fairing ribs had no obvious effects on moment of force characteristics.

171. Measurement of Pressure Distribution and Load Computations

The difference in flow trends between FW and AOW causes the absolute negative pressure value of the base part cross-section to be greater than the AOW part cross-section. The lift at the wing base is rather concentrated toward the front edge. This was quite evident in measurements of surface pressure distribution on the wing profile when $\alpha = 11^\circ$, as shown in Figure 6a. The back-pressure distribution is related to the downwash distribution. Naturally, the eddies caused downwash in the region of the rear side to be greater than at the front edge. As the angle of incidence is increased, the absorption peak at the front edge increases in the beginning. When the angle of incidence becomes large, air flow separation eliminates the absorption peak at the front edge and increases the load on the rear edge. Figure 6b shows that the pressure coefficient on the No. 2 (model) cross-section changes as the angle of incidence is increased.

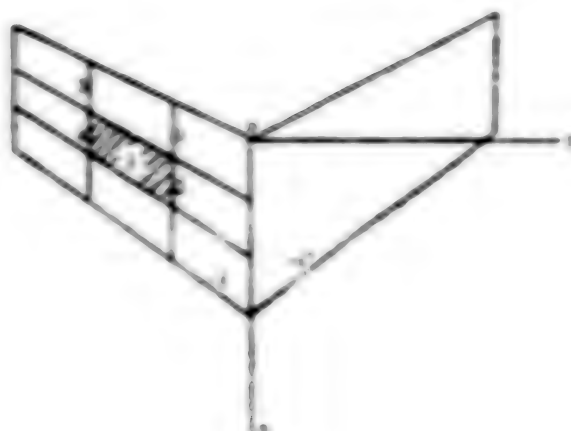
Figure 6. Pressure Coefficient Distribution



Under conditions of no air flow separation, the surface entry method can be used to calculate the load distribution of an FSW. Independent calculations were done on an FSW using a numerical model. The results show that the back load distribution conforms fairly closely to the test results. When the angle of incidence is small, say $\alpha = 5^\circ$, the load coefficient LC becomes less than 0.50 except at the front edge. When using the surface entry method for computations related to FSW, although there is no change in the basic shape of the angle, the sequence of mutual decrease in the angle point solution at normal turbulence speed is the opposite of IFW, however. The left wing of FSW is divided into n blocks. The angle point solution for the surface entry of block j for the normal turbulence speed v at the i control points (see Figure 7) is

$$\bar{W}_{i,j}^* = (W_i^* - W_j^*) - (W_i^* - W_j^*) = (\Delta W_i - \Delta W_j) = (\Delta W_i, -\Delta W_j)$$

Figure 7. Calculation of blocks of FSW



$$W_i^* = \frac{A}{L} (1 + \beta) \Delta H_i = 2 \cos \beta \cdot (2.2)$$

$$\Delta W_i = \frac{A \cdot y_i \cdot (x_i - d)}{L \cdot r^2} \quad (2.3)$$

In the formula,

$$G_i = \frac{1}{L} \sin \beta \frac{L \cdot x_i + \beta^2 y_i}{\beta \sqrt{(x_i - d)^2 + L^2 z_i^2}} \quad (2.4)$$

$$H_i = \sin \beta \cdot \frac{z_i}{\beta} \quad (2.5)$$

At subsonic speeds, $K = 1$, $\beta^2 = 1 - M^2$, $l^2 = l_1^2 + \beta^2 l_2^2$, l_1 is the tangent value of the angle of sweep of the front edge of the small fairing panel, and $d = \sqrt{x^2 + \beta^2 r^2}$, while $r^2 = y^2 + z^2$.

Determination of normal flow should correspond to the boundary condition:

$$W_n = \sum_{i=1}^n [(W_{s_i})_n + (W_{c_i})_n] \rho = (a + dz/dx) V_\infty \quad (2.6)$$

The surface eddy intensity γ_i is derived by solving this linear equation. The load coefficient of the number i panel is:

$$\Delta C_{p_i} = C_{p_i} - C_{p_{i+1}} - 2\gamma_i \quad (2.7)$$

The No 3 model FSW and the corresponding ASW were used for calculation of the lift distribution in the direction of spread for FSW, $C_{p_i}^{1/2}/C_{p_i}^{1/2}$ and the lift coefficient distribution in the direction of spread, $C_{p_i}^{1/2}/C_{p_i}^{1/2}$. It more closely approximates an optimum load distribution under conditions of equal weight than do ASW. When compared with an elliptical distribution, this type of distribution has a load distribution that is concentrated at the wing tip. The results of the computations are shown in Table 2.

Table 2. Comparison of Angle of Spread Lift Distribution

Exp (Angle of spread position)		0.2	0.4	0.6	0.8	1.0
$C_{p_i}^{1/2}/C_{p_i}^{1/2}$	FSW	1.00	1.075	1.095	0.872	0.691
	ASW	1.00	1.095	1.035	0.804	0.775
C_{p_i}/C_{p_i}	FSW	1.00	1.00	1.048	1.012	0.890
	ASW	0.940	0.975	1.032	1.100	1.132

IV. The Use of the Transonic and Supersonic Area Rule To Calculate the Zero-Lift Wave Drag of a Forward-Swept Wing Unit

Because there often were certain controlling cross-sections in the overall configuration, the optimum cross-sectional distribution for minimum zero-lift wave drag for an aircraft was derived. The Emlinton method assumes that $x = 0$, $x = 1$ and that $x = K_i (i = 1, 2, \dots, n)$. When the cross-sectional area is assumed to be $S(0) = S$, $S(1) = S$ and $S(K_i) = A_i$, the $S(x)$ distribution for minimum zero-lift wave drag and the corresponding minimum zero-lift wave drag value C_{D0} can be derived.⁵ In order to facilitate computation, the length of the fuselage is assumed to be 1. When the reference area is 1, the zero-lift wave drag coefficient can be written as:

$$C_{D0} = -\frac{1}{2\pi} \int_0^1 \int_0^1 S(x) S(x') \ln |x - x'| dx dx' \quad (3.1)$$

The above formula can be converted to a numerical solution as:

$$S(x) = \sum_{\theta=0}^{\pi} \Delta x \sin \theta \quad (0 \leq \theta \leq \pi) \quad (3.2)$$

The relationship between θ and x is:

$$x = \frac{1}{2} (1 - \cos \theta)$$

$$\alpha = \frac{\pi}{2} \int_0^{\pi} S(x) \sin \theta d\theta \quad r=1,2$$

By such conversion, the corresponding area distribution of minimum zero-lift wave drag is:

$$S(x) = N - (B - N)U(x) + \sum_{j=1}^n \lambda_j P(x, x_j) \quad (3.3)$$

In the formula,

$$U(x) = \frac{1}{\pi} [\cos^{-1}(1 - 2x) - 2(1 - 2x) \sqrt{x(1-x)}]$$

$$P(x, x_j) = -\frac{1}{2} (x - x_j)^{-1/2} \frac{x + x_j - 2xx_j + 2\sqrt{xx_j(1-x)(1-x_j)}}{x + x_j - 2xx_j - 2\sqrt{xx_j(1-x)(1-x_j)}} +$$

$$+ 2(x + x_j - 2xx_j) \sqrt{xx_j(1-x)(1-x_j)}$$

When $x = x_j$, then $P(x, x_j) = \lambda_j^2 (1 - x_j)^2$

The λ_j in the formula can be determined through the following linear equation when the given area distribution condition $x = x_j$ so that $S(x_j) = A_j (j = 1, 2, \dots, n)$:

$$\sum_{j=1}^n \lambda_j P(x_j, x_j) = (A - N) - (B - N)U(x_j), \quad j = 1, 2, \dots, n \quad (3.4)$$

After (3.4) is derived, then zero-lift wave drag is:

$$C_{w,0} = \frac{4}{\pi} (B - N)^2 + \pi \sum_{j=1}^n \lambda_j \sum_{j=1}^n \lambda_j P(x_j, x_j) \quad (3.5)$$

The remaining question is how to derive the Mach tangent area of PSW for each corresponding value of M . The Mach tangent plane of PSW can be converted to the former point on the symmetrical ASW for calculation. The front edge of the PSW is the rear edge of the ASW. The function (iv) for listing the

thickness of the wing profile is the opposite of that for AFD and there is an opposite sequential order. At the same time, the axial coordinates of the derived Mach tangent plane also are symbolic opposites.

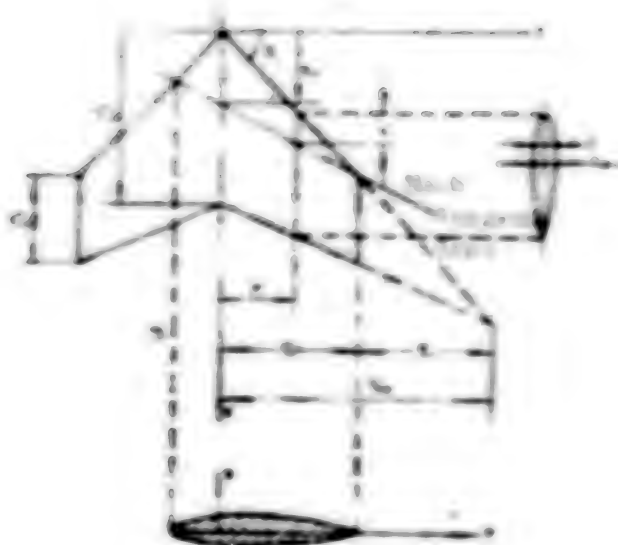
The normal projection cross-sectional area for the Mach tangent plane at a certain thickness is compared with the 1st:

$$q = 2 \sum_{i=1}^n \frac{1}{1 + \frac{1}{2} \frac{1}{\lambda_i}} \quad (3.6)$$

The s in the formula is the half-thickness of the real wing area, as shown in Figure 5.

Figure 9.

Each Youngster Area



Given that $v = \frac{B^2}{2\mu_0}$, that $\lambda_1 = \frac{2\pi}{\omega}$ and that $\omega = \frac{2\pi}{T}$, then $\frac{1}{T}$ is the natural oscillation ratio. Also $f(\omega) = \frac{12/\pi}{\lambda/c}$ is inserted into formula 1.3, then

$$\int_{-\infty}^{\infty} \frac{f(x)}{(x^2 + a^2)^2} dx = \frac{\pi}{2a^3} f(ia) \quad (3.7)$$

$$K = \frac{1}{2} m \left(1 + \frac{B \cos \theta}{18.1} \right)$$

$$m = \frac{2}{B \cos \theta} \left(K - \frac{1}{2} \right) \quad B = \sqrt{M^2 - 1}$$

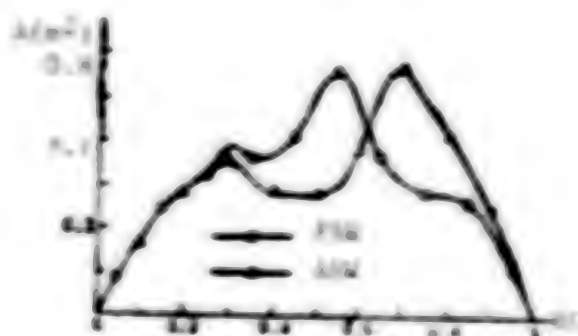
The θ is the corresponding meridian angle of the Mach oblique tangent plane. The β is the angle of sweep of the front edge.

The signs in the formula are set by having the symbol above correspond to the right wing and the symbol below to correspond to the left wing. The integral upper and lower limits are determined according to actual conditions. When intersecting with the front edge, $v = 0$ and when intersecting with the back edge, then $v = 1$. When intersecting with the side edge, $v_1 = x_1/C_1$.

As for the body of rotation of the fuselage, the normal projection of the Mach oblique tangent area can be computed using the normal tangent cross-section. When the aircraft wings are at $M = 1$, the cross-sectional area is the average value of the normally-projected Mach oblique tangent plane corresponding to each meridian angle. In this way, we can calculate the zero-lift wave drag of an FSW aircraft fitted with a canard and the equivalent body of rotation cross-section. Moreover, it can be compared with ASW. The fact that an FSW configuration more easily approximates an optimum cross-sectional area means that its low-zero-lift wave drag than an ASW configuration aircraft. The results of the calculations using model No. 1 are that, when $M = 1.2$, then the FSW $C_{D0} = 0.02009$ while the ASW $C_{D0} = 0.02425$, or it is 20 percent less. The equivalent cross-sectional distribution is shown in Figure 9.

Figure 9.

Equivalent Cross-Section Along the Axial Distribution at Mach 1.2



V. Conclusions

1. Separation occurs easily at the wing base of FSW. Flow is rather good at the tip, however. FSW have less drag and lift than ASW at identical angles of incidence. The lift-drag ratio of FSW is less than that of ASW at moderate angles of incidence. A winglet at the wing tip can improve the lift and lift-drag ratio of FSW.

2. Canards have obvious benefits in improvement of air flow separation at the wing base of FSW. Close-coupled canards have better deflectional results. When a canard is installed, the degree of improvement in the lift-drag ratio of FSW is greater than for ASW. Canards have obvious benefits in maintaining a linear relationship with moment of force.

3. A fairing panel can improve the flow field at the wing base of an FSW. The fairing panel matched with the canard should be of appropriate size. Small panels had a higher lift-drag ratio on FSW in the tests than did large panels.

4. There is a great load on the wing base of FSW and lift is rather concentrated at the front edge. Computations indicate that the load in the direction of spread more closely approximates an optimum distribution than for ASW.
5. A canard configuration on FSW facilitates a distribution that achieves the transonic-supersonic area rule. According to calculations for model No. 1, the zero-lift wave drag can be reduced by 20 percent compared with ASW.

REFERENCES

1. Kenneth, L., et al., "An Aerodynamic Investigation of a Forward-Swept Wing," AFIT/CAI/AA/770-14, 1977.
2. Lobert, G., AIAA 81-4187.
3. (Wu), F.A., "A New Analytical Method for the Aerodynamics of Subsonic Aircraft Wing and Fuselage Tail Units, Defense Industries Publishers, Beijing, 1976.
4. Rinton, E., ARC R&M No. 3641, 1963.
5. Yang Zucheng [杨祖成 1932], "Aerodynamic Design of Transonic-Supersonic Wing Bodies," NANYANG CAIJIAO ["Southern Aviation Data"], 1972.
6. Nelson, R.L. and Walsh, C.J., NASA TN D-646, 1969.
7. Sangia, R.E., "14th Congress of the International Council of the Aeronautical Sciences," ICAS-84-2.6.2, 1984.

12,539

CNO: 4088/187

CHINA'S FIRST SYMPOSIUM ON TECTONOPHYSICS HELD

Beijing DIDI LINGPO (JOURNALIC REVIEW) in Chinese Vol 11, No 4, Jul 85
p 377

[Text] In order to promote the interaction between the subbranches of earth sciences, a symposium on tectonophysics and crustal deformation was held in Beijing on 10-15 March 1983. The symposium was sponsored jointly by the Tectonogeology Committee of the China Geology Soc. and the Seismogeology Committee of the China Seismology Society. Tectonophysics is an interdisciplinary science based on and developed from traditional geology and geophysics in the last few decades. Its main scope of study is the physical nature of structural deformations on various scales of magnitude. It is related to geodynamics and geomorphology but has a different emphasis. Both provide scientific basis for mineral resources development and for minimizing earthquake damages.

In the meeting, more than 90 papers were presented by 180 participants representing 14 units from the State Seismological Bureau, the Chinese Academy of Sciences, institutes of geology, coal, petroleum, chemical engineering, and mining, and institutes of higher learning. Topics discussed in the symposium include structural deformation on various magnitude scales, the inception and the temporal and spatial distribution of earthquakes, and the mine formation mechanism. Presentations are based on field survey, earth stress, deformation, and seismological observations, and numerical and mathematical modelling. This symposium demonstrated the recent developments and trend of tectonophysics in China. Notably features are: (1) Geophysical and geodetic survey of tectonology has greatly improved the depth, breadth, and resolution of field observations, and helped to quantify the study of structural deformation. Papers presented in the symposium include studies of the structural movement at Wenshanhan, the horizontal deformation field and stress field of the Beijing region, the radial-arcuate orthogonal seismic zone in northern China, small scale convection in the upper mantle and the stress distribution of the subduction zone of plates. These studies made use of geological deformation and stress data and seismology and satellite gravity data. (2) The wide application of mathematical mechanics principles and mathematical modelling shows that tectonophysical research in China has made considerable progress toward quantification. Numerical and analytical methods have been applied to the study of fracture propagation, w-shaped fracture, scarp-shaped fault, triangular structure and microstructures, and earthquake threats and nine

Germanium detectors. More significant development is the application of the finite element method and finite-difference modeling and stress-strain-rate modeling. Such simulations have elevated the mathematical modeling of fault-slip behavior to a new level. (1) More and more attention is given to the uniqueness and complexity of structural deformations with respect to the medium environment and spatial and temporal distribution, and to the importance of high temperature and high pressure rock behavior. As a result of recent efforts, there has developed practical experimental techniques for rocks under high pressure and at high temperature. Triaxial testing equipment has been constructed using liquid, gas, or solid medium and the pressure has reached 10 kbar at room temperature, 5.5 kbar at 500°C and 7.5 kbar at 800°C. The solid medium triaxial testing equipment has also facilitated the simulation study of the strongly anisotropic and fluid environment of the process of the earth. Progress in the investigation of fault behavior, including stress, rate, and strain, fracture and rotation in rocks and deformation, in particular, provides increasingly and increasingly direct effects, such as porosity, anisotropy, and viscosity, upon studies such as structural evolution. (2) A series of studies by means of experimental studies is being in the investigation of the microscopic processes and the mechanism of deformation. A number of papers dealt with the deformation stages and stress behavior, the stress-strain rate sensitivity, and the control of the formation of the grain and the crystal lattice in the solid state. These studies have indicated a direct effect of initial structure, anisotropy, grain shape, and partial release of rock tension rate and rate pressure, and thermodynamic relationships.

The participants of this workshop include, for the first time, the scholars and the young generations. Translation into more young researchers has become an important in the meeting. The meeting will be organized and presented in a book and online form. It will promote the development of intergenerational exchange and to facilitate scientific exchange and cooperation. The workshop is also presented to highlight a transnational approach about the global importance of the International Commission of the Great Lakes and the transnational cooperation of the Great Lakes basin and also promote a strong transnational cooperation in the South region of India.

Source: Journal of the American Statistical Association, 1974, 69, 127-130.
 (National Bureau of Economic Research, Inc., New York, NY 10019)

Both alkylbenzene sulfonate (ABS) and alkyl sulfonate (AS) are major active components of current synthetic detergents. The potential mutagenicity of ABS and AS were investigated with *Salmonella typhimurium* test, no significant or consistent difference was detected between ABS (5~30 μ g/ml) or AS (0.01~0.5 μ g/ml) and control. Also there was no difference whether the metabolic activation system of S9-mix was used or not. Treatment of ABS (1~10 μ g/ml) or AS (0.001~0.7 μ g/ml) alone raised no significant increase of SCE frequency in Chinese hamster Wg3-h cells. Treatment of Wg3-h cells with various doses of Methylmercury C (MMC) from 0.005 to 0.05 μ g/ml caused a significant dose-dependent increase of SCE frequency. The increase was significantly inhibited by concurrent addition of a fixed dose of ABS (5 μ g/ml) or AS (0.01 μ g/ml). Furthermore, Wg3-h cells exposed to MMC at a fixed dose of 0.025 μ g/ml plus various lower ABS dose from 0.01~0.0005 μ g/ml or to AS at a fixed dose of 0.005 μ g/ml plus various MMC dose from 0.01~0.005 μ g/ml all observed a dose-dependent inhibitory effect on MMC-induced SCE. These results indicate that under certain conditions, ABS and/or AS suppress the SCE frequency induced by MMC. We suggest that ABS and/or AS might have some effect on the protection of human against environmental harmful factors.

- [1] Zhang Yuzhan [张钰展], 1981, 2283, RYTHM NUCLEIC ACID CONCENTRATIONS (CONCENTRATIONS) IN CHEMICAL INDUSTRY, 7 (1981) 49.
- [2] B. N. Ames et al., *Mutat. Res.*, **31** (1974) 347.
- [3] J. L. Hunt et al., *Mutat. Res.*, **61** (1978) 367.
- [4] K. Imai et al., *Food Cosmet. Toxicol.*, **18** (1980) 289.
- [5] M. Mametani et al., *Res. Ind. Pol. Health*, **27** (1980) 113.
- [6] Y. C. Chang et al., *Chemosphere*, **3** (1974) 2.

AUTHOR: SUN Haoqing [1327 3165 3237]
ZHENG Shanliang [6774 0810 9326]
LI Junying [2621 0689 3892]

ORG: None

TITLE: "Preliminary Studies On the Preparation of a Ribosomal Vaccine From Bacteria S-O₂-1 and Its Antitumor Activity"

SOURCE: Shanghai FUDAN XUEBAO (ZIRAN KEXUE BAN) [JOURNAL OF FUDAN UNIVERSITY (NATURAL SCIENCE)] in Chinese Vol 24, No 2, Jun 83 pp 112-114

TEXT OF ENGLISH ABSTRACT:

This paper is the first report on the ribosomal vaccine from Gram negative bacteria (S-O₂-1) in China. Various techniques such as ultrasonic disruption, differential centrifugation and gel filtration were used for its isolation. The results showed that the ribosomal vaccine could stimulate the immune response of spleen in mice, and suppress the proliferation of transplanted S-180 tumor cells in the peritoneal cavity of mice.

When used in combination with the incomplete Freund's adjuvant, the inhibitory effect of the vaccine became much higher than that of the vaccine used alone. And the toxicity of ribosome was lower. The results could provide some facts for the clinical preparation of antitumor immunopotentiators. (Paper presented at the 1st Symposium on the

ZPBS-CST-84-006

29 October 1984

AUTHOR: GU Youliang (5170 0645 5128)
 WANG Huiliang (3789 1924 7451)
 ZHOU Lirong (0719 7787 5554)
 et al.

ORG: Institute of Chemistry, Chinese Academy of Sciences

TITLE: "Determination of the Chemical Composition and the Crystal Modification of the Ziegler-Natta Catalyst Prepared from the Alkyl Titanium Chloride"

SOURCE: Beijing WAFENZI TONGJIN [POLYMER COMMUNICATIONS] in Chinese No. 1, Feb 85 pp 54-57

TEXT OF ENGLISH ABSTRACT: The elemental analysis data and corresponding gel chromatography indicated that the empirical compositions of the intermediate compounds obtained by reducing $Ti(OC_2H_5)_2Cl_2$ with $AlEt_3Cl$ are $Ti(OC_2H_5)_2Cl_2$ (I) and the catalysts obtained through the heat treatment of $Ti(OC_2H_5)_2Cl_2$ by means of $TiCl_4$ have the formula of $TiCl_3 \cdot 0.02 AlCl_3 \cdot 4.05 (n-C_2H_5)_2O$ (II). The X-ray diffraction pattern showed that (I) is an amorphous material and (II) is $\gamma-TiCl_3$. (II) has almost the same crystal modification (2θ (deg) = 15.13, 15.93 and 21.22) and average size of crystallites (100 Å) as the Solway catalyst (III) prepared from $TiCl_4$. (Paper received on 29 October 1983.)

AUTHOR: GUAN Jiyu [1926-1987] (Jin)
QIAN Renyuan [1927-1988] (Jin)
ZHANG Fengfa [1928-1988] (Jin)
et al.

ORG: GUAN and QIAN of the Institute of Chemistry, Chinese Academy of Sciences; ZHANG, et al., of the Institute of Atomic Energy, Chinese Academy of Sciences

TITLE: "Effect of the State of Macromolecular Aggregation on the Uranium Nuclear Fission Tracks in PET Films"

SOURCE: Beijing GAOFENZI JINCHEN (POLYMER CONCENTRATIONS) in Chinese No. 1, Feb. 85 pp. 62-65

TEXT OF ENGLISH ABSTRACT: ²³⁵U fission track observations have been performed for PET samples stretched and heat treated under different conditions. These damage tracks may be revealed and made visible under an ordinary optical microscope by treatment with KM solution that rapidly and preferentially attacks the damaged material. As the stretching and annealing of PET films causes change in the state of macromolecular aggregation in the film, the diffusion-etching rate of the KM solution will be changed accordingly. Anisotropy in the diffusion-etching rate gives an anisotropy in the diameter of the track cross section. (Paper received on 11 November 1981)

AUTHOR: LIU Rioming [0491 2556 2494]
ZHAO Ruoshan [0392 5478 1472, deceased]

ORG: Beijing Institute of Chemical Technology

TITLE: "A New Electron Microscopy Staining Method for Morphological Studies of Rubber-Modified PVC--The Sulfochlorides-Heavy Metal Staining"

SOURCE: Beijing GAOFENZI TONGJIN [POLYMER COMMUNICATIONS] in Chinese No. 1, Feb 83 pp 66-69

TEXT OF ENGLISH ABSTRACT: A sulfochlorides-heavy metal staining method is developed for morphological studies of rubber-modified PVC (PVC/CPE, PVC/EVA, PVC/MBS, PVC/ACR, etc.). The staining procedure is as follows: Specimens react with HSO_3Cl below -5°C , then are embedded in epoxy resin and microtomed. The ultrathin sections are stained with Hg_2Ac_2 or OsO_4 for TEM. This method is simpler and more effective, and the period of staining is much shorter, than those reported in the literature. (Paper received on 17 November 1983.)

AUTHOR: JIA Lei (9128-4124)
CHEN Baili (77115-9477-1871)
WANG Ruogang (13708-441) (111)

ORG: Institute of Chemistry, Chinese Academy of Sciences

TITLE: "Preparation of Activated Carbon Fiber (ACF) Containing Nitrogen Atom and its Adsorption Behavior"

SOURCE: Beijing CAOPHIL TUNING (POLYMER COMMUNICATIONS) in Chinese No 1, Feb 85 pp 70-72

TEXT OF ENGLISH ABSTRACT: Polyacetylenitrile (PAN) fiber was activated at various temperatures for varying lengths of time in different fluxes of CO_2 . In this experiment, the best conditions for activation were a temperature of 850°C , time period of 2 hours, and CO_2 flux of $\sim 1\text{ L/min}$, which produced an ACF having a specific surface area of $800\text{--}1000\text{ m}^2/\text{g}$ and absorbing KI , $50\text{--}70\%$ percent (in weight). It has been found that the PAN ACF possesses the same properties as the viscose ACF made in Japan through the determination of adsorption, desorption and pore diameter distribution. In addition, the pore diameter distribution is narrow and the peak of distribution is about 30 \AA . It has a larger specific surface, enabling easy adsorption and quick desorption as compared with the conventional activated carbon. It is being regarded as a new absorbent. (Paper received on 7th December, 1984.)

AUTHOR: DAI Mingchang [410] 2496-2549/
SHI Lijuan [1127 7787 1227]
SHI Yaowu [2097 5009 2976]
et al.

ORG. Institute of Elemento-Organic Chemistry, Nankai University

TITLE: "Study of Molybdenum Complexes Catalyzed Copolymerization of Propargyl Alcohol and Propargyl Chloride"

SOURCE: Beijing CAIFENZI TONGJIN [POLYMER COMMUNICATIONS] in Chinese-No. 1,
Feb 85 pp 73-76.

TEXT OF ENGLISH ABSTRACT: The polymerization of acetylenes has been studied extensively since the polymers obtained are a kind of prospective material of organic conductor and semiconductor.

It was found that, in the presence of molybdenum complexes, propargyl alcohol and propargyl chloride copolymerized with vigorous reactions. The polymer obtained was insoluble in all solvents studied, and polymer II was soluble in methanol, chloroform, acetone, etc., with a molecular weight of 700-1000.

The authors have tried using nine complexes of Ti, Zr, Fe, Co and Ni as the catalyst, but no reaction has taken place. (Paper received on 16 December 1983.)

9717
USO: 4009/1116

24 October 1985

AUTHOR: SU, Chengyan (711.814.444)

ORG: Guangzhou Research Institute of Non-Ferrous Metals

TITLE: "Optimal Carrier Gas Flow Rate in Inductively Coupled Plasma Atomic Emission Spectrometry"

SOURCE: Guangzhou FENXI BEAO (ANALYTICAL CHEMISTRY) (In Chinese Vol 1)
No 5, 20 May 85 pp 121-124

TEXT OF ENGLISH ABSTRACT: It is shown experimentally that the optimal carrier gas flow rate of ICP-AES is determined by ICP power and excitation potential of the analytical spectral lines and is independent of the type of nebulizing system used and its performance. The range of carrier gas flow rate obtainable from the nebulizing system must match the ICP parameters. (Paper received on 13 February 1984.)

AUTHOR: LIE Gene (6790 1706 3134)
CHENANG Changqun (2791 7122 1714 1141)
WEN Bo (1629 3134)
TANG Xi (2799 3556)
et al.

ORG: LIE, CHENANG and WEN of the department of Chemistry, Jiangxi University; TANG, et al., of Jiangxi Copper Plant, Jiangxi Copper Company.

TITLE: "Studies of Supercritical Extraction Spectrophotometry. II. Determination of Trace Gold in Ore"

SOURCE: Changchun HANXUE BEKATE (ANALYTICAL CHEMISTRY) in Chinese Vol 13 No 11
20 May 85 pp 326-329

TEXT OF ENGLISH ABSTRACT: Gold in the sample solution is extracted with a surf foam loading with 0.20 ml H₂O₂, and then color is developed in a weak acidic medium with 4,4'-bis (dimethylamino)-thiobenzophenone (TMB). The resulting Au-TMB complex can be measured directly by dual-wavelength spectrophotometry. The method has been applied to the determination of Au down to 0.01 g/t in ores with satisfactory results. (Paper received on 29 February 1984.)

AUTHOR: SUNG Junteng [1345 0193 1496]
CAO Yuanshe [2580 0337 0772]
WU Yinhua [3170 3593 5470]

ORG: Department of Chemistry, Northwest University

TITLE: "Polarographic Study of Metal-6-(2-Pyridylazo)-Resorcinol (PAR)
Complex. III. Catalytic Polarographic Wave in Naphium (V)-Tartaric Acid-
PAR-NaClO₄ System"

SOURCE: Changchun FENXI XUEBAO [ANALYTICAL CHEMISTRY] in Chinese Vol 11 No 5,
74 May 85 pp 317-319

TEXT OF ENGLISH ABSTRACT: In a supporting electrolyte of $1.0 \times 10^{-3}M$
PAR-0.01M tartaric acid-2.2M NaClO₄ (pH 1.940.1) naphium (V) produces a
sensitive catalytic wave with peak potential at $-0.80V$ (vs SCE). The wave
height is proportional to the concentration of Na(V) in the range of 1 ppb
to 80 ppb. It is in 4000-fold excess relative to 0.01 ppm Pb does not interfere.
The method has been used for geochemical samples. (Paper received on
22 May 1984.)

AUTHOR: HE Xiwu [0149 6932 2429]
LI Yunhua [2621 0061 5478]
SHI Huiming [0670 1979 2494]

ORG: Department of Chemistry, Xiamen University

TITLE: "Optimization Design Investigation of Spectrophotometric Analysis by Weighted Centroid Simplex Method"

SOURCE: Changchun FENXI HUAXUE [ANALYTICAL CHEMISTRY] in Chinese Vol 11 No 5, 20 May 85 pp 344-349

TEXT OF ENGLISH ABSTRACT: An improved simplex optimization procedure based on the weighted centroid method has been developed which shows promise as a method for accurate and rapid search of an optimum region.

We applied this procedure to a nonlinear equation and two color reaction systems. The proposed procedure has been shown to yield the correct experimental conditions for two systems. (Paper received on 11 June 1984.)

AUTHOR: FANG Shengqiang (193) 2314 1730
FU Li'an (1128) 6319 1366

ORG: Department of Modern Physics, Lanzhou University

TITLE: "Conductometric Determination of Crown Ether Content"

SOURCE: Changchun FENXI SHIYAN [ANALYTICAL CHEMISTRY] in Chinese Vol 11 No 5,
24 May 85 pp 349-353

TEXT OF ENGLISH ABSTRACT: A new method for the determination of crown ether content is described. Let a kind of crown ether dissolve in a certain amount of low dielectric constant solvent chloroform and add a solid metal salt (e.g., as alkali metal picrate) in excess. The chosen salt is hardly soluble in the solvent, and capable of complexation with the crown ether for determination. After the reaction equilibrium is obtained, the electric conductance of the system, L , is measured. Then the concentration of crown ether, C , can be drawn by the equation $C/L = Q/L + P$, where Q and P are constants. (Paper received on 14 June 1985.)

AUTHOR: SU Qiang [1985 0987]
WANG Hongyan [1985 070] (p41)

ORG: Changchun Institute of Applied Chemistry, Chinese Academy of Sciences

TITLE: "Determination of Nd^{3+} in the Laser Crystal $\text{Y}_3\text{Al}_2(\text{O}_4)_3/\text{Nd}^{3+}$ by Magnetic Balance"

SOURCE: Changchun JENK HEART (ANALYTICAL CHEMISTRY) in Chinese Vol 17 No 1, 10 May 85 pp 334-336

TEXT OF ENGLISH ABSTRACT: Magnet. susceptibilities of laser crystal $\text{Y}_3\text{Al}_2\text{Nd}^{3+}$ were determined at 10°C by magnetic balance. The increased linearly with the increasing concentration of Nd_2O_3 . Using the linear equation $\text{Nd}_2\text{O}_3(\text{wt. percent}) = a\chi_b + b$, the concentration of Nd_2O_3 in $\text{Y}_3\text{Al}_2\text{Nd}^{3+}$ can be determined rapidly by the magnetic susceptibility (χ_b) measured. Solid powder samples may be used directly without decomposition, separation or other time-consuming processes. (Paper received on 15 June 1984.)

AUTHOR: LIE Yaru (1981 3768 5423)
CHEN Mingde (1115 2580 5795)
ZHU Shugen (0719 7885 2704)

ORG: Second Department, Chengdu College of Geology

TITLE: "Studies of a New Color-Forming System. (II). The System $Hg(II)-1,3,5$ -Dichloro-2-pyridylazo-2',4'-Dianthracene-Sulfone-Sodium Dodecylbenzenesulfonate"

SOURCE: *Chungkuo Hsueh Hsueh (ANALYTICAL CHEMISTRY)* in Chinese Vol 11 No 2, 20 May 83 pp 161-161

TEXT OF ENGLISH ABSTRACT: The optimum conditions for the color reaction of $Hg(II)-1,3-Cl_2-PADAT-SDBS$ have been studied systematically. In a tartaric buffer solution at pH 3.8 to 5.0, $Hg(II)$ forms a red ternary complex with $1,3-Cl_2-PADAT$ in the presence of SDBS. The maximum absorption is measured at 520 nm with molar absorptivity being $5.11 \times 10^4 \text{ l mol}^{-1} \text{ cm}^{-1}$. The ratio of $Hg(II)$ to $1,3-Cl_2-PADAT$ to SDBS in the ternary complex has been found to be 1:2:4. A linear relationship is obtained in the concentration range of 2.5 to 76 $\mu\text{g/25 ml}$. The method is simple, rapid and accurate, and can be applied to the spectrophotometric determination of mercury in water. (Paper received on 3 January 1984.)

8717

ORG: 8099/1120

AUTHOR: None

ORIG: The Division of Scientific Research, Nanjing University

TITLE: "The Great Achievements of Nanjing University's Scientific Research in the 35 Years Since the Founding of the PRC"

NOTE: Nanjing DAXUE GAOJIAO JIKAN (JIAN KEXUE) (JOURNAL OF NANJING UNIVERSITY (NATURAL SCIENCES EDITION)) in Chinese Vol 20 No 4, Dec. 84 pp 505-513

TEXT OR SUMMARY ABSTRACT: The great achievements of this university in scientific research during the 35 years since the founding of the PRC under the leadership of the Party are described in this paper. The university has gone through four stages of scientific research.

I. Initial Period (1947-1956)

Most of the teachers selected their own research topics based on the academic speciality of the old teachers. Although there were not many scientific research projects and topics, they reflected a significant level of academic research and showed particular characteristics;

II. Period of Overall Expansion (1956-1966)

Scientific research developed overall from decentralized and self-selected research to unified, organized and planned research;

III. Period of Setbacks (1966-1976)

Because of 10 years of internal disorder, scientific research in this university was hit by an unprecedented setback. Under extremely difficult circumstances, our teachers persisted in their work and did not allow their scientific research to completely stop;

IV. Flourishing Period (1976-present)

Under a corrected line, by emancipating the mind and inspiring enthusiasm, the scientific research of this university has taken on a new and flourishing look. A series of gratifying achievements have been accomplished by unifying the methods of basic research and applied research, and by developing interdisciplinary research.

When we look to the future, the responsibilities and tasks are heavy and the road is long. This university is determined to follow the guidelines of educational reform, "Learning modernization, the world and the future," and stride forward toward the great goals of education and scientific research.

AUTHOR: 20 Anna [7351 1609 4877]
12 Russian [7120 1937 4341]
20 Yawen [6757 1589 3634]

ORG: Nanjing University

TITLE: "Process of Formation and Thermal Decomposition of Tetragonal Structure Oxalate"

SOURCE: Nanjing NANJING DAXUE XUEBAO (NANJING UNIV.) [JOURNAL OF NANJING UNIVERSITY (NATURAL SCIENCES EDITION)] in Chinese, Vol. 20 No. 4, Dec. 84, pp. 786-790

TEXT OF ENGLISH ABSTRACT: The tetragonal structure oxalate was prepared by coprecipitation with $(NH_4)_2C_2O_4$ solution as the precipitant. The processes of formation and thermal decomposition of these compounds were studied by X-ray diffraction, electron microscope observation and magnetic analysis. The following conclusions were obtained: (1) The tetragonal structure oxalate is transformed from an α -type oxalate in $(NH_4)_2C_2O_4$ solution. (2) The thermal decomposition of these compounds is similar to that of α - and β -type oxalates. (Paper was received on 19 April 1983.)

AUTHOR: SHEN Bao (1959 1185)
YE Lei (1973 1621)

ORG: Nanjing University

TITLE: "A New Method for the Purification of Wastewater Containing Chromium Ions"

SOURCE: Nanjing XIAOJIN DAXUE XUEBAO (JIAN XIAO) [JOURNAL OF NANJING UNIVERSITY (NATURAL SCIENCES EDITION)] in Chinese: Vol 26 No 4, Dec 84, pp 791-795

TEXT OF ENGLISH ABSTRACT: As a new electrochemical concentrative material, the carbon-mat electrode is recommended for the purification of wastewater containing chromium ions. After chemical treatment, the primary collecting efficiency of the carbon-mat electrode reaches almost 98 percent, which makes it ideal for the purification of wastewater. The experiment can be carried out easily and the operation is simple, successful, rapid and has good reproducibility. All experimental data were determined through atomic absorption spectrometry.

9717
CSN: 8009/1106

JPES-CST-05-0116
21 October 1985

AUTHOR: CAI Deshui [5591 1795 2055]
MA Cuoqi [7456 0948 2475]
KONG Funing [1060 4395 1317]
et al.

ORG: Department of Precision Instruments Engineering

TITLE: "Focal Characteristic Analysis of Spherical Geodesic Optical Waveguide Lens"

SOURCE: Tianjin TIANJIN DAXUE XUEBAO [JOURNAL OF TIANJIN UNIVERSITY]
in Chinese No 1, Jan 85 pp 20-25

TEXT OF ENGLISH ABSTRACT: The aberration of the spherical geodesic optical waveguide lens and the light intensity distribution at its focal plane have been calculated by ray tracing and Fourier Transformation techniques. The optimum aperture of this lens and the minimum size of the focal spot can also be determined conveniently with our computer program. In addition, the aberrations of the lens is corrected with the twice ion-exchange method inside the sphere. Both sphere and plane waveguides in our lens are of a single mode, and the measured effective index ratio of their TE_1 mode is 1.007, while the focal spot of 16 μm is obtained at a relative aperture of 0.7. The experiment results are in good agreement with the theoretical analysis. (Paper received on 21 May 1984.)

AUTHOR: SUN Renze [1327 0117 1795]
SUN Dong [1327 3767]
LI Dengping [6124 6098 1627]
et al.,

ORG: All of Tianjin University

TITLE: "The Application of Image Processing by a Microcomputer in Welding Electric Arc Research"

SOURCE: Tianjin TIANJIN DAXUE XUEBAO (JOURNAL OF TIANJIN UNIVERSITY)
in Chinese No 1, Jan 85 pp 102-106

TEXT OF ENGLISH ABSTRACT: Image processing by a microcomputer is a new development in computer applications. Welding electric arc is a heat source with high temperature and strong light, and is hard to investigate by ordinary methods. This paper describes how the temperature field of welding electric arc was measured by the use of pictures taken by an ultrared camera and a microcomputer. The interrelationship between the welding electric current and welding temperature field was obtained when D.C. TIG welding was applied to stainless steel. Under the arc with an Ar+H₂ protecting gas, a clear image and arc structure was produced by the false color method. (Paper received on 5 April 1984.)

9717
CSC: 6009/1119

AUTHOR: GU Yidong [7357 5065 2639]
 YU Lianmin [0205 3550 3046]
 WU Jieda [0702 0094 6671]

ORG: None

TITLE: "Research On the Properties of Blue Tungsten Oxide Prepared By Intramolecularly Reducing Method"

SOURCE: Shanghai FUDAN XUEBAO (ZIRAN KEJUE BAK) [JOURNAL OF FUDAN UNIVERSITY (NATURAL SCIENCE)] in Chinese Vol 24, No 2, Jun 85 pp 141-146

TEXT OF ENGLISH ABSTRACT:

A new method for preparing blue tungsten oxide was described. With APT as raw material, named IRT (Intramolecularly Reducing Tungstate) was synthesized. Then, IRT was heated in N₂ atm at 620 ± 30°C, for 0.5 hour to give blue tungsten oxide and the blue tungsten oxide was investigated by X-ray diffraction, I. R. spectroscopy, S. E. M. and chemical analysis.

The crystal of the blue tungsten oxide was simple, WO₃. Purity > 99.99% and surface area 22~30 m²/g. Other properties, K⁺-absorption and true density were reported too.

The blue tungsten oxide prepared by this way is an ideal intermediate material for manufacturing products of tungsten. (Paper received on 3 March 84)

- [1] Kirk-Othmer, Encyclopedia of Chemical Technology, Vol. 22, Wiley, New York (1963), p. 544.
- [2] J. C. Bailar, Comprehensive Inorganic Chemistry, Vol. 3, Pergamon, Oxford (1973), p. 744.
- [3] DT 2,646,756 (1976).
- [4] SU 584,302 (1977).
- [5] Fr 1,328,880 (1963).
- [6] Jap 79 25,256 (1979).
- [7] K. G. Bartaeva, C. A., 87/1982/200221a.
- [8] Jap 75 92,906 (1975).
- [9] B. A. Kim and F. Tlaga, Acta Chem. Acad. Sci. Hung. 104 (1980) 211.
- [10] Bartaeva Lashin, Acta Chem. Acad. Sci. Hung. 101 (1979) 127.
- [11] GB 946,063 (1964).
- [12] US 3,054,654 (1962).
- [13] Zhuzhou Hard Alloys Plant, YINGZHI HEJI (HARD ALLOYS), 3 (1980) 90.

AUTHOR: JU Linyu [2040 0243 3768]
GU Yidong [7357 5065 2639]

ORG: None

TITLE: "Preparation of 11-Tungsto-niobo-phosphoric Acid and Its Properties"

SOURCE: Shanghai FUDAN XUEBAO (ZIRAN KEXUE BAN) [JOURNAL OF FUDAN UNIVERSITY (NATURAL SCIENCE)] in Chinese Vol 24, No 2, Jun 85 pp 147-152

TEXT OF ENGLISH ABSTRACT:

11-Tungsto-niobo-phosphoric acid was prepared by mixing proper amounts of sodium niobate, tungstate and phosphate in alkaline solution, followed by acidification with sulfuric acid to pH 0.95, and then boiling for 15 minutes. Isolation of the solid was performed through formation of ethyl ether adduct. Dilute sulfuric acid, 0.2M, may be used for further purification through recrystallization.

U. V. absorption spectra, I. R. spectra and DTA all indicate the resemblance between $H_2(PNbW_{11}O_{68}) \cdot x H_2O$ and $H_2(PW_{11}O_{68}) \cdot x H_2O$. (Paper received on 1 March 1985)

12949

CSO: 4004/1002

AUTHOR: HUANG Chaoben [1906 1900 1989]
D. Elwell
R.S. Feigelson

JPRS-CST-85-036
21 October 1985

ORGL: HUANG of the Research Institute for Synthetic Crystals, State Administration of Building Materials Industry, Elwell and Feigelson of Stanford University

TITLE: "Computer Study of the Influence of System Parameters on Interface Shape During Bridgman Growth"

SOURCE: Beijing GUISHIYAN XUEBAO [JOURNAL OF THE CHINESE SILICATE SOCIETY] in Chinese Vol 13 No 2, Jun 85 pp 129-134

TEXT OF ENGLISH ABSTRACT: Finite element computer analysis was used to investigate the influence of interface position, temperature gradient, growth rate and latent heat on the interface shape during crystal growth by the Bridgman method. The interface shape was found to depend critically on the distance from the interface to the point where the temperature gradient changes steeply. Heat transfer brought about by moving the crucible, as expected, has a tendency to make the interface more concave. (Paper received on 15 August 1984.)

AUTHOR: HUANG Pengnian [7806 1756 1628]
HUANG Xihua [7806 3356 2037]

ORG: Shanghai Institute of Ceramics, Chinese Academy of Sciences

TITLE: "Li⁺-H⁺ Ion Exchange of Glasses in Li₂O-(LiCl)₂-B₂O₃-Al₂O₃ System in Water Solutions"

SOURCE: Beijing GUISUANYAN XUEBAO [JOURNAL OF THE CHINESE SILICATE SOCIETY] in Chinese Vol 13 No 2, Jun 85 pp 159-163

TEXT OF ENGLISH ABSTRACT: The lithium chloro-alumino-borate glasses were immersed in buffer solutions, and the change in pH value of the solutions with time was measured. The reaction process of glasses in the solutions and the change of ion exchange of glasses with their compositions were analyzed. It was found that the ion exchange ability of glasses has a good relationship with the ionic conductivity. It follows that the ionic conductivity of glasses mainly depends on the mutual forces of Li⁺ ions with anions or anion groups, and this supports the weak electrolyte theory on the ionic conduction of glass. (Paper received on 12 December 1983.)

AUTHOR: WANG Zhongcai (3709 0022 2008)
WANG Shizhuo (3709 0013 0743)
LIU Hanning (0491 3352 5281)
et al.

ORG.: WANG Zhongcai and WANG Shizhuo, et al., of Changchun Institute of Optics and Fine Mechanics, Chinese Academy of Sciences, LIU of Jilin Provincial Chemical Fiber Laboratory

TITLE: "Investigation of Network Structure for Antimony-Borate Glasses"

SOURCE: Beijing GUOSIYANTAN XUEBAO (JOURNAL OF THE CHINESE SILICATE SOCIETY) in Chinese Vol 13 No 2, Jun 85 pp 169-173

TEXT OF ENGLISH ABSTRACT: The network structures of glasses of $2\text{Sb}_2\text{O}_3 \cdot 4\text{B}_2\text{O}_3 \cdot 4\text{H}_2\text{O}$ (NKK) and $1.5\text{Sb}_2\text{O}_3 \cdot 4.5\text{B}_2\text{O}_3 \cdot 3.5\text{H}_2\text{O} \cdot 0.5\text{H}_2\text{O}$ (KKE7) systems have been investigated by IR spectra analyses and the radial distribution functions obtained from X-ray diffraction measurements. It is found that the coordination numbers of Sb and B atoms are 5.0-5.6 and 3 or 4 respectively.

Experimental results indicate that the average bond length of the Sb-O bond is 1.88-1.92 Å, and the distances between Sb-O, O-O and Sb-Sb are 3.11, 3.17 and 3.65(Å) respectively. Based on infrared spectroscopic analyses, the peaks for the bond vibration of glasses are: 1640 cm^{-1} and 1220 cm^{-1} (B-O-B), 1040 cm^{-1} or 920 cm^{-1} (O-B-O), 1330 cm^{-1} (Sb-O-B) and 870 cm^{-1} , 780 cm^{-1} (O-Sb-O). In other words, the characteristic absorption of BO_2 and NBO_2 coexist with BO_3 in the network structure. In this case, the fraction α_2 of BO_2 depends on the contents of K_2O and Sb_2O_3 . This is similar to the results obtained in the system $\text{K}_2\text{O}-\text{B}_2\text{O}_3$ by P.J. Bray using the NMR method.

A model of the NKK glass network structure has been proposed based on the analyses and experimental data. The network structure consists of 6 and 4, circular structural units formed by SbO_4 , BO_3 , and BO_2 . (Paper received on 16 May 1984.)

AUTHOR: YANG Wenxiong [2798 2429 2574]
YAO Bingrong [5135 3521 1837]

ORG: YANG of Shanghai Jiaotong University; YAO of Linhu Glass Factory,
Shanghai

TITLE: "On the Fluid Dynamics Calculation of the 02.2m Astronomical
Telescope Lens"

SOURCE: Beijing GUISHIYAN XUEBAO (JOURNAL OF THE CHINESE SILICATE SOCIETY)
in Chinese Vol 13 No 2, Jun 85 pp 178-182

TEXT OF ENGLISH ABSTRACT: Fluid dynamics for the 02.2m astronomical
telescope lens have been studied. Several problems are presented in this
paper, such as the critical condition for the vortex of the glass liquid
occurring in a single crucible, the calculation of the lowering of the
liquid surface and casting period, the effect of the end of a cylindrical
pipe on the calculation and the selection of the simulated criterion number.
(Paper received on 9 October 1983.)

AUTHOR: CHEN Shusheng [7115 0700 3917]
LI Xian [2621 0207]

ORG.: Xian Institute of Optics and Fine Mechanics, Chinese Academy of Sciences

TITLE: "The Absorption of ^{60}Co Narrow Beam γ -ray in Optical Glasses--
On the Relationship Between Linear Absorbing Coefficient, Lead Equivalent
and Density"

SOURCE: Beijing GUISHANYAN XUEBAO [JOURNAL OF THE CHINESE SILICATE SOCIETY]
in Chinese Vol 13 No 2, Jun 85 pp 183-189

TEXT OF ENGLISH ABSTRACT: An assumption that absorption of ^{60}Co narrow beam γ -rays in glass or other materials merely depends on the mass per unit area perpendicular to the γ -ray is made in this paper. According to this assumption, a relationship between the linear absorbing coefficient, the lead equivalent and density is deduced. For some glasses the given theoretical values of the lead equivalent are compared with the experimental values. It is proven from the comparison that the theoretical values are in agreement with the experimental ones. Therefore, the measurement of the lead equivalent and linear absorbing coefficient of glasses can be simply converted to the measurement of their densities. In addition, similar problems with other materials are discussed in this paper. (Paper received on 24 May 1984.)

AUTHOR: Liu Changling (1949-1991) [1991]

ORG: Tianjin Institute of Geology, Ministry of Metallurgical Industry

TITLE: "Discovery of Al-Si spinel in nature"

SOURCE: Beijing GUOSHANAN XUEBAO (JOURNAL OF THE CHINESE SILICATE SOCIETY) in Chinese Vol. 13 No. 2, Jan 81 pp. 190-197

TEXT OF ENGLISH ABSTRACT: L. A. Brindley, et al. (1959) considered the principal crystalline phase in the exothermic reaction of clay mineral kaolinite at about 980°C as Al-Si spinel ($2\text{Al}_2\text{Si}_2\text{O}_7$ or $3\text{Al}_2\text{Si}_2\text{O}_7$) and pointed out that the Al-Si spinel is similar to that of $\gamma\text{-Al}_2\text{O}_3$, making it possible to mistake it for $\gamma\text{-Al}_2\text{O}_3$ in the case of inaccurate measurements. F. C. Loughnan, et al. (1981) found that the kaolinite flint clay could be transformed into millite and cristobalite during the self-burning of coal in New South Wales, Australia, while in the low temperature zone metakaolinite occurred. They also considered the above fact to have been discovered by themselves. However, the formation of the Al-Si spinel was not ascertained. Ma Jinping, Ba Qinglian, Jing Xigui and the author (1983) observed, near a highway in Hequ County, Shanxi Province, that carbonaceous clay had been whitened by scorching during the self-burning of coal within the carboniferous coal series. Later, through the author's study, it was determined that the temperature of the carbonaceous kaolinite had reached 1000°C, almost that needed to form Al-Si spinel near the exothermic peak of kaolinite. It is in agreement with data obtained by F. C. Brindley and with that of the exothermic peak of kaolinite. The appearance of the samples resembles kaolinite clay heated to 1000°C. They are white and soft with micropores, slightly rough, and stain fingers easily. They are also dark in luster and not viscous. The X-ray data from a powder photo (Jenex photo, 10 hours) are as follows: 1.9673 Å (strong), 1.3919 Å (very strong) and 1.140 Å (weak) in width. All of the curves of different thermal analyses and those of dehydration are straight lines. The result of chemical analysis is similar to that of the dehydrated kaolinite. The content of impurities is 0.59 percent, $\text{Al}_2\text{O}_3 = 0.9\%$. Granular texture and micropores are shown under the scanning electronic microscope. The results of infrared spectrum analysis are the same as those from the reaction when Suzhou's kaolinite was heated up to 1000-1100°C (Zhou Jingyan 1983), and the 1300-950 cm^{-1} wide peak shows the curve of the elastic vibration of $(\text{Si}-\text{O})-\text{Si}$, 806 cm^{-1} shows the vibration of $\text{Si}-\text{O}-\text{Al}$, and 464 cm^{-1} shows the vibration of $\text{Si}-\text{O}$.

The burned clay is always associated with a small amount of millite. This resembles the reaction of kaolinite heated to 1000°C, but is different from halloysite heated to 1000°C (no millite). Sometimes a small amount of halloysite (2 Å) is formed by rain action. (Paper received on 26 December 1983, revision on 31 July 1984.)

AUTHOR: GUANG Guohuang (1926-41-64 1992)
ZHANG Zhiping (1928-11-11 1971)
LI Guangping (1911-1939 1977)

ORG: Luoyang Institute of Refractories Research, Ministry of Metallurgical Industry

TITLE: "Activated Sintering (Densification) of Natural High Purity Dolomites"

SOURCE: Beijing GUISHUANYAN KUEBAI (JOURNAL OF THE CHINESE SILICATE SOCIETY) in Chinese Vol 13 No 1, Jun 85 pp 117-121

TEXT OF ENGLISH ABSTRACT: Sintering behavior of natural high purity dolomite and magnesitic dolomite was studied with calcinated specimens (D and MD) and calcinated-hydrated specimens (DH and MDH). The mechanism for the initial sintering stage of MD, DH and MDH specimens was postulated and the activation energy calculated.

Hydrate specimens are found to be much more susceptible to sintering than oxides, with a temperature difference of about 400°C for the same level of densification. The susceptibility of hydrates to sintering is expected to be related to the presence of water vapor, which gives rise to some kinds of rapid adsorption-desorption of OH⁻ between two solid phases.

Dense sinter with bulk density 3.30-3.38 g/cm³ and well-developed microstructure was obtained by sintering DH and MDH specimens at 1600°C for 2-15 hours. (Paper received on 9 June 1984.)

AUTHOR: JIANG Shaoying [3068 4801 5391]
WANG Guodong [3769 0948 2767]
ZHANG Guangrong [1728 1639 2837]
et al.

ORG: Geological Company, Geological Institute, State Administration of
Building Materials Industry

TITLE: "The Mineralogy and Industrial Application of Chrysotile Asbestos
of Shimian County, Sichuan Province"

SOURCE: Beijing GUISUANYAN XUEBAO [JOURNAL OF THE CHINESE SILICATE SOCIETY]
in Chinese Vol 13 No 2, Jun 85 pp 224-233

TEXT OF ENGLISH ABSTRACT: Most chrysotile asbestos in Shimian County, Sichuan Province, is in the form of slip-tilted fibers, but occasionally cross fibers are found. One hundred twenty-one samples of asbestos fibers, including commercial fibers, have been collected and systematic mineralogical studies on the samples have been made using wet chemical analyses, XRD, DTA, TG, IR, EM and ED. Physical properties of asbestos, such as tensile strength, elastic modulus, volume resistivity, specific magnetic susceptibility, specific gravity, heat resistance, heat conductivity, specific surface, chemical resistance, etc., have been measured, providing a lot of data, plots and tables for industrial application. Asbestos fibers in this area can be classified into four groups and seven types, according to the impurities in fibers. In addition to chrysotile crystallinity, the physicochemical condition of mineral formation and the influence of impurities on the physical properties of fibers are discussed in the paper, and the influences of mineral processing and heat treatment on the physical properties are also discussed. Many experiments show that, contrary to the rule commonly accepted, the tensile strength of chrysotile asbestos in the Shimian mine is 10-70 percent more than that of the original fibers (150-250 kg/mm²) after heat treatment at 380-450°C, so that the value of the asbestos in use is increased. (Paper received on 19 April 1984.)

AUTHOR: CHEN Jiaping [7115 1367 1627]
WANG Lamei [3769 5198 1188]

ORG: Shanghai Institute of Ceramics, Chinese Academy of Sciences

TITLE: "Determination of Ferroelastic Properties of $\text{NdP}_3\text{O}_{14}$ Crystal"

SOURCE: Beijing GUISUANYAN XUEBAO [JOURNAL OF THE CHINESE SILICATE SOCIETY]
in Chinese Vol 13 No 2, Jun 85 pp 247-249

TEXT OF ENGLISH ABSTRACT: Ferroelastic properties of the $\text{NdP}_3\text{O}_{14}$ crystal have been determined by the optical method. Experiment results of the micro-optical method show that the ferroelastic transition temperature on the (100) plane is $96 \pm 1^\circ\text{C}$. Extinction angles (ψ) between adjacent domains have been determined as a function of pressure. When a pressure of 6 kg/cm^2 is applied on the (100) plane, the phase transition temperature of the crystal is $117 \pm 1^\circ\text{C}$. Anomalous temperatures for birefringence of the $\text{NdP}_3\text{O}_{14}$ crystal are clearly shown at 142°C and 158°C , using the results of laser scanned curve. (Paper received on 12 April 1984.)

AUTHOR: YE Ruilun [0673 3843 0243]
WANG Xinrong [3769 2450 2837]

ORG: Wuhan Institute of Building Materials

TITLE: "Synthesis of a New Compound-- $\text{Ca}_8\text{Mg}(\text{SiO}_4)_8\text{Cl}_2$ "

SOURCE: Beijing GUISUANYAN XUEBAO [JOURNAL OF THE CHINESE SILICATE SOCIETY]
in Chinese Vol 13 No 2, Jun 85 pp 250-251

TEXT OF ENGLISH ABSTRACT: Recently a new compound was synthesized in the $\text{CaO-MgO-SiO}_2\text{-CaCl}_2$ system. The compound belongs to the cubic system, with regular octahedral shape, density $D_{\text{obs}} = 3.08 \text{ g/cm}^3$ and refraction index $n = 1.6910$. The crystal is stable in the range of $810\text{-}1260^\circ\text{C}$ and in incongruent at about 1265°C . From chemical analysis its molecular formula is $\text{Ca}_8\text{Mg}(\text{SiO}_4)_8\text{Cl}_2$. From powder X-ray diffraction, the unit-cell parameter is $a = 15.06 \text{ \AA}$, and the crystal lattice is a face-centered cubic lattice. By using the four-circle diffractometer, it is found that the unit-cell parameter is $a = 15.0653 \text{ \AA}$, space group is Fd_3m , and eight molecules are contained in a cell ($Z=8$). The crystal structure is determined by a direct method (SHELXTL). (Paper received on 29 January 1985.)

9717

CSO: 4009/1118

END

END OF

FICHE

DATE FILMED

14 NOV 85

